Microstructure-process relationship and reactivity at the nanoscale : a molecular dynamics study of Ni, Ni-Al, and Ti-Al metallic systems

Quentin Bizot

THESE DE DOCTORAT DE L'ETABLISSEMENT UNIVERSITE BOURGOGNE FRANCHE-COMTE

Laboratoire Interdisciplinaire Carnot de Bourgogne

Ecole doctorale n°553

Carnot - Pasteur

Doctorat de Chimie - Physique

Par

Mr Quentin BIZOT

Thèse présentée et soutenue à Dijon, le 9 Mars 2023

Microstructure-process relationship and reactivity at the nanoscale: a molecular dynamics study of Ni, Ni-Al, and Ti-Al metallic systems

Composition du Jury :

Mr Jakse Noel	PR, Université de Grenoble	Rapporteur
Mr Perez Michel	PR, Université de Lyon	Rapporteur
Mme Brochard Sandrine	PR, Université de Poitiers	Examinatrice
Mme Costil Sophie	PR, Université de Technologie de Belfort-Montbéliard	Examinatrice
Mr Nicolaï Adrien	MCF, Université de Bourgogne	Examinateur
Mme Baras Florence	CRHC CNRS, Université de Bourgogne	Directrice de thèse
Mr Politano Olivier	MCF, Université de Bourgogne	Directeur de thèse
Mr Turlo Vladyslav	Dr, Laboratoire EMPA	Invité

Remerciements

Un travail de thèse est souvent le fruit des nombreuses rencontres que l'on peut faire et des nombreuses expériences que l'on peut vivre. Ces quelques lignes seront sans doute insuffisantes pour adresser mes remerciements à toutes les personnes que j'ai pu croiser durant ces quelques années. Ces mêmes personnes sans qui ce travail n'aurait pas été mené de la même façon qu'il l'a été. Ces lignes permettront cependant de remercier les personnes qui ont pris part à ce travail que ce soit sur le plan scientifique ou personnel.

J'aimerais tout d'abord remercier mes directeurs de thèse Florence Baras et Olivier Politano qui m'ont fait découvrir la recherche à travers mon stage de master et ma thèse. Vous m'avez accordé votre confiance même si mes connaissances étaient relativement limitées sur la science des matériaux en général. J'ai appris énormément à vos côtés sur le plan scientifique et professionnel. Vous avez su m'accompagner de la meilleure des façons durant l'intégralité de ma thèse tout en me transmettant votre savoir avec passion, enthousiasme et bienveillance.

J'exprime tous mes remerciements à Michel Perez, Noel Jakse, Sandrine Brochard, Sophie Costil et Adrien Nicolaï qui ont accepté de faire partie de mon jury de thèse et plus particulièrement Michel Perez et Noel Jakse d'avoir accepté de rapporter ce travail de thèse. Un grand merci pour tous vos conseils, vos suggestions et l'intérêt que vous avez porté à mes travaux. Une mention particulière revient également à Adrien Nicolaï sans qui mon attrait pour le numérique aurait sûrement été différent.

Merci également aux collaborations qui ont contribué à rendre ce travail plus riche. Je tiens à remercier A. S. Rogachev, A.A. Nepapushev et S. G. Vadchenko pour la collaboration franco-russe avec une mention spéciale pour les discussions très intéressantes que nous avons eu avec A. S. Rogachev lors de son séjour en France. Je tiens également à remercier Vladyslav Turlo pour la collaboration franco-suisse. La visite de son laboratoire, avec les nombreuses discussions scientifiques qui en ont découlées durant ce court séjour, a grandement été apprécié.

Je remercie chaleureusement Mary Bouley pour toutes les corrections, suggestions et explications détaillées en anglais sur l'ensemble de ce manuscrit.

Merci à Didier Rebeix et toute son équipe qui sont toujours présents pour répondre aux

questions relatives au Centre de Calcul de l'Université de Bourgogne. Je remercie plus particulièrement Didier Rebeix qui m'a donné l'opportunité de visiter les infrastructures du centre de calcul.

Merci à tous les doctorants et postdoctorants Adrien S., Mélanie F., Corentin, Damien, Célia, Adrien F., Bastien, Alan, Eduardo, Simon, Margaux, Laura, Jérémie, Rémi, Anthony qui ont rendu le quotidien plus joyeux durant ces années de thèse en partageant de nombreuses activités. Je vous souhaite plein de réussites professionelles et personnelles.

Je tiens à remercier l'ensemble du 4ème étage pour toutes les discussions durant les pauses café : Lionel, Lucien, Michaele, Sophie, Julien, Frédéric D., Frédéric B., Nadine. Vous avez été très importants durant ces années en participant à la bonne ambiance de l'étage.

Un merci également aux équipes MaNaPi et M4Oxe pour les discussions scientifiques et amicales que j'ai pu avoir tout au long de ces années de thèse.

Je souhaiterais également remercier toutes les personnes qui ont contribué à leur façon à cette thèse : Thomas, Manuel, Olivier, Guy, Claude.

Merci à tous les amis du vendredi-foot qui permettent de s'amuser, de rigoler, de décompresser et de partager des matchs les vendredis midi.

J'adresse mes remerciements à ma famille et mes amis qui m'ont toujours soutenu durant cette thèse. Leurs soutiens indéfectibles m'ont permis de passer ces années en toute sérénité.

Finalement, je tiens à remercier ma (petite) Mélanie R. qui a su m'encourager, me soutenir et me supporter au quotidien surtout pendant les moments les plus difficiles. Reçois tout mon amour.

Contents

Chapter 1

Context of the study

Because of climate change and sustainable development, it is necessary to adopt new processes for the manufacture of metallic parts, lowering material losses and reducing the cost of the final product. Unlike traditional techniques based on substractive processes, powder metallurgy offers new perspectives. Powder metallurgy consists of three basic steps: powder blending, die compaction, and sintering, and encompasses a large number of techniques such as Spark Plasma Sintering (SPS) or Hot Isostatic Pressing (HIP). Additive manufacturing (AM) is a relatively novel family of techniques which use metal powders (among other materials, such as plastics) to make parts by laser sintering or melting. Since the advent of industrial production–scale metal powder–based additive manufacturing (AM) in the 2010s, metal AM processes are a new category of commercially important powder metallurgy applications. A key step in Powder Metallurgy is powder preparation. Ball milling is commonly used to grind or blend metallic powders. High-energy ball milling changes the reactivity of as-milled solids (mechanical activation), induces phase transformations and defects in starting powders, or provokes chemical reactions (mechanochemistry).

In material sciences, the understanding of the relationship process-microstructure-performance is of primary importance. In this respect, microstructure modeling is useful for predicting the impact of processing conditions on performance of the resulting material. As the microstructure is associated with many processes running on different scales, a multi-scales approach is necessary. As an example, multiscale modeling of additive manufacturing of metal-based materials includes: macroscale modeling to extract temperature profiles, mesoscale modeling for evaluating melt flow, microscale modeling for investigating microstructure development, and nanoscale modeling to describe solid/liquid interfaces. As shown in Fig. 1.1, different simulation techniques were developed to address a specific problem at relevant time and length scales.

In the present manuscript, we focused on the atomic level by means of classical molecular dynamics simulations. That approach can be considered as an *in-situ* tool that allows us to follow the elemental mechanisms governing kinetics aspects, at the mi-

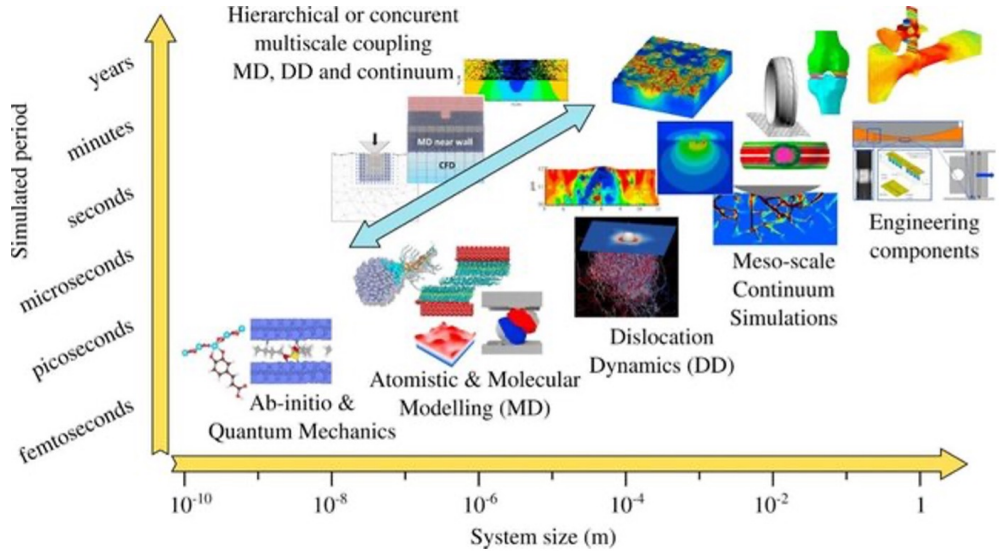

Figure 1.1: Schematic representation of the different numerical methods with respect to their length and time scales. From [1].

croscopic level. It consists in solving numerically the equations of motion of a set of atoms for which the interaction law is specified. The main limitations are the reliability of the interaction potential, the number of atoms (a few millions) and the time scale (nanosecond). This method will be presented in details in Chapter 2 together with numerous case studies in Materials Science. In this chapter, we give an overview of the processes on which we focused. Additive manufacturing is first introduced in 1.1 together with the state of the art of modeling. The mechanical treatment of powders is presented in 1.2.

1.1 Additive manufacturing

Additive manufacturing (AM) is a promising technology that enables complex-shaped parts with tailored properties to be produced using layer-by-layer deposition. This technology uses a local high-power heat source to melt material in the form of powder or wire. The melted material solidifies as the heat source moves away from the molten region [2–5]. The main advantage of metal AM compared to conventional manufacturing is that it is possible to design complex shapes in one step, while reducing waste, and eliminating assembly time and cost. The impact on the environment is limited by reducing energy consumption and carbon footprint.

The first AM technology was developed in the 80s to manufacture three dimensional objects layer-by-layer with photopolymers using UV light beam. Since many technologies have been developed and several materials can be used such as polymers, metals, ceramics, biochemicals, or glass.

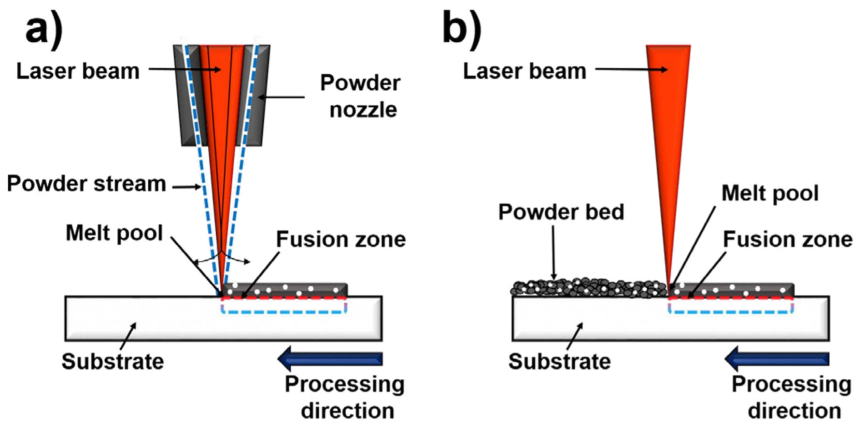

Figure 1.2: Schematic representation of the main additive manufacturing techniques (a) power bed fusion (PBF) and (b) direct energy deposition (DED) categories. From [6].

Frazier *et al.* [7] published in 2014 a review article that classified the metal AM technologies regarding the material feed stock, the energy source, and the build volume. Among all the available approaches, the two main categories are power bed fusion (PBF) and direct energy deposition (DED) (see Fig. 1.2). In PBF, a thermal energy source such as a laser or an electron beam is used to melt or fuse materials previously deposited on a bed in powder form. Once a powder layer has been processed by the laser, it is lowered and a new layer of fresh powder feed again the bed. This process is repeated until the complete metallic part is designed. In DED, the powder or wire is streamed through a nozzle and a heat source is focused on this stream to melt the metal. The melted material is then deposited layer by layer with the desired shape on a substrate. Different sub-categories exist depending on their specificity such as the type of heat source (laser, arc or electron beam) and material feed-stock (wire or powder).

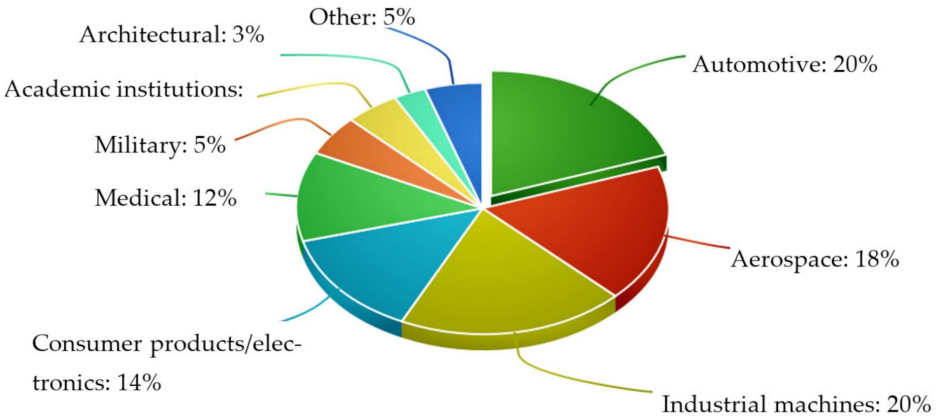

Figure 1.3: Distribution of industrial fields related to metals AM technologies. From [8].

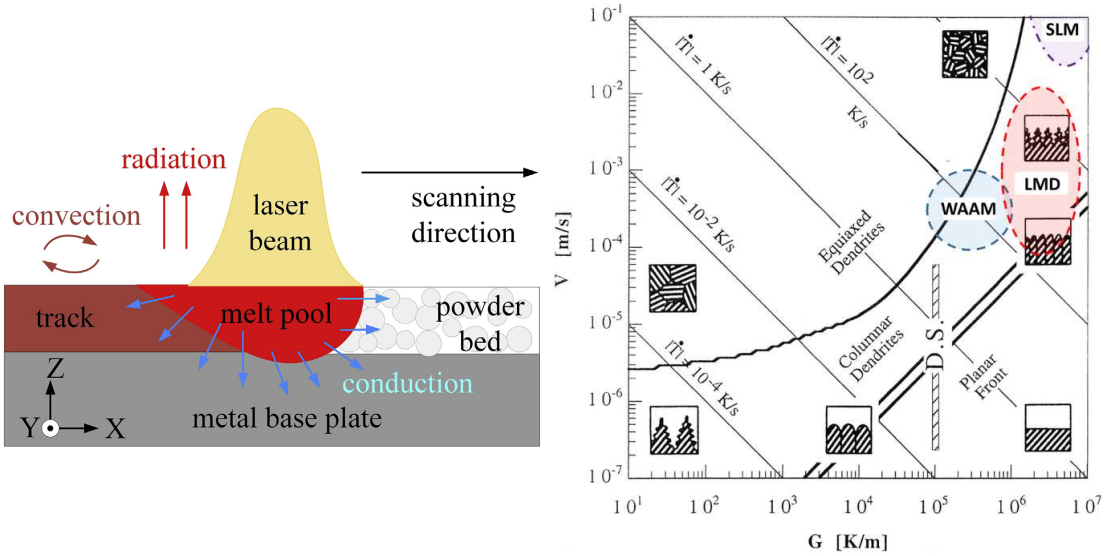

Figure 1.4: On the left, schematic representation of the meltpool with thermal processes induced by an energy source (here a laser). From [22]. On the right, microstructure associated to gradient and velocity in AM technologies: Selective Laser Melting (SLM), Wire Arc Additive Manufacturing (WAAM), Laser Metal Deposition (LMD). From [23]. SLM is a Power Bed Fusion technology while WAAM and LMD are Direct Energy Deposition techniques. WAAM uses electric arc as heat source and wire as feed-stock. LMD technology uses a laser as heat source and the feed-stock is either powder either wire.

The number of metallic materials used in metallic AM is constantly increasing. The most used are titanium alloys [9], aluminum alloys [10], nickel-based alloys [11], HEA [12], steels [13], precious metal alloys [14], copper alloys [15], cobalt-based alloys [16], bimetals [17] and gradient alloys [18]. As shown on Fig.1.3, innovative metal AM has already found numerous applications in the automotive, aerospace, electronics, and biomedical industries [8, 19–21].

A typical AM process involves the local melting of the metal and the solidification of the melt pool (Fig. 1.4). Because the heat source is usually not uniform (a Gaussian in the case of a laser), a temperature gradient develops at the melt pool surface with a significant variation of surface tension. This effect leads to thermocapillary convection in the melt pool. Once the energy source is stopped or focus on another location, heat transfer by conduction on the solid side begins and induces progressive solidification of the meltpool. In addition, there exist radiative heat losses at the surface of the melt pool. Solidification in AM technologies is directional due to high temperature gradients and rapid due to high cooling rates. Moreover, the layers treated successively give rise to repeated melting of the materials resulting in a very complex thermal history. Thus, solidification carries out in non-stationary and non-equilibrium conditions. Yet, the way solidification develops is crucial because it determines the microstructure and performance of the final product.

In general, two specific microstructures are observed during AM processes, namely a structure composed of columnar grains and/or equiaxed grains. Columnar grains (dendritic or cellular) are often associated with rapid solidification and steep thermal gradient (Fig.1.4). Equiaxed grains result from nucleation processes (inoculant particles or impurities) or from dendrite fragments. Indeed, dendrite fragments can detach during solidification under the effect of the constraints. Later, these fragments are transported by convections within the meltpool. For both mechanisms, equiaxed grains are formed blocking columnar growth. Structures with columnar grains present anisotropic mechanical properties. Structures with fine equiaxed grains exhibit more homogeneous properties [24]. For this reason, structures with equiaxed grains are particularly interesting and several studies aim at the production of these structures.

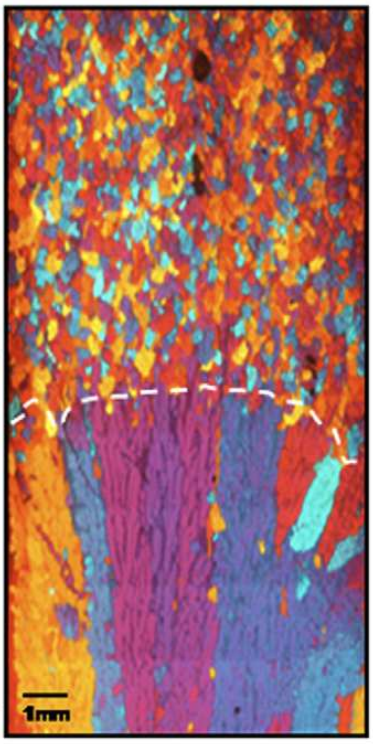

Figure 1.5: Example of columnar (bottom part of the sample) and equiaxed structure (upper part of the sample) with the transition between both structures delimited by white dashed line. This represent the longitudinal section of solidified Ni-Al alloy obtained in a furnace. From [25].

Therefore, the columnar-to-equiaxed transition (CET) is central to the control of the solidified microstructure (see Fig. 1.5). In alloy solidification, the main parameters governing CET are the temperature gradient, the velocity of the solidification front, the cooling rate, and constitutional undercooling. The critical gradient condition for fully steady-state equiaxed growth with a given density of inoculants has been estimated by Hunt and is commonly used as a rough estimate of CET [26]. Kurz *et al.* [27] and Gaumann *et al.* [28] improved Hunt's model with a dendritic growth model more

appropriate for the rapid solidification observed in AM processes. In order to deal with the specific characteristics of AM, extensive experimental work (see, for example [29]) and theoretical studies have been carried out to predict favorable CET conditions.

Modeling of Additive Manufacturing

Modeling AM processes requires a multiscale approach: the macroscopic scale to record thermal history, the mesoscopic scale to predict melt pool dynamics, and the microscale to describe microstructure formation. Process modeling based on finite element methods or computational fluid dynamics often integrates experimental measurements to predict process defects such as cracks and pores as well as to estimate surface roughness of the final parts [30]. At the microscale, stochastic models such as cellular automata and kinetic Monte Carlo can provide micrographs of grain structures close to those observed experimentally. Such models nevertheless leave aside many physical phenomena, relying on effective parameters that are not transferable, but have to be fitted for each new material of interest [31]. In contrast, phase field modeling provides a much more comprehensive description of solidification at the microscale that involves the formation of dendrites, microsegregation, and precipitation [32]. Phase-field can also be combined with cellular automaton to study competitive growth of columnar dendritic grains under temperature gradient [33]. The multiscale phase field method can also be used to describe heterogeneous nucleation, grain selection, and epitaxial growth to assess the role of AM parameters in CET [24]. However, at nanoscale, few models report CET, except for a recent work by Kurian *et al.* [34], which studied the micro-selective laser melting process using molecular dynamics (MD) simulations in order to investigate melting and solidification of a randomly-distributed aluminum nano-powder bed.

Modeling of solidification at the microscopic level

Many solidification processes have nevertheless been investigated at the nanoscale by means of MD simulations. The pioneering work of Lu and Spzunar [35] described the structural changes induced by rapid solidification. Fast quenching leads to a nonequilibrium glassy state, while a slow cooling rate results in a crystalline state [36–38]. The characteristics of a solidification front have been measured by MD in two-phase metallic systems under isothermal conditions for different orientations of the solid-liquid interface in order to obtain the kinetic coefficients [39, 40]. The case of directional solidification has been studied using non-equilibrium MD simulations for Lennard-Jones systems [41], Al-Cu alloys [42], and CrNi-alloyed steels [43]. Large-scale MD simulations with several million atoms have been used to study the very first steps of solidification in various metallic systems. Homogeneous nucleation has been studied at constant undercooling temperature or by applying a constant cooling rate on a melted metal [44, 45]. Athermal heterogeneous nucleation through grain refiners in

undercooled metal has also been investigated by MD simulations [46].

The columnar-to-equiaxed transition was not systematically investigated by MD in the case of pure metal, in the typical non-stationary thermal conditions specific to AM. In pure metals, the microstructure results exclusively from thermal effects occurring during solidification processes. The simulations will allow us to understand the different thermal mechanisms leading to different solidified microstructures. The results obtained on the topic in the framework of my PhD and their direct comparison to classical theories of solidification/nucleation will be presented in Chapter 3.

1.2 Mechanical treatment of powders

Mechanical treatment of powders in planetary ball mills is a very common process used for several purposes including the synthesis of inorganic compounds and metallic nanocomposites, the formation of supersaturated solid solutions or metastable crystalline phases, and the elaboration of nanostructured materials or amorphous alloys [47]. Mechanosynthesis, also termed mechanochemistry or mechanical alloying, supposes that the reaction is completed during the mechanical treatment [48]. In contrast, preliminary mechanical activation is used to fabricate reactive materials [49], and the reaction follows the activation process. As an example, the combination of mechanical activation and reactive sintering leads to the formation of nanostructured intermetallics [50], and nanostructured High Entropy Alloys [51]. Nanocomposites prepared by mechanical milling are also used in additive manufacturing [52, 53], where attention is paid to particle size and shape.

Popov *et al.* described the fundamental requirements of powders used in AM. The shape of the powders needs to be as spherical as possible with a smooth surface. Powder size must be controlled to range from few micrometers to 240 micrometers depending on the AM technology. The powder size distribution is also important because finer powders in the distribution enable to fill the void between the larger powders resulting in a higher packing density [54]. In addition, the powder flowability is often described as the crucial parameter to produce high quality powder layer [55]. Because of its ability to produce regular spherical powders, atomization is currently the most widely used technique [56]. However, this technology finds limitation to produce composite reactive particles due to the difference of mechanical properties of the different reagents. One way to solve this limitation is the high energy ball milling (HEBM) such as planetary ball mills.

Planetary ball milling

In the planetary ball mills, the jars containing the powder and the grinding balls are arranged on a sun wheel. The sun wheel rotates in one direction while the jars rotate in the reverse direction (Fig.1.6). In practice, powders processed in planetary ball mills are submitted to a series of transformations induced by contact with grinding balls. The

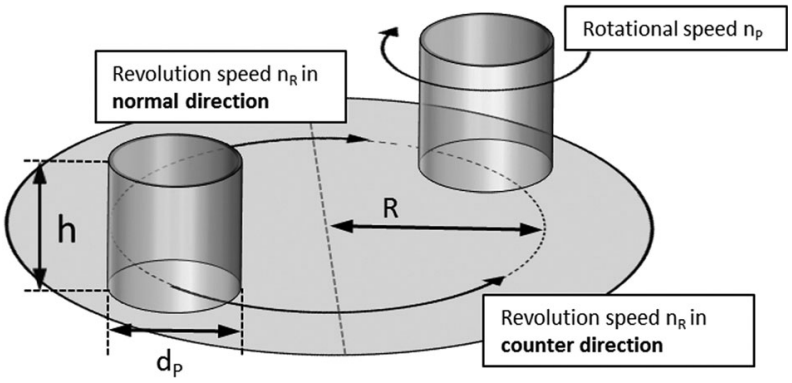

Figure 1.6: Schematic representation of a planetary ball mill. From [57].

different elemental load modes observed in milling experiments include compression, shear, shock, cutting, and impact. Beinert *et al.* [58] classified the contacts between beads or bead and wall into four contact types: impact, torsion, shearing, and rolling, as a function of the relative velocity of colliding bodies (Fig. 1.7, right). In addition, *in situ* observations have demonstrated that milling balls undergo complex motions in the jar [59]. Three milling regimes were identified as a function of milling parameters in the case of a large number of grinding balls [57]. In cascading regime, the balls are taken along the container and unroll upon each other from the bulk top to its base. Friction between grinding balls is dominant. In cataracting regime, the balls detach from the wall and impact the other balls or the opposite wall with high intensity. In centrifugal regime, the balls are stuck to the inner wall of the vial and move together with the vial (Fig. 1.7, left). The specific milling regime was found to influence the microstructure and reactivity of the final powder mixture [60]. The action of balls on the blended elemental powders is essential to control the effects of milling. The two main activation factors are the collision of grinding balls with one another and with the milling wall, and friction between the grinding balls.

The fundamental question is to determine how the mechanical energy delivered by the mechanical process is stored in the powder, leading to enhanced reactivity in activated powders. The most common explanation is to assert that mechanical energy is stored in defects created during severe plastic deformation associated with mechanical treatment. According to Hoffman *et al.* [61], the defects due to mechanical treatment include: zero-dimensional point defects, such as vacancies; one-dimensional line defects, such as dislocations; two-dimensional area defects, such as stacking faults, grain boundaries, and contact areas with other phases. Three-dimensional volume defects include amorphous regions, pores, other phases, and metastable regions, corresponding to the development of structural transformations. The energy associated with different types of point defects, dislocations, and grain boundaries has been evaluated by Khina [62, 63]. Low-dimensional defects appear to have a negligible effect on subsequent reactivity, in comparison with metastable phases, for which the formation mechanism is not yet understood.

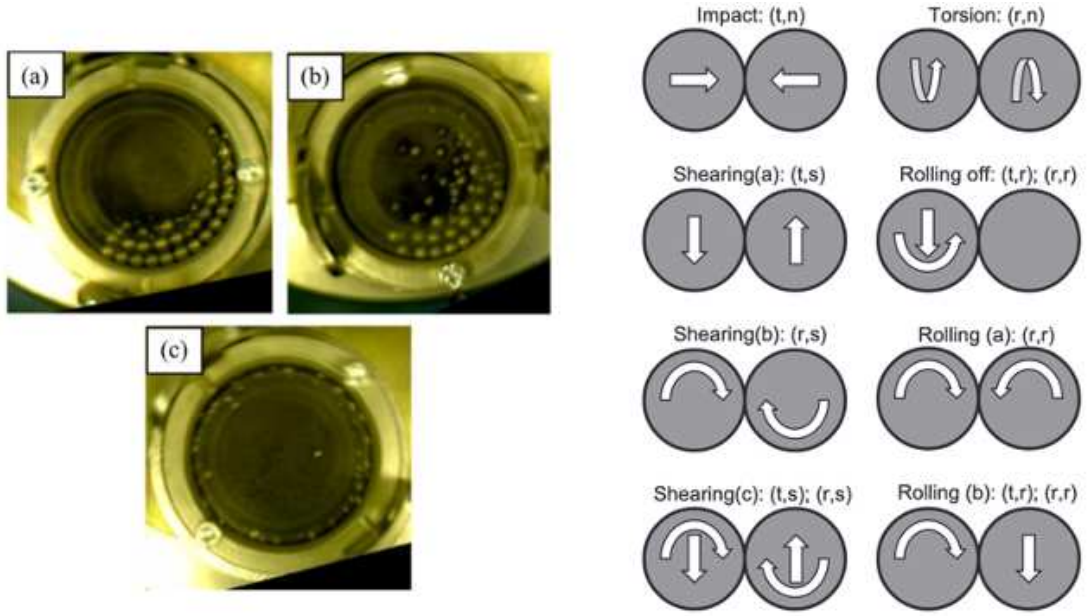

Figure 1.7: On the left: *in-situ* observations of the specific regimes recorded via high speed video camera: (a) the cascading regime, (b) the cataracting regime and (c) the centrifugal regime. From [60]. On the right: specific motions of the grinding balls observed in the container. Four distinct loading modes are represented namely the impact, the torsion, the shearing and the rolling. From [58].

Characterizing the reactive properties of activated powders is important to design reactive material with tailored reactivity, and to choose the most adequate parameters for the elaboration process (e.g., milling speed).

Reactivity of activated powders

In order to understand the effect of mechanical activation on reactivity, the Ni-Al or Ti-Al systems have been widely studied experimentally. It has been shown that high-energy ball milling affects the reaction kinetics of these reactive composites [64, 65]. In the case of Ni-Al, it was demonstrated that the effective activation energy of the reaction is significantly reduced after mechanical treatment [66]. In the case of Ti-Al, Nepapushev *et al.* presented the difference of temperature of ignition regarding the milling time and the size of the grinding balls as shown in Fig. 1.8 . They reported that temperature of ignition can be lowered to 640 °C compared to 850 °C without mechanical activation [52]. This reduction may be attributed to structural refining that leads to an increase in the number of contact surfaces (Fig. 1.9). In addition, microstructural analysis has shown that nanosized clusters are formed, which can serve as highly reactive precursors of new phases, and thus reduce the potential barrier to the initiation of exothermic reaction.

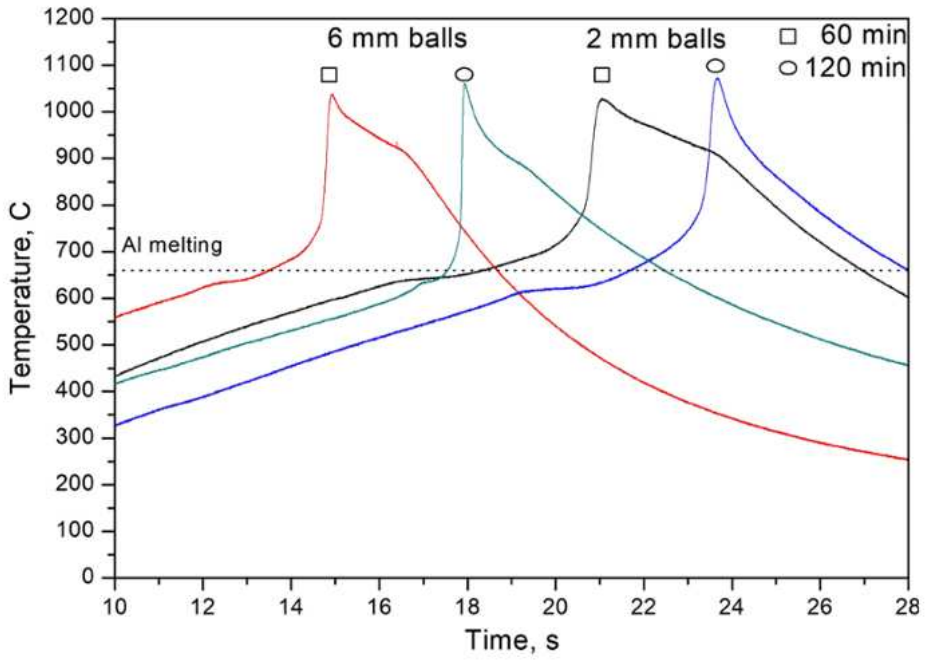

Figure 1.8: Thermograms of the Ti/Al mixtures after mechanical treatment. The size of the milling balls are 6 mm (red and green curve) and 2 mm (black and blue curve). The milling times are 60 min and 120 min represented by square and circle, respectively. The black dashed line represents the melting temperature of Al close to the beginning of the reaction. From [52].

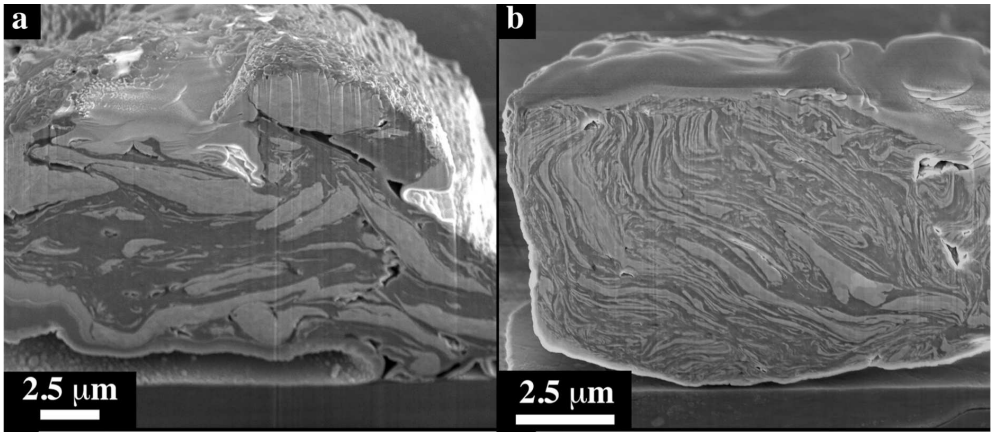

Figure 1.9: SEM images showing nanostructured Ni-Al system obtained after (a) 10 min and (b) 40 min of milling. The corresponding structure exhibits a very large number of surface contacts between Ni and Al (especially after 40 min), which lowers the ignition temperature. From [66].

A problem of topical interest is to understand how impact and friction (the two prevalent actions during milling) act on the powder and modify microstructure evolution. Several studies have already been conducted at the atomic level. The plastic deformation induced by milling was modeled by cyclic deformation [67, 68]. These studies have demonstrated that cyclic deformation forces chemical mixing due to dislocation gliding. The progressive amorphization and mixing of a binary system through extensive plastic straining has been studied in [69], by means of a strain-and-stack process similar to cold-rolling. Since the pioneering work of Holian and coworkers [70], the friction between sliding metallic blocks has been extensively studied (see for instance [71]). The frictional sliding of solid surfaces involves large plastic strains and strain gradients, high strain rates and strain rate gradients, and mechanical mixing from both contacting solids. Mechanical mixing was attributed to different mechanisms: interface instability that leads to local vorticity, dislocation and twin activity, and amorphization. Atomic mixing in metals under shear deformation has been studied at various interfaces in [72]. The mixing was found to be diffusive or "superdiffusive", depending on the coherence between interfaces. Heat dissipation due to sliding was investigated by means of non-equilibrium Molecular Dynamics simulations [73, 74]. Atomic-scale mechanical mixing and generation of mixing layer were observed in the regions near the contact interface. The enhanced reactivity of mechanical activated systems has also been considered in the literature. The mechanisms of loading and chemical processes resulting from shock compaction have been investigated in the case of Ni/Al composites by means of Molecular Dynamics simulations [75, 76]. The role of porosities in such systems during deformation has been considered in [77]. The reactivity of Ni-Al composites prepared by mechanical activation has been studied in order to detect the role played by the nanoscale mixing of the reagents [78]. But, in these studies, a nano-laminated structure or premixing of reagents was assumed. So a complete description of the effects induced by the mechanical treatment of elemental powders from activation to reaction is still lacking.

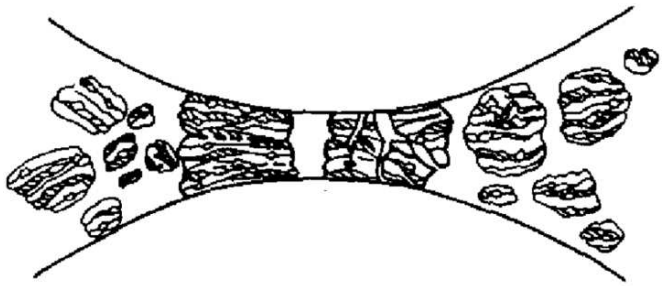

Figure 1.10: Schematic representation of the impact of grinding balls acting on the powders. From [79].

In order to obtain a better understanding of the mechanisms that take place during mechanical activation at the atomic level, Molecular Dynamics simulations mimicking the

effects of grinding balls on powder particles can be developed. We modeled the impact of grinding balls and their action on blended powders following Maurice and Courtney's idea [79] (see Fig. 1.10). Flat surface tools act on a large number of individual powder particles and cause uniaxial compression of the powder. Despite unavoidable limitations in system size and simulation time, large-scale Molecular Dynamics simulations are a useful tool to provide *in situ* observations during mechanical activation. We considered a set of metallic binary systems: Ni-Al, Ti-Al, Fe-Cr, and Fe-Ni [80]. It is expected that a layered structure would be observed in ductile/ductile binaries. In the case of couples with dissimilar ductility, the resulting composite represents a metallic matrix with inclusions of the less ductile phase. The aim is to understand the specific behavior of each couple as a function of the mechanical and structural properties of its elemental constituents. Understanding the specific behavior of metallic couples during mechanical activation is important when this process is used to fabricate complex alloys. The efficiency of mechanically induced deformation will be investigated by measuring amorphization rate, chemical mixing efficiency, and the creation of defects. In order to evaluate their reactivity, activated Ni-Al and Ti-Al systems were studied at different temperatures, below and above the melting point of the less refractory element (Al). Both diffusion and reaction mechanisms will be evaluated in Ni-Al and Ti-Al systems. The results will be presented in Chapter 4.

Reactivity of multilayer nanofoils

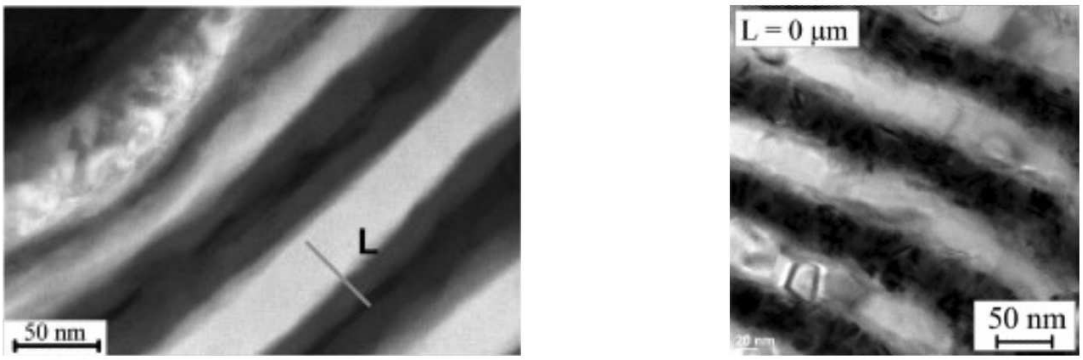

Figure 1.11: On left, STEM image of the microstructure of Ni-Al mixtures obtained after planetary ball milling process. From [64]. On right, TEM image of Ni-Al reactive multilayer nano-foils produced by magnetron sputtering. From [81].

Reactive laminated particles (RLPs) produced by planetary ball mill present very close similarities with Reactive multilayer nanofoils (RMNFs) (see for instance Fig. 1.11 for Ni-Al mixtures). They are often used as model systems to study the processes occurring at the atomic scale in metallic nano-systems presenting a huge amount of interfaces. The RMNFs are composed of hundreds of stacked thin metallic layers, varying in thickness from 4 to 100 nm. They can be prepared by several methods such as sput-

tering, vapor deposition or electrodeposition [82, 83]. The pure metals are arranged alternately with layer of one metal and layer of another metal (Fig.1.11). The reaction occurs after an ignition process such as mechanical loading, thermal heating, laser heating or electrostatic discharge [82]. The exothermic reaction propagates along the foil without any further energy supply, leading to the transformation of reactants into intermetallics. Trevizo *et al.* listed the different reactive nanometric multilayers materials [84], including Ti-Al systems. In such bimetallic Ti/Al nanofoils, a short-term local heating will induce a rapid and self-sustaining reaction [85]. The propagation velocity of the reaction is up to 3 m/s [86, 87]. The overall reaction temperature is higher than the melting temperature of Al (T_m = 933 K) and lower than the melting temperature of Ti (T_m = 1923 K). Thus, the reaction proceeds in a liquid/solid system. A Ti-Al foil is transformed in intermetallics in less than 50 ms. The kinetics of intermetallic phase formation in the Ti/Al multilayers has been investigated using differential scanning calorimetry and time-resolved X-ray diffraction [88, 89].

Chapter 5 is dedicated to the reactivity of Al-Ti system and the formation of intermetallic compounds upon a certain temperature of ignition. This part allows us to obtain a full microscopic understanding of the reactivity in the case of a perfect layered structure of Ti-Al. Different observations at the microscopic level were also conducted in order to understand how the dissolution process occurs. That study, at the microscopic scale, also makes possible to explain the various observations of our Russian colleagues who did the experimental part.

Chapter 2

Molecular Dynamics simulations

2.1 Molecular Dynamics Method

Molecular Dynamics (MD) allows one to simulate the time evolution of a system made of atoms. It has been proven to be a valuable tool to predict thermodynamics or kinetic properties and to observe in-situ atomic processes in order to understand physico-chemical mechanisms. Classical MD approach is based on the Born-Oppenheimer approximation: the motions of the electrons adapt themselves instantaneously to the displacements of the cores. Hence, electron motion is not taken into account and MD treats atomic nuclei as classical particles whose trajectories are determined by integrating Newton's equations:

$$f_i(t) = m_i \frac{d^2 r_i(t)}{dt^2} \tag{2.1}$$

where m_i is the mass, f_i is the force and $d^2 r_i / dt^2$ the acceleration of the atom i. Newton's equations are integrated, with a time step dt, in a discrete time domain. dt must be low enough to avoid instability and conserve energy, but not too low in order to avoid waste of computing time (typically dt=1-2 fs). The forces f_i applied to the atoms are conservative, meaning that the work between two points does not depend on the path followed by the force between these two points. The forces are given by the derivative of the potential energy U depending only on the relative positions of the atoms:

$$f_i(t) = -\nabla_{r_i} U(r_1, \ldots, r_n) \tag{2.2}$$

The MD algorithm is divided into three main parts: initialization, simulation and post-processing, as summarized in Fig. 2.1:

1. The positions of the atoms and their velocities are initialized. Atomic positions will depend on the system and its specific structure. Initial velocities are assigned randomly according to a Maxwell-Boltzmann distribution at a given temperature. The potential energy U is computed with an interatomic potential. The force f_i acting on each atom is then determined according to Eq. (2.2).

2. Positions and velocities are updated by integrating the equation of motions (velocity Verlet algorithm).
3. After the displacement of the atoms, system properties are computed, analyzed and visualized with appropriate software.

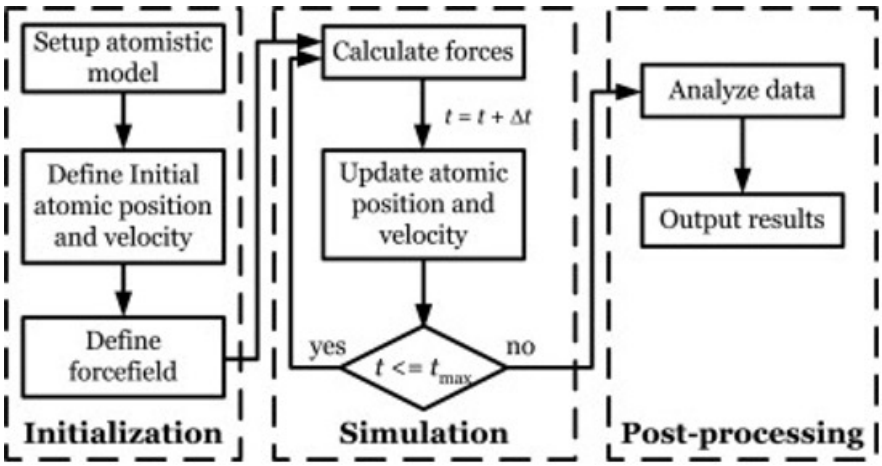

Figure 2.1: Schema of the basic molecular dynamics simulation [90].

2.2 Initialization

2.2.1 Crystal lattice

Before starting a simulation, atomic positions must be set, usually according to a particular crystalline structure that is composed of a periodic ordered stacking of atoms in space. The periodicity is defined by a basis - defined by 3 vectors Aℓ with $\ell = 1,2,3$ - that is replicated over space. Basis vectors are not necessarily normed or orthogonal and form a parallelepiped called a unit cell. Unit cells are divided into 7 crystal classes: cubic, tetragonal, monoclinic, orthorhombic, rhombohedral, hexagonal or triclinic, depending on the angles and lattice parameters (see Fig. 2.2). Moreover, there exist 4 types of unit cells known as Primitive, Body-centered, Face-centered and Side-centered. Thus, one can distinguish 14 Bravais Lattices. Finally, to build a crystalline lattice, the unit cell is replicated by a vector:

$$R_{i,j,k,\ell} = iA_1 + jA_2 + kA_3 + a_\ell \tag{2.3}$$

where a_l are the coordinates of the atoms in the unit cell.

To perform MD simulations of non-crystalline systems (e.g., amorphous or liquid phase systems), the initial box can be filled with a random distribution of atoms corresponding to a given density. Another approach will consider the melting of a solid system at high temperature to create a liquid phase which will be cooled down to reach the temperature of interest.

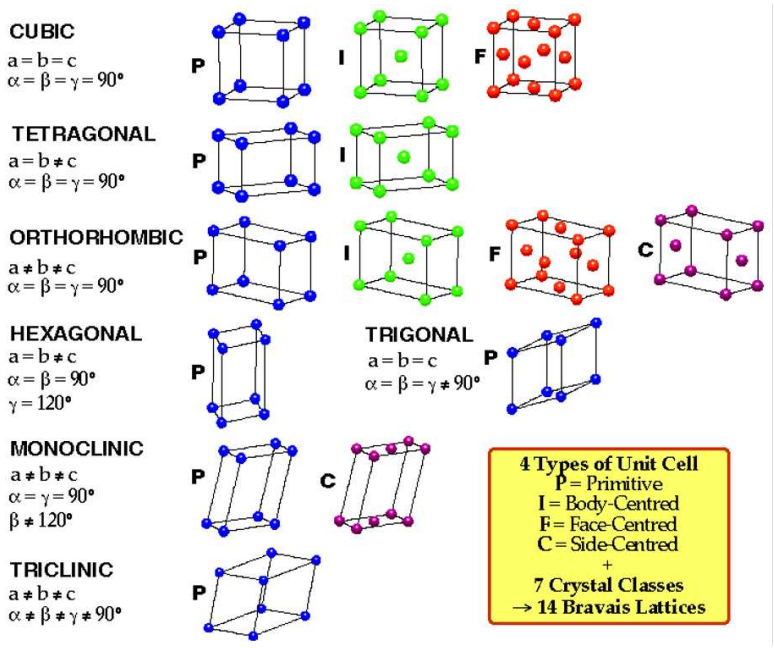

Figure 2.2: List of the different Bravais unit cells. From [91].

2.2.2 Velocity and temperature initialization

The initial velocities of the atoms follow the Maxwell-Boltzmann distribution:

$$P(v_{i,\alpha}) = \left(\frac{m}{2\pi k_b T}\right)^{-\frac{1}{2}} e^{-\frac{mv_{i,\alpha}^2}{2k_b T}} \tag{2.4}$$

with $v_{i,\alpha}$ the velocity of the atom i and α one of the three components of the direction x, y and z. The distribution of velocity is also directly related to the instantaneous temperature $T(t)$ of the system through the equipartition theorem:

$$< \frac{mv_\alpha^2}{2} >= \frac{1}{2} k_b T \tag{2.5}$$

which relates the kinetic energy of atoms to the temperature of the system. In order to avoid significant fluctuation in temperature, a large number of atoms is required. It can be estimated that the fluctuations on $T(t)$ follow:

$$\frac{\Delta T(t)}{< T(t) >} = \frac{\left(< T^2(t) > - < T(t) >^2\right)^{\frac{1}{2}}}{< T(t) >} \sim N^{-\frac{1}{2}}. \tag{2.6}$$

In the present work, the smallest number of atoms used in a simulation is 40000, corresponding to a relative temperature fluctuation of 0.5 %.

2.2.3 Interatomic potentials

Interatomic potential is the cornerstone of MD simulations as it captures all the physical characteristics of the system such as lattice parameters, cohesive energy, elastic constants, defects, stacking faults and surface energies, diffusion barriers, etc. These quantities, obtained by experimental measurements or by *ab-initio* calculations, are collected in the fitting database. In classical approaches, the potential energy is expressed in terms of empirical interatomic potentials with many body notations:

$$U(r^1, r^2, ..., r^N) = \sum_i U_1(r^i) + \sum_i \sum_{j>i} U_2(r^i, r^j) + \sum_i \sum_{j>i} \sum_{k>j} U_3(r^i, r^j, r^k) + ... \quad (2.7)$$

where U_1 refers to a one-body term equivalent to an external force. U_2 represents a two-body term in which the interaction between any pair of atoms ignores the influence of other atoms. This pair term, including Morse, Born-Meyer or Lennard-Jones terms, has been widely used for rare gases but is inefficient to reproduce metallic, covalent or ionic interactions. It was only in the 1980s that a three-body term U_3 was introduced. This term takes into account the presence of a third atom which influences the pairwise interaction of the atoms. The kind of potential used depends on the type of interaction. For example, the Stillinger-Weber, Tersoff or Brenner potentials are more suited to covalent interactions. Finnis-Sinclair (FS), the Embedded Atom Method (EAM) or modified-EAM (MEAM) are used when considering metallic interactions. The differences among these potentials arise from the way the parameters are calculated or from their analytical forms. In this manuscript, the potentials used are EAM and FS. Although their analytical forms are similar, the Finnis-Sinclair potential is based on the second-moment tight binding approach, whereas the EAM potential is based on density-functional theory (DFT). The potential energy of the EAM or FS type is expressed as follows:

$$U = \frac{1}{2} \sum_{i,j(i \neq j)} \phi(r_{ij}) + \sum_i F_i(\rho_i)\,. \quad (2.8)$$

The potential is composed of two terms: the first one, $\phi(r_{ij})$, represents the pair interaction between 2 atoms. It makes it possible to reproduce the repulsion between atoms. The second one, F, corresponds to the embedding energy of the atom i in the host electron density ρ_i produced by neighboring atoms at the atom i site (see Fig. 2.3). This term corresponds to the cohesion of the system and yields the metallic interactions between atoms. The functional F differs between FS and EAM type potentials. Indeed, in the FS approach, the binding energy is proportional to the square root of the electron density, whereas in the EAM approach, F corresponds to the energy required to place an atom i in the local electron density area produced by the neighbor atoms. This electronic density for a given atom i is given by the relation:

$$\rho_i = \sum_{j=1(j\neq i)}^{N} \varphi_j(r_{ij}) \tag{2.9}$$

where $\varphi_j(r_{ij})$ is the electronic contribution of the neighbor atoms j of the atom i.

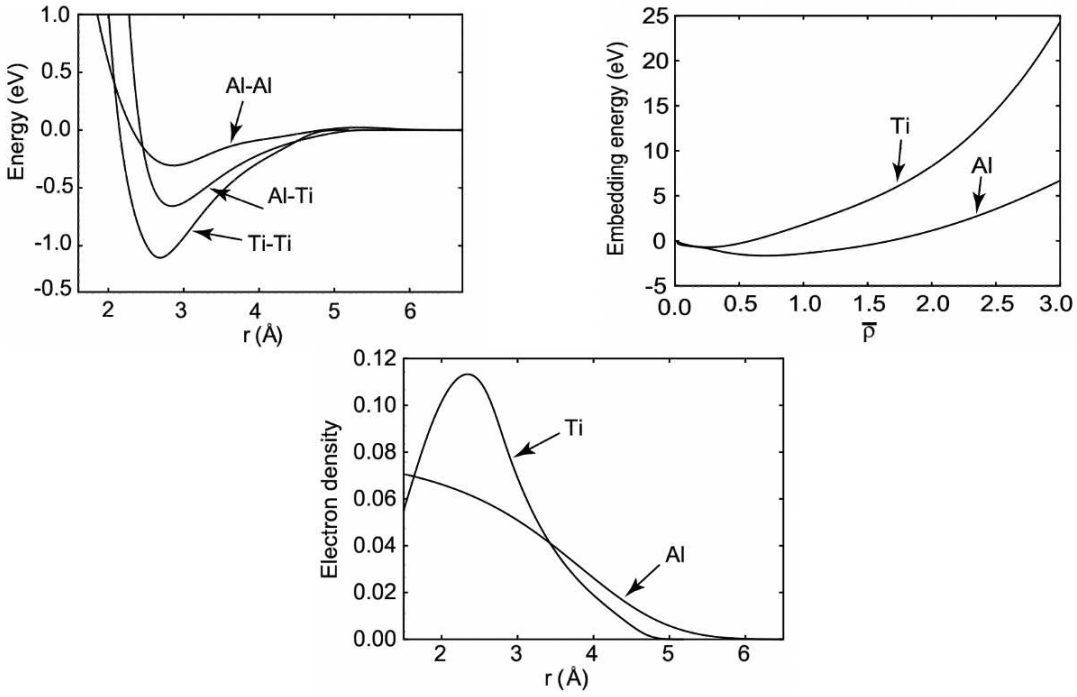

Figure 2.3: Potential functions of the EAM Ti-Al potential. From [92]. Top left, the pair interaction function, $\phi(r_{ij})$, for three different interactions between Al-Al, Ti-Ti and Ti-Al. Top right, the embedding energy function, F_i, of Ti and Al. Below, the electronic density function, ρ_i, for Ti and Al.

The potentials are designed to reproduce certain material properties at the expense of others. For example, a potential may be created specifically to capture the transport properties of a material, but it will not be transferable to simulations that wish to calculate the mechanical properties. One major difficulty is to obtain an appropriate potential that is suited to the system of interest. Sometimes, there is no potential or it is not parameterized for the purpose of the simulation. It is then necessary to validate the chosen potential by first calculating basic properties such as melting temperature, thermal conductivity and elastic constants. Nevertheless, softwares have been created to enable the proper development (testing and standardisation) of potentials. These include potfit [93], KLIFF [94] and Atomicrex [95]. Potentials are also available for a wide variety of material choices (metals, semiconductors, oxides, carbon, etc.) on sites such as Interatomic Potentials Repository (NIST) and the Knowledgebase of Interatomic Models (OpenKim) [96].

2.3 Simulation

2.3.1 Integrators

Many methods are available to integrate the equations of motion including leapfrog, predictor-corrector, Verlet, etc. Each is characterized by its own accuracy and efficiency. Among them, the velocity Verlet algorithm stands out for its efficiency, stability, convergence and low truncation error at long simulation times. This method is divided into two steps. The first step consists in computing the velocity at a half time-step:

$$v_i(t+\frac{dt}{2}) = v_i(t) + \frac{dt}{2}a_i(t) \tag{2.10}$$

Positions and velocities of atoms are computed at the next time step:

$$v_i(t+dt) = v_i(t+\frac{dt}{2}) + \frac{dt}{2}a_i(t+dt)\,, \tag{2.11}$$

$$r_i(t+dt) = r_i(t) + dt\,v_i(t+\frac{dt}{2})\,. \tag{2.12}$$

2.3.2 Statistical ensembles

The "natural" ensemble for molecular dynamics simulations is the micro-canonical ensemble (NVE). In this ensemble, the system is isolated, i.e. there is no exchange of energy with the external environment. The number of atoms N, the volume V and the total energy E of the system are constants. Sometimes, it is desirable to be able to control the temperatures and pressures of a system to ensure that simulations more closely reproduce physical and chemical experiments. It is thus necessary to modify the equations of motion to allow the system to exchange energy with a larger external system commonly referred to as a "thermostat". Different methods have been developed to ensure temperature control such as velocity scaling [97], the Berendsen thermostat [98], the Andersen thermostat [99] or the Nosé-Hoover thermostat [100, 101]. In this work, we principally used the Nosé-Hoover (NH) formalism in which a friction term, ζ, is added to the equations of motion:

$$f_i(t) = m_i\frac{d^2r_i(t)}{dt^2} - \zeta m_i v_i\,. \tag{2.13}$$

The temperature is then controlled by the difference between the actual kinetic energy (E_c) of the system and the "target" kinetic energy (E_c^{target}). When E_c is greater than E_c^{target}, the kinetic energy drops and vice versa when it is lesser. The dynamic friction term $\dot{\zeta}$ is linked to the kinetic energy by:

$$\dot{\zeta} = (E_c - E_c^{target})/Q_T \tag{2.14}$$

where Q_T is the mass parameter of the thermostat that determines the degree of coupling of the system thermostat. In other words, it determines how rapidly the temperature is relaxed. The ensemble using this method is the canonical ensemble (NVT) with the number of atoms N, the volume V and the temperature T as constants. However, other simulations require controlling the pressure and therefore varying the volume. The Nosé-Hoover approach also makes it possible to introduce a barostat to act on the pressure. The approach consists in introducing a degree of freedom acting on the volume of the simulation box by:

$$\dot{V} = (P - P^{target})/Q_P \tag{2.15}$$

with V the volume and Q_P the response speed of the barostat. The corresponding thermodynamic ensemble is isoenthalpic-isobaric (NPH) with constant atomic number N, pressure P and enthalpy H. When a thermostat and barostat are considered, the simulations are performed in the isothermal-isobaric ensemble (NPT). This ensemble allows the system to adjust its volume and to control the temperature through pressure and kinetic energy.

Moreover, certain simulations have been carried out using a Langevin thermostat. The principle remains similar to that of an Nosé-Hoover thermostat: it consists in adding a term to the equations of motion according to a Gaussian probability. This thermostat is no longer deterministic but rather stochastic.

2.3.3 Boundary conditions

Molecular Dynamics simulations are usually limited to system sizes of a few hundred nanometers (sub-micrometers). Therefore, periodic boundary conditions are applied to overcome finite size effects, the system becoming pseudo-infinite. The application of periodic conditions considers the simulation box as a primary cell. This cell is replicated in all directions (x,y,z) by images with the same properties (number of atoms, position of atoms, moment of atoms, size and geometry) as shown in Fig. 2.4. If an atom leaves the primary cell, it will re-enter from the opposite side. Note that an atom must not interact with its image. Therefore, the size of the primary cell must be at least 2 times larger than the cut-off radius of the interatomic potential (i.e., the minimum distance for which the attractive part of a potential is zero).

2.3.4 LAMMPS software

In the present work, we used the large-scale massively parallel atomic/molecular simulator (LAMMPS) that was developed since 1995 at the Sandia National Laboratory to simulate the time evolution of a very large number of atoms [103]. This open-source software is widely used to simulate a large variety of materials such as metals, semi-conductors and even biomolecules or polymers. LAMMPS is computationally efficient as it supports most parallel technologies such as MPI, Open MP, Cuda, etc.

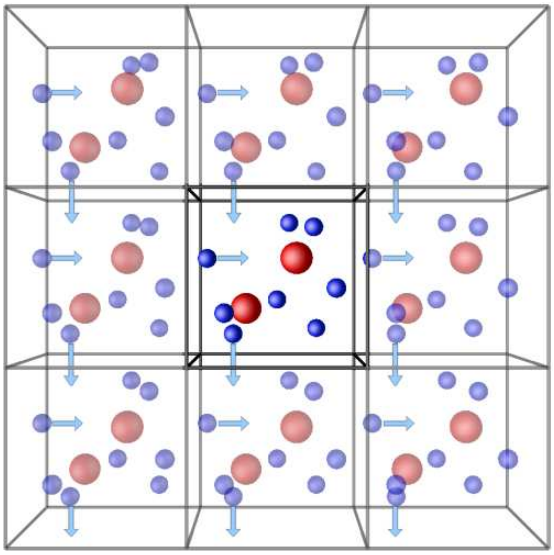

Figure 2.4: Schematic representation of the Periodic Boundary Conditions (PBC). From [102]. The central cell is replicated in all directions by images with the same properties (number of atoms, position of atoms, moment of atoms, size and geometry).

It is also possible to build on LAMMPS as a library to include or couple with many codes to extend its range of application. Moreover, LAMMPS incorporates state of the art methods thanks to an active developers' community, allowing specific commands to be improved or added.

2.4 Post-processing

2.4.1 Analysis

Analysis of simulation data is necessary to detect elementary mechanisms at the nanoscale. One of the keys to better understanding such mechanisms is to visualise the atomic displacements using visualisation software such as Ovito [104]. Ovito reads atomic coordinates and individual properties of atoms in order to visualise the structure at different times during the simulation. This is free-distribution software that incorporates a wide variety of analysis methods such as crystalline structure, the radial distribution function, atomic trajectory and cluster analysis, among others.

• Structure analysis

Many methods are available to identify crystalline structures, each with its own specificity and accuracy. In the present work, we have used three different methods to identify the local atomic environment of an atom. The first method is based on the analysis proposed by Ackland and Jones. For an atom i (or central atom), the Ackland and Jones analysis calculates the number of neighbors and the angles with the central atom to determine whether its structure is *hcp, bcc, fcc* or amorphous [105]. The advantage

of the Ackland and Jones analysis is that it is less sensitive to thermal fluctuations than other methods because it considers the angles between atoms and not their distances. However, characterisation in the liquid phase is difficult as many atoms are recognised with a defined structure even when amorphous.

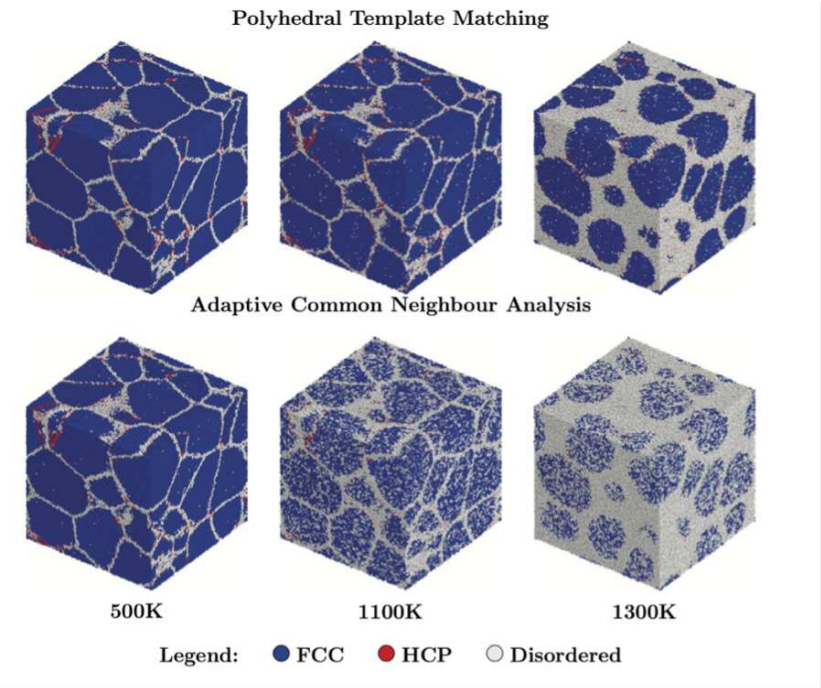

Figure 2.5: Comparison between a-CNA and PTM. From [106].

Another method used below is the Common Neighbor Analysis (CNA) approach [107]. In this method, a central atom is chosen and a sphere is drawn around this atom to select the first neighboring shell. Each pair is then characterized by three criteria: the number of atoms common to both atoms, the number of bonds between their common neighbors and the number of bonds in the longest chain among the common neighbors. The criteria are then compared to reference structures to identify the structure of the chosen atom. The adaptive Common Neighbor Analysis (a-CNA) is an evolution proposed by Stukowski to study binary systems [108]. However, a-CNA sometimes leads to certain ambiguities in the identification of the structure, particularly in the presence of thermal fluctuations or stresses.

Finally, the last and most robust Polyhedral Template Matching (PTM) method allows for the identification of crystalline structures with less noise than the other methods [106]. This method is divided into two steps: a graph isomorphism test is used to identify potential structure matches. Then, the deviation is calculated between the local structure (in the simulation) and a model of the ideal network structure. As clearly shown in Fig. 2.5, the PTM method is much more efficient than a-CNA in distinguishing *fcc* and disordered phases in systems at different temperatures.

• Radial distribution function

An efficient method to analyse the structure of a system is the radial distribution function (RDF), g(r). The RDF is defined as the probability of an atom to be located at distance r_0 from another atom chosen as reference (see Fig. 2.6, left). This function is expressed as follows:

$$g(r) = \frac{\rho(r)}{\rho} \tag{2.16}$$

with $\rho = N/V$ corresponding to the average density over the entire system with respect to the total number of atoms N and the volume V. The local density, $\rho(r) = dn(r)/V_{shell}$, corresponds to the probability of finding $dn(r)$ atoms in a small volume (V_{shell}). The volume of the shell of thickness dr is approximated to $V_{shell} = \frac{4}{3}\pi(r_0+dr)^3 - \frac{4}{3}\pi r_0^3 \sim 4\pi r_0^2 dr$. The radial distribution function is efficient in detecting the phases of a system. The crystalline structures exhibit defined peaks corresponding to the neighbor shells. In the solid phase, the peaks are separated from each other, even at long-range order. The liquid or amorphous phases are characterized by a smoothing of the peaks at long-range order and by a broad peak at short-range order (see Fig. 2.6, right). Moreover, RDF can provide information about the progressive amorphization of a system or about the local rearrangement of atoms.

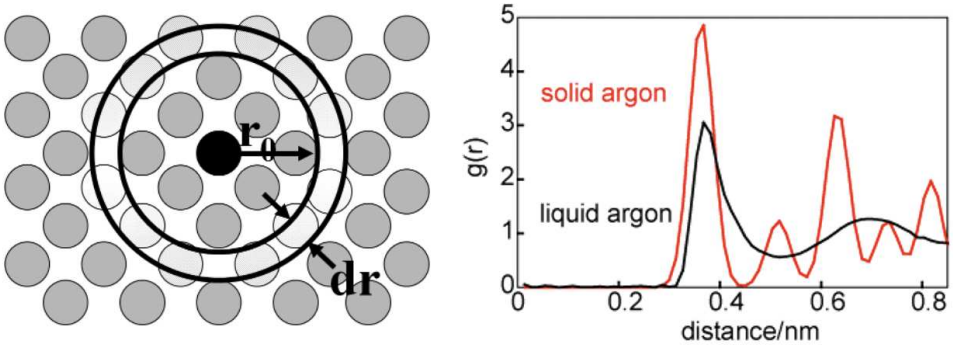

Figure 2.6: On the left, 2D representation of the radial distribution function (RDF). The black atom in the center is the atom of reference. dr is the thickness of the shell located at distance r_0 from the atom of reference. On the right, typical RDF for the liquid phase and solid phase (here the Argon from [109]).

• Degree of mixing

The degree of mixing is a powerful method to analyse the level of mixing between different elements at short-range order. The first step is to define the limit distance (r_{cut}) between the short-range order and the long-range order (see Fig. 2.7). This distance is chosen such as to be superior to first neighbor shells for fcc, hcp and amorphous atoms and superior to the first and second neighbor shells for bcc atoms. This criterion is defined via the radial distribution function. The short-range order parameter is therefore

introduced to follow the degree of mixing during the simulation by:

$$\Omega = \frac{\frac{c}{1-c}N_i^j + \frac{1-c}{c}N_j^i}{N_i^j + N_j^i} \tag{2.17}$$

with Ω the chemical mixing of the system, c the atomic fraction and N_i^j the average number of neighbors of type j in the sphere of radius (r_{cut}) around atoms of type i (and vice-versa for N_j^i). These atoms are considered in the zone of mixing between the different elements.

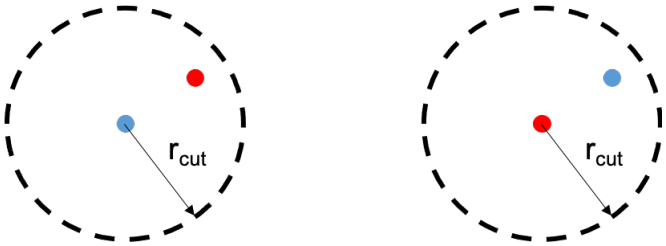

Figure 2.7: 2D representation of the atoms considered in the mixing zone. Red and blue atoms represent the atoms of type i and j, respectively. Dashed lines represent the distance r_{cut} between short- and long-range orders.

• Number density profiles

The number density profile (NDP) is an analytical tool which provides abundant information about the dynamics in multiphase systems. NDP consists in dividing the space into several bins of a constant thickness. Then, the number of atoms is calculated in each bin with respect to the type of atoms. The thickness needs to be sufficiently large in order distinguish the different crystalline planes but low enough to be accurate. In the ideal case, the thickness is chosen to be slightly lower than the interplanar distance. The NDP provides useful information about the ordering at the interface between two phases, the formation of crystalline phases (such as intermetallic phases, for example), the stoichiometry and the amorphization.

Note that other 2D profiles such as temperature profile or fcc fraction profile can be obtained in a way similar to the NDP approach. The difference is essentially the way in which the variables of interest in each bin are computed. Indeed, these variables are calculated with the average over each bin, providing accurate information about the location of interfaces, the width of interfaces, local transformations, increases in temperature, etc.

2.4.2 Calculations of specific properties

As mentioned in Section 2.2.3, interatomic potentials are fitted with a limited database of properties determined experimentally or with ab-initio calculations at zero or room

temperature. The calculations of specific properties (e.g. Melting temperatures, thermal conductivities, latent heat of fusion, solid/liquid interface energy, lattice parameters, solid/liquid interface velocities) that were not explicitly fitted allowed us to evaluate the potential transferability at high temperature. Also, these values determined with atomic simulations will later serve as inputs in models based on the classical nucleation theory (CNT) that is well established. The use of CNT with values determined by MD calculations allow us to extend our results to large scale systems. Last but not least, this procedure also demonstrated that the classical nucleation theory that was developed at micro/macro-scale still to be valid at atomistic scale.

• Latent heat of fusion of Ni

In order to estimate the latent heat of fusion, L_V, we considered a bulk system of 5.28 nm $\times$ 5.28 nm $\times$ 5.28 nm at zero pressure, thermalized at $T = 100$ K. Periodic boundary conditions were imposed in all directions. The sample was then heated with a temperature ramp of 50 K over 50 ps in the NPT ensemble, and then relaxed at constant temperature in the NPT ensemble over 50 ps, and in the NVT ensemble over 10 ps. Quantities were measured in the NVE ensemble over 10 ps. The corresponding average heating was ~ 450 K/ns. This procedure was repeated until complete melting of Ni at 3000 K. Note that the melting temperature of the bulk is higher than the thermodynamic melting temperature (T_m), because the crystal is perfect, without any free surfaces or imperfections. The system was then cooled with a temperature ramp similar to that imposed for the heating process. A rough estimation of the melting temperature, $T_m = T_+ + T_- - \sqrt{T_+ T_-}$, is deduced from the temperature for the maximum degree of superheating (T_+) and supercooling (T_-) [110].

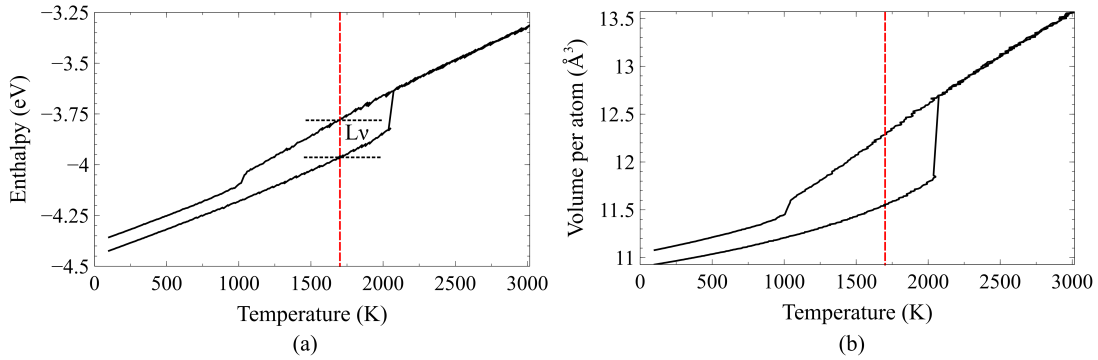

Figure 2.8: (a) Enthalpy as a function of temperature. (b) Volume per atom as a function of temperature. Latent heat of fusion L_V and volume per atom V_{at} are evaluated at melting point (dotted red line).

The latent heat of fusion is determined at the melting point of the bulk system (1701 K) as the difference between the enthalpy of the solid phase and the enthalpy of the liquid phase. The latent heat of fusion is estimated at 22.00 10^{-2} eV, equivalent to

21.23 10^6 J/kmol (Fig. 2.8a). The experimental reported value in the range between 17.03 10^6 J/kmol and 18.90 10^6 J/kmol [111] is slightly lower than the value measured in MD. The volume per atom (V_{at}) is estimated at 11.55 Å^3 (Fig. 2.8b) at the melting temperature of Ni (1701 K, value of the potential [112]).

The molar volume is $V_m = V_{at} \times N_A = 0.006955$ m^3/kmol. Note that the molar volume estimated with the potential at ambient temperature 0.006612 m^3/kmol is close to the experimental value 0.006590 m^3/kmol. Finally, the latent heat of fusion, L_V, expressed in appropriate units, is equal to 21.23 $10^6/V_m$ = 3.052 10^9 J/m^3. This value slightly differs from the experimental estimation (2.530 10^9 J/m^3). Nevertheless, this indicates good adequacy of the potential to determine the latent heat of fusion.

• Velocity of the solid/liquid interfaces of Ni

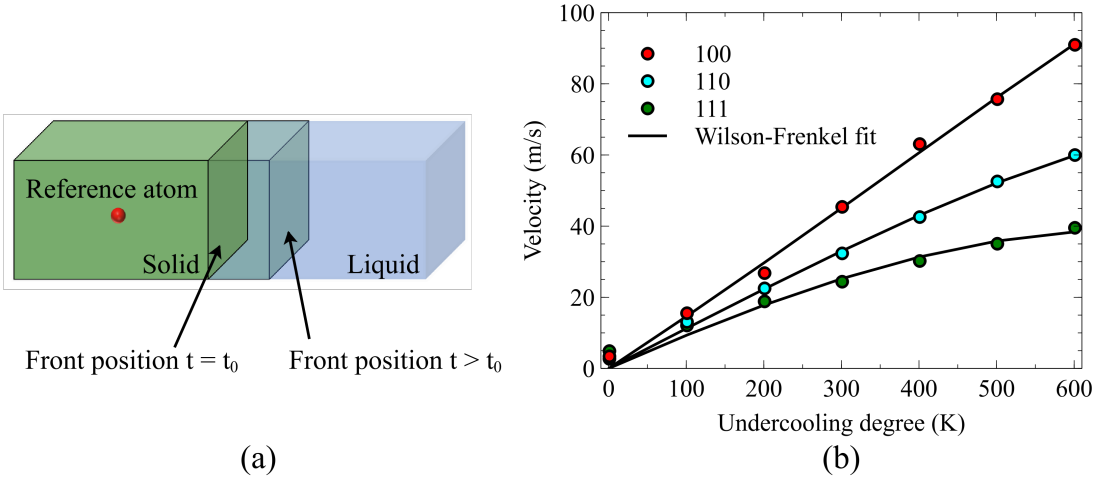

Figure 2.9: (a) Schematic representation of the system. (b) Solid/liquid interface velocity of the three orientations (100), (110), and (111) as a function of the degree of undercooling.

Two-phase systems were considered, with a solid/liquid interface perpendicular to the x direction. The crystallization velocity of Ni was determined for three orientations (100), (110), and (111) of the solid/liquid interface. The following procedure was considered:

1. We built a *fcc*-Ni system elongated in the x-direction at the target temperature T, with the appropriate lattice parameter and orientation. Typical sizes ($L_x \times L_y \times L_z$) of the system for the orientation (100), (110), (111) were 85.36 $\times$ 4.27 $\times$ 4.27 (nm), 120.71 $\times$ 6.04 $\times$ 4.27 (nm) and 147.84 $\times$ 6.03 $\times$ 6.97 (nm), respectively. Periodic boundary conditions were imposed in all directions. The whole system was then relaxed at the target temperature T in the NPT ensemble for 1 ns.

2. One half of the sample was frozen and the other half (i.e between 0 and L_x/2) was melted in the NPT ensemble for 1 ns at a temperature $T_{\text{sup}} = 3000$ K, much

higher than the melting temperature estimated with the EAM potential, in order to ensure complete melting and produce a liquid phase.

3. Finally, the simulation was carried out in the NPT ensemble for 2.5 ns at the target temperature T for the whole system. If the target temperature is below the melting temperature ($T_m = 1701$ K), the interface moves toward the right and the system crystallizes (Fig. 2.9). If the target temperature T is above the melting temperature, a melting front propagates to the left and the system melts completely.

We considered 7 target temperatures below the melting temperature: 1100 K, 1200 K, 1300 K, 1400 K, 1500 K, 1600 K, and 1700 K. In order to estimate the solid/liquid interface velocity, the front position was followed and compared to the position of a reference atom in the solid phase (Table 2.1). We observed that the solid/liquid interface velocity depends on the degree of undercooling. The Wilson-Frenkel model was used to approximate temperature dependence:

$$v = K\frac{T_m - T}{T}\exp\left(-\frac{Q}{k_B T}\right) \tag{2.18}$$

where Q is the activation enthalpy, k_B is the Boltzmann constant, and K is a constant. In addition, the crystallization velocity $v\,(100) > v\,(110) > v\,(111)$ is consistent with the sequence, reported in the literature.

The two-phase method gives also the melting temperature of the material. The target temperature is chosen around the estimated melting temperature. If the temperature is below the melting temperature, the solid phase grows. If the temperature is above the melting temperature, the liquid phase invades the entire system. The melting temperature is estimated as the temperature for which the solidification/melting front is stagnant.

T (K)	v (100)	v (110)	v (111)
1100	90.95	59.98	39.53
1200	75.68	52.56	35.05
1300	63.07	42.55	30.20
1400	45.41	32.34	24.38
1500	26.80	22.51	18.85
1600	15.53	13.09	12.08
1700	3.41	2.71	4.89

	100	110	111
K	488.1	531.2	775.1
Q (J)	$1.63\,10^{-20}$	$2.41\,10^{-20}$	$3.65\,10^{-20}$

Table 2.1: Left: Crystallization velocity (in m/s) calculated with the two-phase method at different temperatures and for different interface orientations. Right: Wilson-Frenkel parameters obtained from the fit by eq. (2.18).

• Solid/liquid interfacial energy of Ni

In order to estimate solid-liquid interfacial energy γ_{SL}, we built a pseudo 2D system with a solid Ni cylinder surrounded by liquid Ni. Periodic boundary conditions were

imposed in all directions. The entire sample was thermalized at a target temperature in the NPT ensemble for 200 ps, followed by the NVT ensemble for 100 ps. The liquid phase around the cylinder was introduced by heating the liquid region in the NPT ensemble for 200 ps and the NVT ensemble for 100 ps to 2500 K (Fig. 2.10a). The entire sample was then maintained in the NPT ensemble for 5 ns at the target temperature. Several radii were considered: 1.79 nm, 3.58 nm, 7.17 nm, 14.34 nm, and 17.93 nm. Given a particle radius, we chose a large set of target temperatures in order to find its melting point.

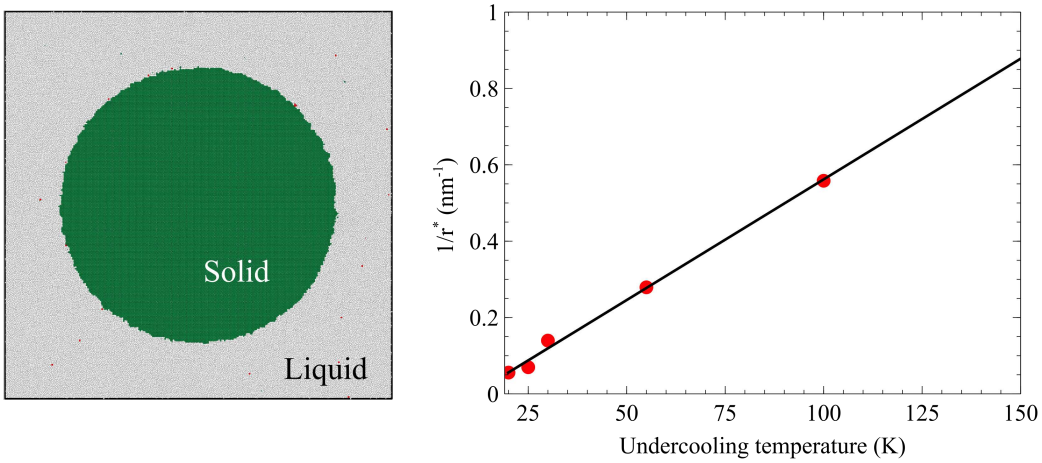

Figure 2.10: (a) Snapshot of the solid particle, in green, surrounded by the liquid, in gray. (b) Inverse of the critical radius as a function of the degree of undercooling. Red dots are the simulation results. Black curve is the fit used for the interfacial energy estimate

According to the classical nucleation theory, since there is no interaction between solid and liquid for the flat face of the cylinder, the Gibbs free energy for a cylinder can be expressed as $\Delta G = -\pi r^2 h \Delta g_V + 2\pi r h \gamma_{SL}$, where h is the cylinder height, r the cylinder radius, and Δg_V is the Gibbs free energy per volume unit. The critical radius r_c is obtained when the first derivative of the Gibbs free energy is zero. Moreover, Δg_V can be approximated by $\Delta g_V \sim L_V \Delta T / T_m$. The critial radius r^* is then expressed as $r^* = (\gamma_{SL} \times T_m)/(L_V \times \Delta T)$, where $\Delta T = T_m - T$ the degree of undercooling at which the cylinder melts. By considering the values of latent heat and the melting temperature, the simulation results were fitted by this expression in order to obtain the solid-liquid interfacial energy γ_{SL} = 284 mJ.m^{-2} (Fig. 2.10b).

• Phonon thermal conductivity of Ni

Phonon thermal conductivity was computed with non-equilibrium molecular dynamics (NEMD) [116]. We considered a periodic simulation box elongated in the z direction, with a cross-section of 20 $\times$ 20 lattice units (i.e. 7.04 nm $\times$ 7.04 nm). This system was equilibrated at T in an isothermal-isobaric ensemble (NPT) over 0.2 ns. Then it was divided into 20 bins. The first bin defines the hot region maintained at $T + 50$ K,

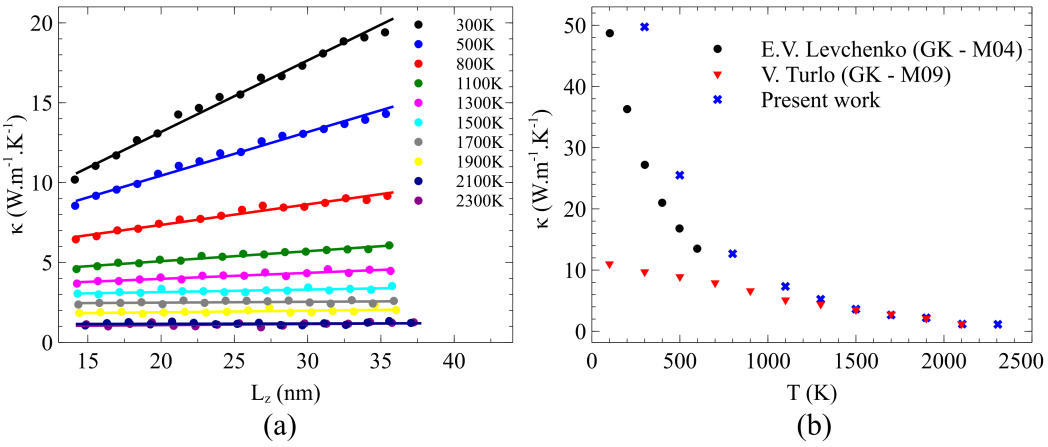

Figure 2.11: (a) κ as a function of the simulation box length for the considered temperatures. Symbols are the numerical results. Lines are the corresponding fits. (b) Bulk thermal conductivity results as a function of temperature compared with the values reported by Levchenko *et al.* [113] and Turlo *et al.* [114] . These two authors computed κ with the Green-Kubo approach, using Mishin 2004 (M04) [115] and Purja Pun and Mishin 2009 (M09) [112] potentials for Ni.

while the middle bin (i.e. 11) is the cold region thermalized at $T-50$ K. Two distinct Langevin thermostats were used. The Langevin damping parameter was set equal to 0.1 ps. The equations of motions of the atoms outside the thermostated regions were integrated into the NVE ensemble. A run of 0.28 ns was long enough to obtain a steady state temperature profile between heat sink and heat source. The energies added/removed by the two thermostats and the temperature profile between the two regions were monitored and averaged for 0.1 nanoseconds. Thermal conductivity was computed using Fourier's law :

$$\kappa = -\frac{J}{dT/dz} \tag{2.19}$$

where J is the heat flux and dT/dz is the thermal gradient between the two thermostated regions. In the case of solids, finite size effects have to be taken into account. The distance between the two thermostats limits the phonons' mean free path that lowers thermal conductivity compared to bulk values. This was overcome by computing thermal conductivity with samples of different lengths. Bulk thermal conductivity was then estimated by extrapolating reciprocal thermal resistivity $1/\kappa$ versus reciprocal system length $(1/L_z)$. Note that, in metallic melts (or liquids) the phonon's mean free path for heat transport is much shorter than the distance between the two thermostats since it is meanly due to collisions between close neighbors. That lead us to simulate between 40 and 100 lattice units (i.e. 14.08 nm to 35.2 nm) along the z-direction and nine temperature values were considered: $T = 300$ K, 500 K, 800 K, 1100 K, 1300 K, 1500 K, 1700 K 1900 K, 2100 K, and 2300 K (see Fig.2.11).

2.5 Non-exhaustive literature review of MD simulations on solidification, mechanical activation and nanocomposite reactivity

In this section, selected Molecular Dynamics studies are presented in order to contextualize the different chapters presented later. Firstly, it allows our work to be situated in relation to other studies already carried out using Molecular Dynamics and, secondly, to be compared with what has already been done. The three main themes of this work will be discussed, namely solidification, mechanical activation and reactivity of Ti-Al.

2.5.1 The solidification process at atomic scale

Various aspects of solidification processes at the nanoscale have already been investigated, namely homogeneous and heterogeneous nucleations, the effect of cooling rates on final microstructure, directional solidification and the calculation of solidification properties.

Many atomistic simulations for numerous materials, including metals, have been undertaken to study homogeneous and heterogeneous nucleations. They have focused on fundamental aspects such as nucleation rates or nucleation barriers (see for instance [117, 118]). Two main procedures for achieving homogeneous nucleation are usually used in MD approaches: at a constant undercooled temperature (isothermal conditions) or by applying a constant cooling to the melt.

• Isothermal homogeneous nucleation

Shibuta *et al.* studied homogeneous nucleation at isothermal undercooled temperatures in large-scale simulations. These authors simulated a billion-atom iron melt with a Finnis-Sinclair potential [119]. They considered two temperatures in order to observe the structural evolutions over time by tracking the number of grains created and their orientation with respect to the (100) orientation (see Fig. 2.12). They demonstrated the formation of grains at the surface of previously formed grains. In parallel, they also investigated homogeneous nucleation in iron for a larger range of temperatures [44, 120]. This work allowed them to follow the nucleation rates, the incubation time for the nucleation as well the microstructural evolution with respect to temperature.

Another notable MD work was published by Mahata *et al.* [45]. They investigated homogeneous nucleation in an undercooled aluminum melt using a MEAM potential. Under isothermal conditions, they derive important values such as critical nucleus size, number of nuclei or induction time. Furthermore, Mahata *et al.* succeeded in comparing their numerical values obtained at constant temperature or with different cooling rates with those of classical nucleation theory.

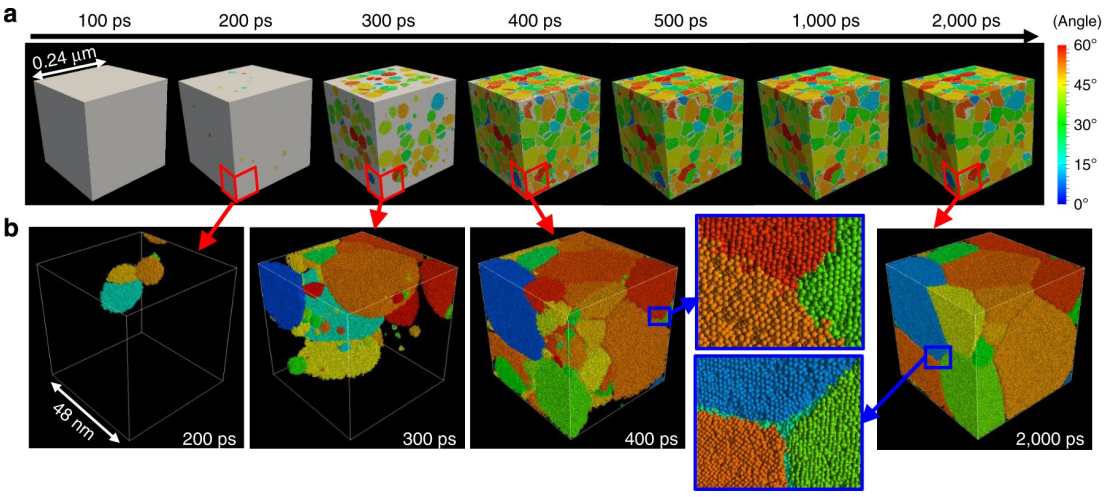

Figure 2.12: Overview of the homogeneous nucleation process in an iron melt at a temperature of 0.67 T_m. From [119]. (a) Representative snapshot of the entire billion-atom simulation box. (b) Zoom on the part of the simulation highlighted by the red box. The white color represents the liquid atoms and the different colors represent relative disorientation with respect to the coordination axis.

• Isothermal heterogeneous nucleation

Few approaches focus on heterogeneous nucleation and unfortunately most of them use pair potentials that are not appropriate for metals [121–123]. Nevertheless, one can cite the approach reported by Fujinaga *et al.* for titanium particles surrounded by liquid aluminium using an EAM potential [46]. This work considered heterogeneous nucleation for various particle geometries and sizes under different isothermal undercooling conditions. Two different cases were characterized: stagnation and free growth. Free growth was observed when the undercooling temperature was sufficiently high with respect to the size of the nucleant particle (Fig. 2.13). Their approach was validated by a direct comparison with the classical theory of nucleation.

• Solidification at different cooling rates

According to solidification theory, the solidified microstructure will vary according to the applied cooling rate. A very fast cooling rate will result in a glassy structure while a slower cooling rate will result in a crystalline structure. In the mid-90s, a pioneering work on aluminium melts was restricted to two cooling rates and the use of pair potentials because of limited computing power [35]. Later on, more systematic studies were carried out to precisely determine the specific cooling rates giving rise to a crystalline or glassy structure on metals and alloys such as Ag [36] with the Sutton-Chen potential, Al [38] or Ti_3Al [37] with EAM potentials. In all of these studies, the initial stage was obtained by heating the system of interest to an equilibrium liquid state ($T > T_m$). Then, several cooling rates were applied to observe the effect of the

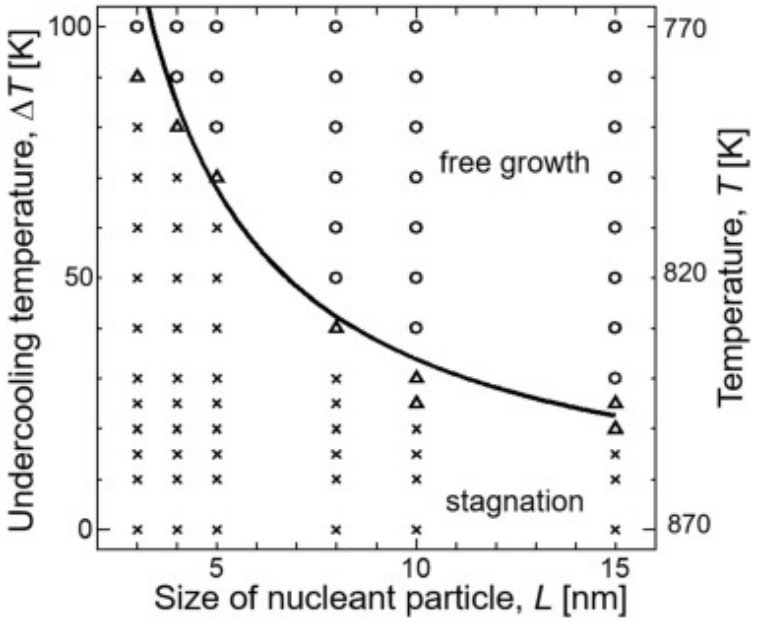

Figure 2.13: Heterogeneous nucleation simulations with titanium particles surrounded by liquid aluminium. From [46]. The crosses represent the stagnation for which the liquid phase remains the same over the entire simulation, the circles represent the free growth of the liquid aluminum on the titanium surface and the triangles the transition from the two preceding behaviors. The solid black line is a fit from the Classical Nucleation Theory (CNT).

cooling rate on the final microstructure (see Fig.2.14).

• Solidification front properties

Molecular dynamics also provides access to characteristic values of the solidification front such as the kinetic coefficient or the solid-liquid interface energy. Neither quantity is easily accessible via experiments and their evaluation requires the use of numerical methods at nanoscale.

The kinetic coefficient expresses the dependence of the interface velocity on the interface temperature. It is particularly important to know this value for the various orientations at which velocities are different. Sun *et al.* and Celestini *et al.* computed the kinetic coefficients for several interface orientations under isothermal conditions in nickel using an EAM potential [40] and in gold using the Glue potential [39]. Both studies considered an elongated system in one direction with a temperature gradient. They observed the difference in velocity of the solid-liquid interface as a function of orientation.

The solid-liquid interface energy has been calculated using different techniques such as the cleaving technique [124], the capillarity fluctuation method [125, 126], theoretical calculation based on density functional theory [127, 128] or the critical nucleus method [129, 130]. An accurate estimation of solid-liquid interface energy is of great

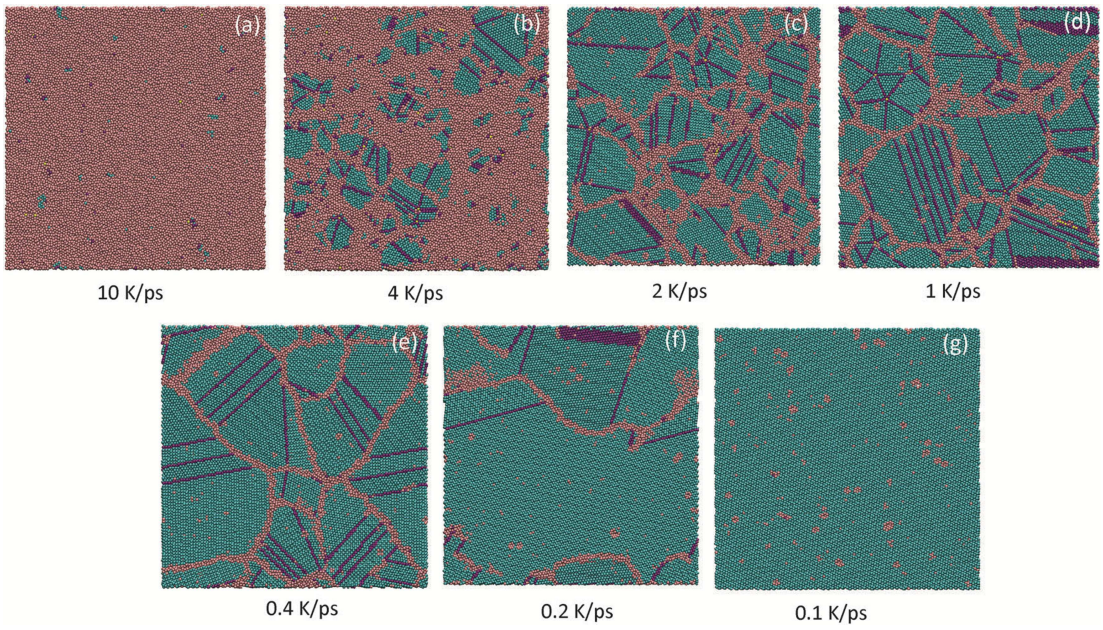

Figure 2.14: Snapshots of the microstructures obtained for different cooling rates on pure aluminum at the final temperature (here 293 K). From [38]. Cyan, purple and pink represent *fcc, hcp* and amorphous atoms, respectively. Crystalline structures are observed for the cooling rates below 4 K/ps. As shown in (a), the fastest cooling rate (10 K/ps) exhibits a glassy structure.

importance as it will serve as an input parameter for more realistic simulations of solidification with, for example, the phase field approach [131].

• Directional solidification

The first work on rapid directional solidification was published by Celestini *et al.* in 2000 [41]. It focused on the growth of a solid binary alloy from its liquid phase. This approach was developed using LJ potentials with an Argon melt containing a random dispersion of solute atoms. Using Non-Equilibrium molecular dynamics (NEMD), the authors established a temperature gradient brought about by heating parts of the system to different temperatures. It was not until much later (*i.e.*, 2019) that studies on rapid directional solidification were carried out on metallic systems. Among these studies, one can mention the studies of Al-Cu alloys [42] (see Fig.2.15) and CrNi-alloyed steels [43].

• Columnar to equiaxed transition in MD

To our knowledge, only one study has dealt with the transition between columnar and equiaxed structures where equiaxed grains are formed by homogeneous nucleation. In this work, the temperature distribution reproduced that observed in additive manufacturing techniques with a temperature rise due to the heating of the laser followed by an

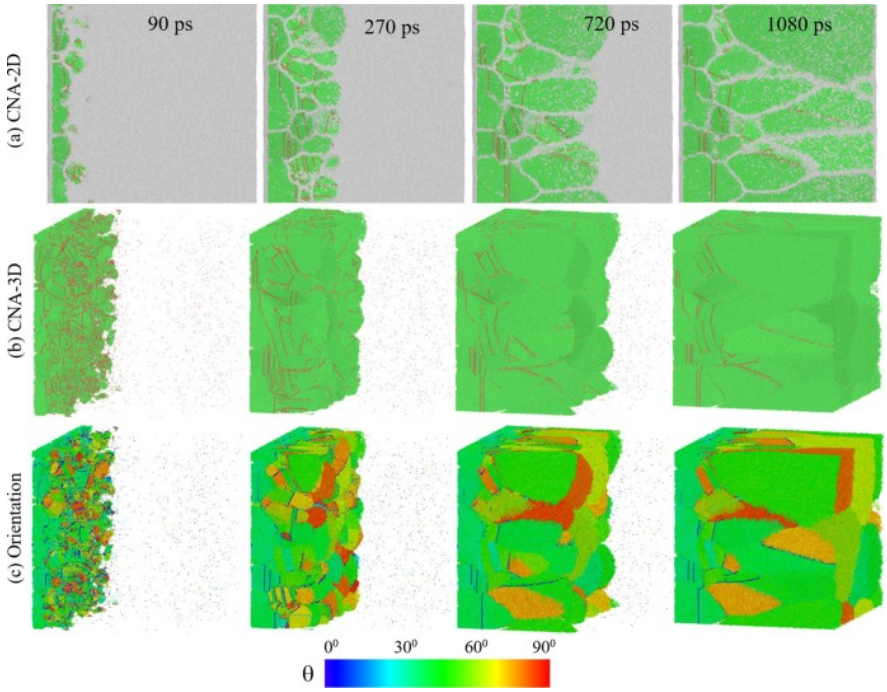

Figure 2.15: Directional solidification on Al-Cu alloys. From [42]. (a) and (b) represent the microstructure evolution (2D and 3D representations, respectively) with fcc atoms in green, hcp atoms in red and amorphous atoms in white. (c) represents the different orientations of grains during solidification.

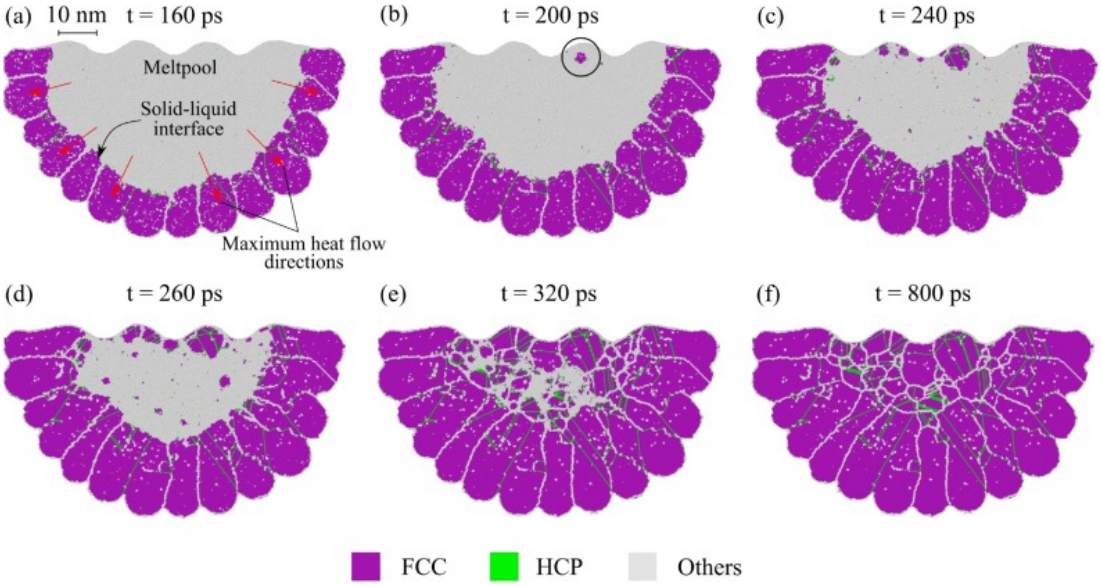

Figure 2.16: Solidification process of laser powder bed fusion technologies on Al powder. From [34].

imposed cooling on a bed of aluminum powder. A finite element approach determined the temperature distribution which served as input parameters for the Molecular Dynamics using Langevin thermostats. This work reported columnar grain solidification in the direction of the hottest point as well as the formation of equiaxed grains close to the surface of the meltpool during cooling (see Fig. 2.16). Further observations were also formulated on porosity, dislocations and cracks [34].

2.5.2 Deformation studied by MD

Most of the studies related to mechanical deformations concentrate on the mechanical properties of materials and very few are related to milling mechanisms. For example, sliding giving rise to friction was studied in [132–134]. These works highlighted the creation of an amorphous mixing zone mainly localized at the interface regions during deformation. Chen *et al.* also studied the slide on an Ni-Al system and observed that the softest material (Al) is the location at which the mixing zone is formed [74]. Plastic deformation induced by milling was also studied by cyclic deformations [69]. In this study, dislocation motions induced the chemical mixing of the elements.

• Mechanical activation

Mechanical activation has been studied in detail by Cherukara *et al.* [75, 76] in the context of the shock loading of a granular material consisting of laminated Ni-Al grains (see Fig. 2.17). The results of this MD work with an EAM potential were reported into two papers. The first one outlines the elementary mechanisms related to the compaction of the system such as stress, temperature and localized velocity increase. The authors also highlighted the importance of pores, which play an important role during collision by locally increasing temperature. Indeed, during the collision of pores, high impact velocities cause the void to be filled with Ni-Al fluid. In the second paper, the influence of different impact velocities on the reaction is discussed. In the case of low impact velocities, the initial voids are filled by the deformation of adjacent grains. The Ni and Al atoms mix only partially, leading to no significant reaction in the sample. In contrast, at high impact velocities, the void filled by the fluid of Ni-Al atoms results in intimate mixing. This mixing induces a localized increase in temperature permitting the adjacent solid grains to melt and thus start the reaction. This reaction, observed at various locations in the sample, then propagates rapidly throughout the sample.

Activating factors determine the increase in reactivity of a mixture due to mechanical treatment. Nevertheless, most of the studies published in the literature have no direct link with mechanical activation but rather isolate mechanisms encountered in mechanical processes giving rise to improved reactivity. For example, Witbeck *et al.* have shown that lattice defects and grain boundaries play an important role in enhancing reactivity [135, 136]. Cherukara *et al.* and Crone *et al.* have highlighted the effects of surfaces [137, 138]. Premixing studies are also used to investigate reactivity. For example, Fourmont *et al.* reported a systematic study on the premixing of lamellar Ni-Al [78]. In this work, various percentages of Ni were artificially added to an alu-

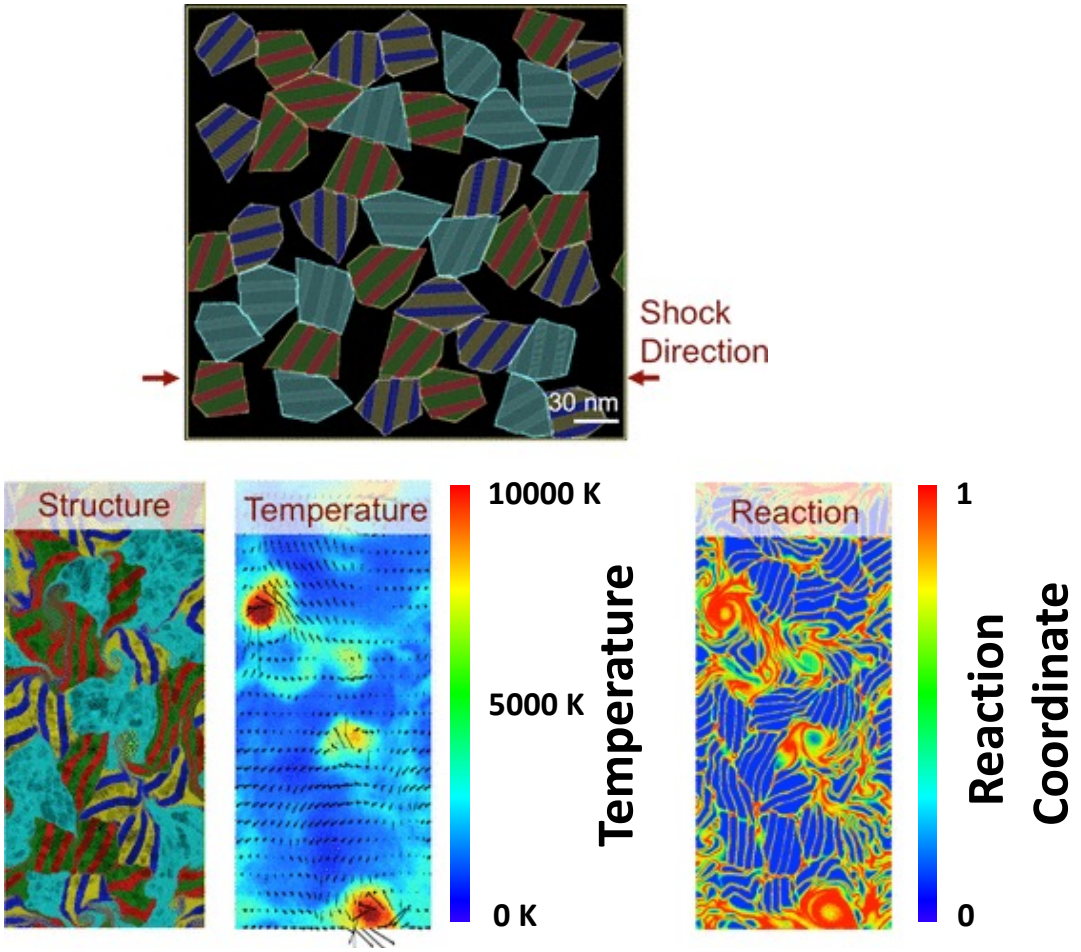

Figure 2.17: Overview of the Cherukara *et al.* study [76]. At top, initial system containing laminated grains of Ni and Al. The arrows represent the direction of the deformation. Below, the final microstructure obtained after deformation with the maps of the temperature and chemical reaction. The two colors within in each grain denote Ni (thin bands) and Al (thick bands).

minium layer surrounded by two nickel layers as might be observed experimentally. In this particular system, the authors reported that premixing at the nanoscale improved reactivity when compared to samples with no premixing.

2.5.3 Reactivity of Ti-Al systems

Many molecular dynamics studies have been performed on the reactivity of metallic systems using geometries such as nanoparticles, nanowires, nanofilms and nanometric multilayers [140]. Indeed, MD is a very pertinent method as it allows observation in-situ of the elementary mechanisms that occur at the nanometric scale, namely melting, dissolution, mixing, phase transformations, microstructure formation, nucleation,

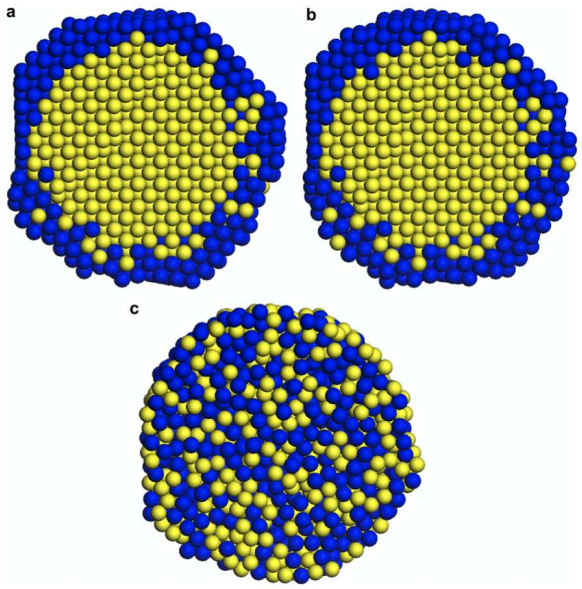

Figure 2.18: Ti-coated Al nanoparticles at 3 different temperatures: a. 900 K, b. 1000 K, c. 1100 K. From [139]. Al is in dark blue and Ti in yellow.

growth of intermetallics, etc. Nevertheless, few studies focus on the particular Ti-Al system.

• Ti-Al coated nanoparticles

Levchenko *et al.* studied the alloying reaction in Ti-coated Al nanoparticles with a particle size of 4.8 nm and an equivalent atomic fraction [139]. They heated their samples to a temperature of 900 K (see Fig. 2.18,a.). At this temperature, the aluminium was completely melted, allowing for the dissolution of Ti in Al(see Fig. 2.18,b. and c.). This dissolution caused an exothermic reaction that raised the temperature to 1352 K in a self-sustaining manner. Finally, after this heat release, the system was cooled down to create a Ti-Al alloy. The authors also compared their study with one they had previously conducted on Al-coated Ti nanoparticles [141]. With similar nanoparticle sizes, they concluded that the interfaces play an important role in reactivity. Indeed, reactivity is better in the Al-coated Ti because the aluminium layer disturbs the structure while in the Ti-Coated Al, the titanium layer is harder and confines the aluminium core.

• Multilayers

Studies on nanoscale multilayers in the Ti-Al system have also been carried out by Kiselev *et al.* [142]. These authors considered a system featuring a Ti layer and an Al layer of equal size, 8 nm in length, 8 nm in width and 2 nm in thickness. The sample was then heated to a temperature of 1000 K, close to the melting point of Al, to start the reaction. They observed that the temperature rise was slow up to 1400 K due to the limited solubility of Ti in Al. From 1400 K, the reaction was accelerated considerably

due to a much higher solubility of Ti in Al in this temperature range. The exothermic reaction was always more pronounced, allowing for a rise in temperature sufficient to reach the melting point of Ti (1700 K). The 2 components then mixed intimately, maintaining a heat release up to 2100 K. The samples were cooled to observe the formation of the Ti-Al intermetallic phase.

Chapter 3

Solidification at nanoscale in the context of Ni additive manufacturing

In the present chapter, we developed MD simulations of pure nickel submitted to typical non-stationary thermal conditions specific to Additive Manufacturing (AM) in order to study the columnar-to-equiaxed transition. Among metals and alloys, nickel-based alloys are commonly used in AM [143]. As this study is restricted to pure metal, the microstructure will result exclusively from thermal effects occurring during solidification processes. The first representative model (model A) was set up to describe the rapid directional solidification of a textured Ni substrate. The second model (model B) was used to investigate the effect of the cooling rate on the evolution of the microstructure. This approach allowed us to assess the effects of process parameters on the resulting microstructure at the nanoscale. In addition, MD simulations were compared to predictions based on the classical theory of solidification of pure metals and on classical nucleation theory.

3.1 Details of the simulations

The simulations were performed using the Embedded Atom Method (EAM) potential, developed by Purja Pun and Mishin for Ni-Al systems [112]. This potential has been extensively used to study reactivity in Ni-Al nanofoils [144, 145]. In addition, this potential is known to reproduce well the physical and thermodynamical properties of nickel [114] (see Table 3.1).

We considered a pseudo 2D system in a simulation box of 100 nm $\times$ 1.4 nm $\times$ 200 nm. As shown in Fig. 3.1, the system was divided into three regions along the z direction: a lower region located between 0 and 20 nm kept at a fixed temperature and named the substrate, a middle region from 20 to 50 nm, and an upper region that was effec-

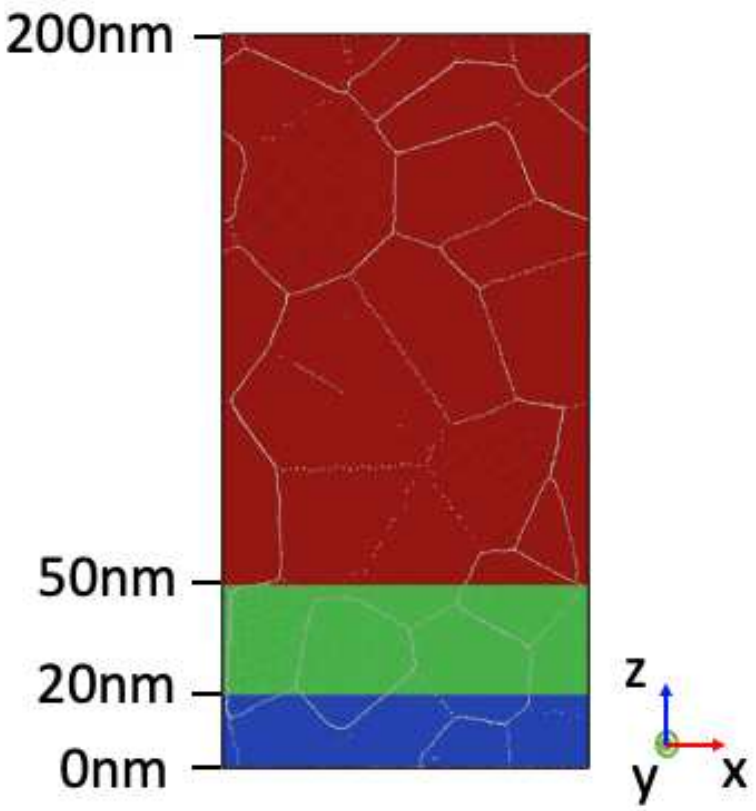

Figure 3.1: Schematic representation of the model. The laser region is represented in red between 50 nm and 200 nm. The substrate region is represented in blue between 0 and 20 nm.

tively affected by the laser beam. The y direction was slightly larger than twice the cut-off distance (r_{cut}) of the potential to avoid multiple interactions. Periodic boundary conditions were applied in the x and y directions, while the boundary condition was nonperiodic and shrink-wrapped in the z direction. The system was built with the Atomsk software [146]. The procedure used to create this polycrystalline sample is analogous to that used to obtain Voronoi cells, which has already been applied in previous works [144, 147]. Each grain had its [010] axis aligned with the y direction and could rotate along the y axis. The equations of motion were integrated using a timestep of 1 fs. The local atomic environment (i.e. *fcc*, *hcp*, or *unknown*) was determined using Polyhedral Template Matching (PTM).

Two representative models were prepared: with and without cooling. Different temperature values of the substrate were considered in order to explore a broad range of microstructures. Typically, the first model (A) allowed us to understand rapid directional solidification in a temperature gradient, without cooling. In the second model (B), a cooling rate was applied to force the system to cool down at a controlled rate, as observed in AM solidification processes (see [43]).

In model A, the system was first equilibrated at T_{sub} for 200 ps in the NPT (isothermal-isobaric) ensemble, followed by another equilibration in the NVT ensemble for 100 ps. After thermalization, the two extremities of the sample were thermostated in an NVT ensemble for 2 ns. The laser region extended from 50 to 200 nm (see Fig. 3.1) and its temperature was set at 1750 K. The temperature of the substrate was set at T_{sub}. Note that, in the central part of the sample, atoms evolved freely as their equations of motion were integrated into the NVE ensemble. After 2 ns, the hot thermostat was removed but the cold thermostat was kept until the end of the simulation. We considered 2 different temperatures for the substrate: T_{sub} = 300 K and 1000 K, in order to consider two very different gradients.

In model B, the system was first equilibrated at T_{sub} for 200 ps in the NPT (isothermal-isobaric) ensemble, followed by another equilibration in the NVT ensemble for 100 ps. After thermalization, the two extremities of the sample were thermostated as in model A. The laser region was set at 1750 K whereas the substrate was set at T_{sub} for 2 ns. Then the laser thermostat was removed and replaced by a temperature ramp corresponding to cooling rates ranging from 75 K/ns to 750 K/ns (see Table 3.2 for more details). The substrate thermostat was kept until the end of the cooling process. At the end of the cooling ramp, which is when the whole system reaches the substrate temperature, T_{sub}, the two thermostats were removed, and the simulation of the entire system was carried out in the NVE ensemble. Six different temperatures of T_{sub} were considered: 800 K, 900 K, 1000 K, 1100 K, 1200 K, and 1300 K.

parameter	symbol	MD	Exp
bulk melting temperature	T_m	1701 K	1728 K
solid/liquid interfacial energy	γ_{sl}	284 mJ.m^{-2}	364 mJ.m^{-2} [a]
bulk latent heat of fusion	L_V	3.052 10^{9} J.m^{-3}	2.35 10^{9} J.m^{-3} [b]
heat conductivity	κ	2.8 W.m^{-1}.K^{-1}	54.182 W.m^{-1}.K^{-1} [c]
lattice parameter	$a(T_m)$	0.35857 nm	
cohesive energy Ni-*fcc*†	$E_0(fcc)$	-4.45 eV	
cohesive energy Ni-*hcp*†	$E_0(hcp)$	-4.43 eV	
atomic volume	$\Omega = a(T_m)^3/4$	11.55 10^{-30} m^3	
atomic mass	m_0	9.75 10^{-26} kg	
molar volume liquid	V_m(liq)		7.43 10^{-6} m^3 [b]
molar volume solid	V_m(sol)		7.13 10^{-6} m^3 [b]
molar mass	M	58.71 10^{-3} kg.mol^{-1}	58.69 10^{-3} kg.mol^{-1} [b]
heat capacity	C_p	655 J.kg^{-1}.K^{-1}	734.4 J.kg^{-1}.K^{-1} [b]
density (solid)	$\rho = m_0/\Omega$	8.46 10^{3} kg.m^{-3}	8.20 10^{3} kg.m^{-3}
heat diffusivity	$D_{\text{th}} = \kappa/\rho C_p$	5.053 10^{-7} m^2.s^{-1}	89.97 10^{-7} m^2.s^{-1}

Table 3.1: Parameters of pure Ni computed with the EAM-09 interatomic potential (Purja and Mishin [112]) and compared to experimental values or thermodynamic calculations ([a] estimated in the review of Jiang and Lu [148] ; [b] Thermo-Calc; [c] Assael *et al.* [149]). Experimental values are given for information only. Most of these values are discussed in Thurnay [111]. Temperature-dependent parameters are evaluated at the bulk melting temperature T_m. † Cohesive energies are evaluated at 0 K.

Molecular dynamics simulations enable characterization of solidification processes by means of thermal effects and nucleation. In order to evaluate quantities such as critical nuclei, nucleation rate, or thermal fluxes, it is necessary to estimate structural parameters (lattice parameter), thermodynamic properties (melting temperature, solid/liquid interfacial energy, latent heat of fusion, heat capacity, etc.) and thermal transport (heat conductivity). For this purpose, we developed separate MD simulations (see Section 2.4.2 for more details). The parameters for Ni are reported in Table 3.1. The structural order of the Ni crystalline phase is *fcc*. The temperature evolution of the lattice parameter a_0 was evaluated, and its value at melting point, $a(T_m)$, is reported. The melting temperature was determined with the isothermal two-phase method. The heating-cooling cycle procedure was used to obtain the other thermodynamic properties: the bulk heat of fusion L_V and the heat capacity C_p (see Section 2.4.2). The heat capacity, which is proportional to the slope of the relative dependence of the enthalpy on temperature, was in good agreement with experimental data. Reasonable agreement between experimental value and MD calculation was also obtained for the latent heat of fusion. The huge discrepancy between the experimental and MD data for heat conductivity can easily be understood if one considers that the conduction of heat observed in this MD study with the classical potential accounts only for phonon transport and does not account for electronic transport. In the present approach, phonon thermal conductivity was computed with non-equilibrium molecular dynamics (NEMD) (see Chapter 2.4.2 for details). In the case of our Ni system, the MD value led to an effective characteristic length of heat conduction that was shorter than the real one by a factor $\sqrt{D_{\text{th}}^{\text{MD}}/D_{\text{th}}^{\text{exp}}} = 4.2$. This can be considered as an asset in simulations because we can investigate thermal effects on MD scales, which allows the refinement and validation of existing theories and the development of new theories for nanoscale systems [150]. After the theoretical model has been refined, experimental values for material properties can be inserted to generate reliable predictions, which can be further validated experimentally. In addition, such theoretical models solved analytically or numerically are much more computationally efficient, which allows us to cover much greater length and time scales, well beyond the MD capabilities. The solid-liquid interfacial energy γ_{sl} was determined using the critical nucleus method [129]. Details are given in Section 2.4.2.

In AM, laser heating imposes dynamic temperature conditions that affect the solidification process. In order to understand their influence on microstructure formation, we first considered the role of a temperature gradient between the solidified material and the melt pool (model A). Next, we introduced the effect of global cooling (model B).

3.2 Solidification under free cooling (model A)

After the complete melting of the upper region through laser heating, the system was divided into 3 regions: a polycrystalline substrate from 0 to 20 nm maintained at T_{sub},

a melt pool at 1750 K ($> T_m$(Ni)), and a solid region between the two (middle region). The resulting temperature profile at t = 0 ns, after the passage of the heat source, is depicted in Fig. 3.2, showing that the steep temperature gradient in the solid part was established between 20 and 80 nm. The abrupt decrease in the fraction of *fcc* atoms in Fig. 3.2 corresponds to a solid/liquid interface. In the specific initial microstructure of this simulation, the system was composed of three columnar grains at the interface, as shown in the snapshot at $t = 0$ ns.

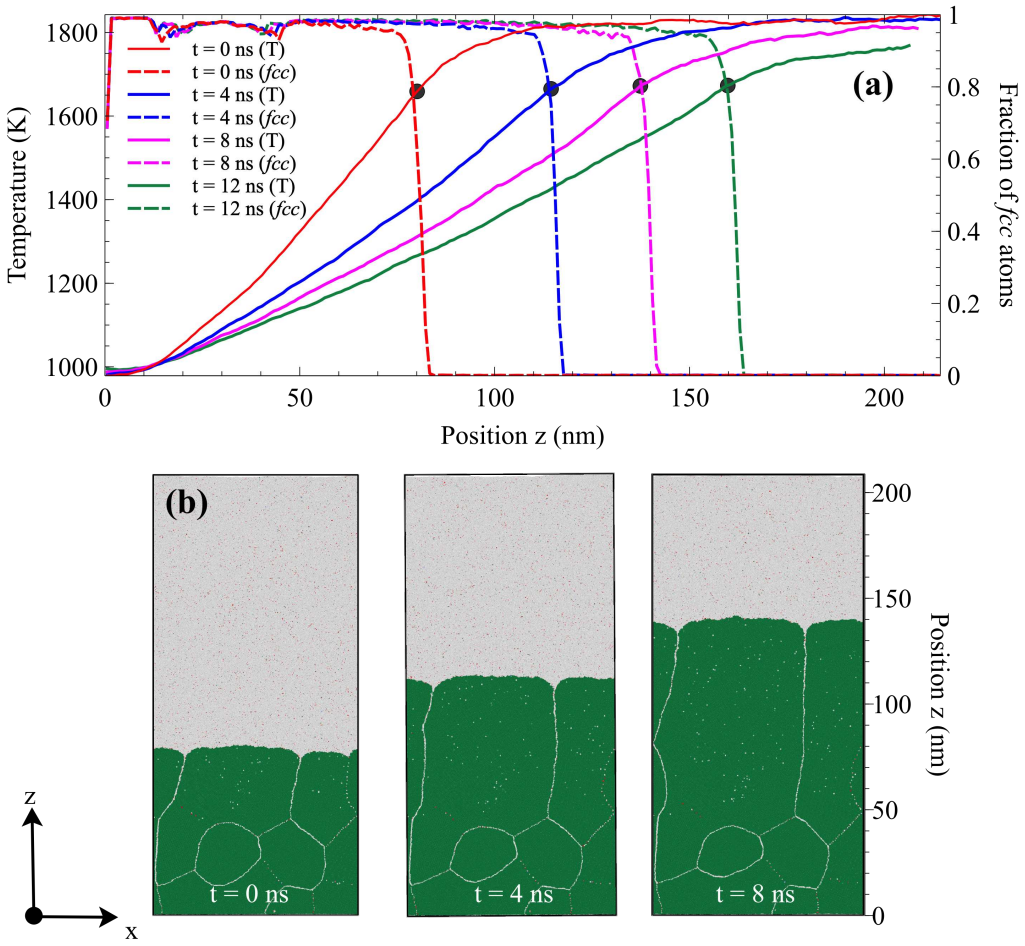

Figure 3.2: System (model A) with a substrate maintained at $T_{sub} = 1000$ K. (a) Temperature profiles (solid lines) and the fraction of *fcc* atoms (dashed lines) at different moments in time. (b) Snapshots of the system at 0, 4, and 8 ns.

After the release of the thermostat from the melt pool, solidification proceeded with propagation of a planar solid/liquid interface in the z direction. We observed that the melted region shrank while the solidified region increased. This progressively induced a smoother temperature gradient in the solidified region. As one can see in Fig. 3.2, the fraction of *fcc* atoms in the solid region is not strictly equal to 1 because of grain

boundaries and point defects. Thus, the thickness of the front was measured as the zone with a fraction of *fcc* atoms between 0.02 and 0.95, which never exceeded 10 nm. The position of the solidification front, associated with the decrease in the fraction of *fcc* atoms, was defined as the point where the fraction of *fcc* atoms is equal to 0.8. This intersection corresponds to 1650 K, which is slightly lower than the melting point of Ni (1701 K). The resulting position of the solid/liquid interface is plotted in Fig. 3.3 as a function of time for two distinct substrate temperatures of 300 K and 1000 K. The crystallization velocity was found to be strongly dependent on the temperature of the substrate but with common features, including a change in slope after some time. By analyzing the regions with linear time dependence on the position of the solid/liquid interface, we extracted the corresponding solidification velocities, listed in Fig. 3.3. During a transient period (before 3 ns for $T_{\text{sub}} = 300$ K and 5 ns for $T_{\text{sub}} = 1000$ K), the instantaneous velocities were larger than the stationary ones by 2.5-3 m/s. In the stationary regime, the solidification front velocities were reduced to 11.5 m/s for $T_{\text{sub}} = 300$ K and 5.5 m/s for $T_{\text{sub}} = 1000$ K, suggesting a linear relationship between substrate temperature and steady-state solidification front velocity. Extrapolating the linear trend set by these two points to zero velocity would result in a temperature of 1642 K, close to the melting temperature of Ni (1701 K).

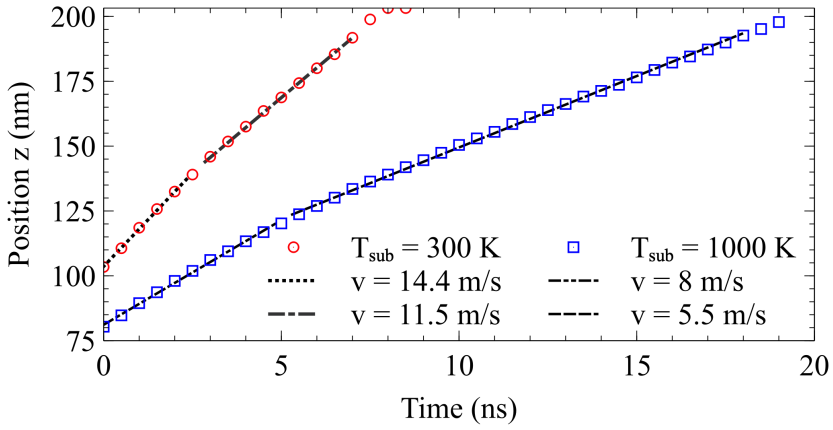

Figure 3.3: Position of the solid/liquid interface as a function of time in the polycrystalline system (Model A) with a substrate at 300 K and 1000 K.

Solidification in pure metals is entirely controlled by thermal processes [151]. In the absence of convection, the latent heat of solidification released during solidification is transported by conduction away from the solid/liquid interface. Conduction can take place through either the solid or the liquid, depending on the temperature gradients at the interface. For solid growth at a velocity v with a planar interface, the balance between heat flow through the solid, heat flow through the liquid, and latent heat released at the interface reads

$$\kappa_{\text{sol}} G_{\text{s}} = \kappa_{\text{liq}} G_{\ell} + v L_V \tag{3.1}$$

where $G_s = \left(\frac{dT}{dz}\right)_{sol}$ is the local temperature gradient in the solid, $G_\ell = \left(\frac{dT}{dz}\right)_{liq}$ is the local temperature gradient in the liquid, and L_V is the latent heat of fusion. In Model A, the liquid is superheated, and temperature gradients at the interface in the liquid and the solid are both positive. If we assume that thermal conductivity is very similar in the liquid and in the solid $\kappa_{sol} = \kappa_{liq} = \kappa$, eq. (3.1) gives an estimate of the velocity v:

$$v = \frac{\kappa}{L_V}\left[G_s - G_\ell\right] \tag{3.2}$$

Since the local gradient in the melt pool is weak, the velocity mainly depends on the temperature gradient in the solidified region. The relationship (3.2) explains why the velocity is greater at the beginning of the solidification process when the gradient is steeper (see Fig. 3.3). We also understand why the crystallization velocity increases for decreasing substrate temperatures, since the temperature gradient is larger in this case.

In MD studies, the crystallization velocity is usually estimated at constant temperature using the two-phase method [112]. The crystallization velocity as a function of temperature and interface orientation was evaluated using this method (see Section 2.4.2). The velocity depends on the orientation of the Ni interface: $v(001) > v(101) > v(111)$ and the degree of undercooling. The difference in velocity as a function of orientation becomes smaller as it approaches the melting temperature. In the case of directional solidification, investigated in the present work, we estimated the solidification velocity as a function of orientation in the case of an initial system composed of a single grain. The velocity was almost the same for the three orientations: $v(001) \sim v(101) \gtrsim v(111)$. This is not surprising because the solid/liquid interface corresponds to a temperature value close to melting point. It is also supported by the fact that the velocities measured in the polycrystalline samples (see Fig. 3.3) are in the same range as the crystallization velocity measured by the two-phase method between 1600 K and 1700 K. It is also important to note that the interface (111) was the least mobile and, thus, was not considered in our polycrystalline sample, as crystal rotations around the direction [010] did not allow us to establish such an interface. The crystallization velocity in the case of directional solidification (model A) in polycrystalline samples is fixed by the temperature gradient rather than by the temperature value at the solidification front or by the grain orientation. This observation corroborates the fact that the front remained flat in the case of a polycrystalline system.

3.3 Solidification under imposed cooling rate (model B)

In Model B, a progressive global cooling was imposed in order to mimic the thermal conditions experienced during AM. As in the previous model, A, the system was composed of a substrate maintained at a given temperature, T_{sub}, a melt pool, and a solidified region between the substrate and the melt pool (middle region). Both the so-

T_{sub} (K)	α (K/ns)	morphology	t_1 (ns)	t_2 (ns)	ΔT (K)	ΔL_z (nm)
800	750	C+E	1.27	1.00	551	61.5
	375	C+E	2.53	1.73	527	47.8
	250	C+E	3.8	2.55	525	27.8
900	375	C+E	2.27	1.60	527	55
1000	750	C+E	1.00	0.84	545	79.4
	375	C+E	2.00	1.57	528	60.9
	250	C+E	3.00	2.34	530	39.4
	187.5	C+E	4.00	2.99	522	34.4
	150	C+E	5.00	3.72	520	15.4
	75	C	10.00	-	-	-
1100	375	C+E	1.73	1.50	533	66.1
1200	375	C+E	1.47	1.46	528	70.9
1300	750	C+D	0.6	-	-	-
	375	C+D	1.2	-	-	-

Table 3.2: Summary of MD results for Model B as a function of the temperature of the substrate T_{sub} and the cooling rate α expressed in K/ns. The morphology is named 'C' for columnar grains, 'C+E' for columnar and equiaxed grains, 'C+D' for columnar and dentrites; t_1 is the time at which cooling ended, t_2 is the time at which the first nucleus appeared, ΔT is the degree of undercooling at which first nucleation appeared, ΔL_z is the width of the zone with equiaxed grains.

lidified and melted regions were affected by the progressive cooling. Two parameters define the thermal conditions: the temperature of the substrate, T_{sub}, and the cooling rate α measured in K/ns. All the conditions considered in the present work are reported in Table 3.2.

The temperature profile and the associated fraction of *fcc* atoms are depicted in Fig. 3.4 at different times for $T_{sub} = 1000$ K and $\alpha = 375$ K/ns. Time $t = 0$ ns corresponds to the time at which the heat source was released. We observed a solidified region ranging from 15 to 85 nm between the substrate and the solidification front. The solidification front separating the solid and liquid regions was located at 1650 K, close to the melting point. A temperature gradient of about 8.75 K/nm was established in this solid region, whereas most of the liquid region was at the melting temperature of Ni. Because of the imposed cooling, the liquid went from a superheated to a supercooled state. The temperature profile at 0.8 ns showed a peak reflecting the exothermicity of the solidification process, whereas most of the liquid region was at a temperature lower than the melting point of Ni. The solidification front was located precisely at the peak of the temperature front. From 0.8 ns to 1.6 ns, the solidification front propagated forward, resulting in columnar grain growth. At 1.6 ns, a small peak of *fcc* phase was observed in the liquid region, reflecting the appearance of a nucleus of crystalline phase. At 2 ns, the exothermic peak in the temperature profile was less pronounced because of the homogeneous nucleation and growth of the crystalline grains,

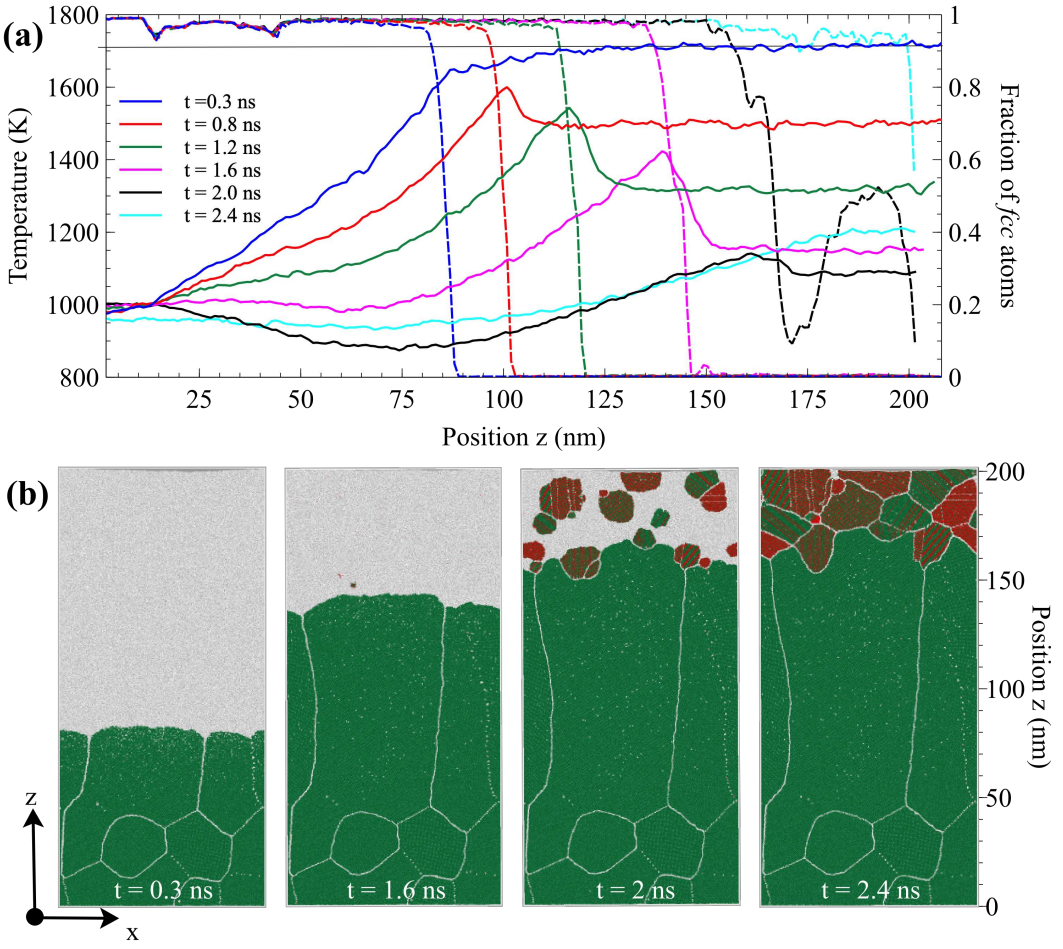

Figure 3.4: System (Model B) submitted to a cooling rate $\alpha = 375$ K/ns with a substrate maintained at $T_{sub} = 1000$ K. (a) Temperature profiles (solid lines, left axis) and fraction of *fcc* atoms (dashed lines, right axis) at different times during the global cooling. (b) Snapshots of the sytem at 0.3, 1.6, 2, and 2.4 ns. Color coding: *fcc* atoms are in green, *hcp* in red, and *unknown/liquid* atoms in light gray.

increasing the overall temperature in this previously liquid region. After 2.4 ns, the upper region was completely filled with randomly oriented and randomly distributed Ni grains. By comparison with model A, the cooling imposed in model B induced a drastic change in the microstructure, with the coexistence of columnar and equiaxed grains (see Fig. 3.4b).

In the case of a substrate at $T_{sub} = 1000$ K, the influence of the cooling rate α was evaluated to be in the range of one order of magnitude from 75 K/ns to 750 K/ns. We observed that the cooling rate modified the time at which the first nucleus appeared (t_2 in Table 3.2). The higher the cooling rate, the faster nucleation occurred. Consequently, the zone of equiaxed grains ΔL_z was thicker for greater cooling rates. The

position of the solidification front as a function of time is reported in Fig. 3.5. The typical curve is convex, in comparison with Model A (see Fig. 3.3). This means that the instantaneous velocity progressively increased with the degree of undercooling of the melt pool. Furthermore, greater cooling rates correspond to faster solidification. After first nucleus appearance (black diamond in Fig. 3.5), columnar grain solidification ceased in favor of equiaxed grains.

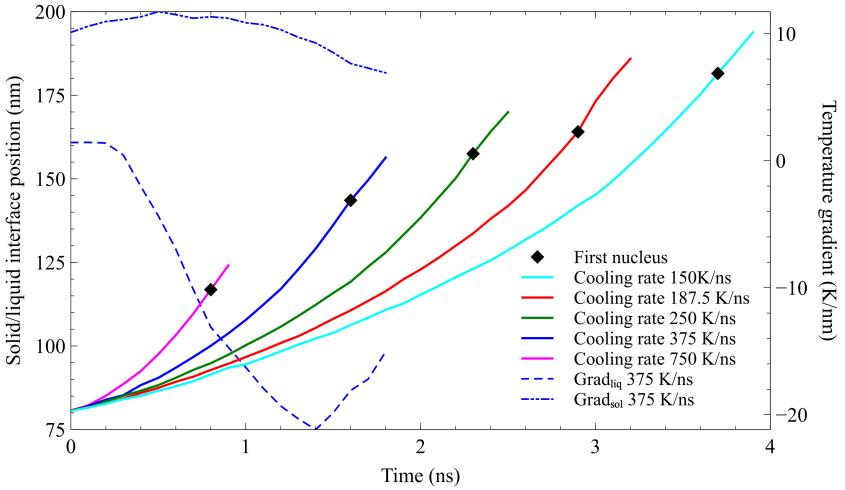

Figure 3.5: Position of the solid/liquid interface as a function of time for a substrate at 1000 K; different cooling rates are shown as solid lines (left axis). Local temperature gradients in the solid G_s and the liquid G_ℓ around the solidification front at a cooling rate of 375 K/ns are shown as dash-dotted and dashed lines in blue, respectively (right axis).

The only difference between model A and model B was the imposed cooling rate. In model A, the solidifiaction developped in a superheated fluid and the front kept its planar shape. In contrast, in model B, the solid grew in a supercooled liquid and the heat was conducted away from the front in the liquid due to the negative gradient $G_\ell < 0$, as shown in Fig. 3.5, in the case of a cooling equal to 375 K/ns. Equation (3.1) still holds and the velocity reads

$$v = \frac{\kappa}{L_V} \left[G_s + |G_\ell| \right] \tag{3.3}$$

The negative temperature gradient in the liquid G_ℓ significantly decreased until it reached a minimum when the first nucleus appeared. This observation explains why the instantaneous velocity increased during the associated solidification stage. After that stage, the heat released by the formation of solid grains in the liquid thwarted the cooling, which became less efficient. In Fig. 3.4 at t = 2 ns, we noted that the peak corresponding to solidification was less pronounced, when compared to previous times. Each grain formation released heat in the liquid region and, consequently, the melt pool temperature increased. Figure 3.6 shows the instantaneous solidification front ve-

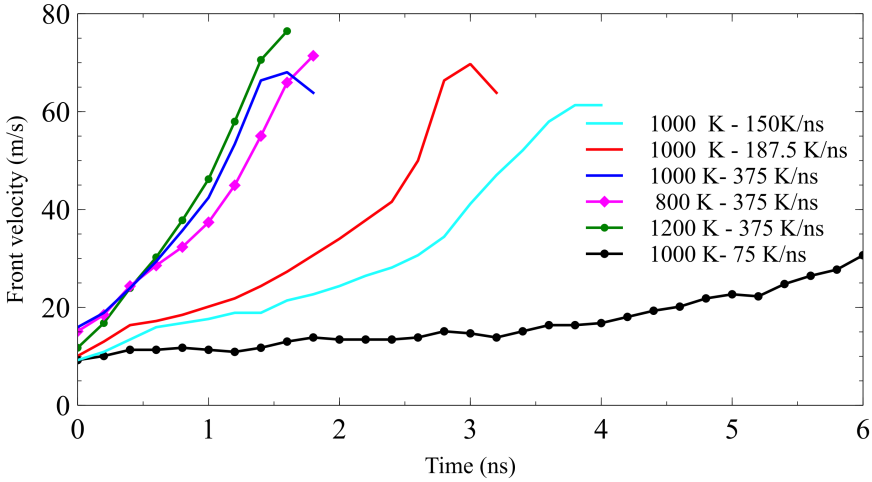

Figure 3.6: Instantaneous velocity as a function of time for different T_{sub} and different cooling rates α.

locity of columnar grains in representative cases of Table 3.2. For a given cooling rate ($\alpha = 375$ K/ns), the substrate temperature, T_{sub}, has a limited impact on front velocity. This is due to the fact that G_{s} in eq. (3.3) is the local temperature gradient evaluated on the left side of exothermic peaks (see Fig. 3.4a) rather than the global temperature gradient established in the solidified region. In the case of columnar and equiaxed grain microstructure, velocity increased as a function of time. This is related to the increase in magnitude of the temperature gradient in the liquid G_ℓ during cooling. The increase in v is thus more pronounced for greater cooling rates. Due to the formation of equiaxed grains in the melt, the front associated with columnar grains either stopped or slowed down before stopping. For a very low cooling rate (75 K/ns), the velocity was almost constant over 4 ns before a slight increase. The front reached the system edge before the degree of undercooling ($\Delta T = T_m - T = 450$ K) was sufficient for homogeneous nucleation.

The crystallization velocity is also a function of the degree of undercooling (see Section 2.4.2 for more details):

$$v = K \frac{T_m - T}{T} \exp\left(-\frac{Q}{k_{\text{B}} T}\right) \tag{3.4}$$

According to eq. (3.4), the velocity increases as a function of the degree of undercooling $T_m - T$. In contrast, the formation of equiaxed grains, which occurred at around the same degree of undercooling (500-600 K) for all systems (see Table 3.2), led to a drastic change in the local temperature gradient due to the release of heat associated with nucleation. The nucleation provoked a slowing down of the velocity at a characteristic time corresponding to the target degree of undercooling. As a consequence, the local temperature gradient in the liquid reached about the same minimum value (-20 K/nm) whatever the cooling rate or substrate temperature (see Fig. 3.5). The ve-

locity at columnar-to-equiaxed transition was in the range of 60-65 m/s, corresponding to this specific degree of undercooling.

During the propagation of solidification from 0 to 1.6 ns, the front progressively lost its planar shape, developing a characteristic rounded grain shape at the interface. This is also reflected by the greater thickness of the front. We observed a typical microstructure of columnar and equiaxed grains for most of the parameters considered, except for a high substrate temperature value (see Table 3.2). Homogeneous nucleation began when the degree of undercooling of the melt pool reached a value in the range 500 K-600 K, whatever the substrate temperature T_{sub} and the cooling rate α. Is it possible to interpret this observation in terms of Classical Nucleation Theory (CNT)? In CNT, the rate of homogeneous nucleation I reads [45]:

$$I = I_0 \exp\left(-\frac{A}{T^3(\Delta T)^2}\right) \tag{3.5}$$

with

$$A = \frac{16\pi\gamma_{\text{SL}}^3 T_m^4}{3k_{\text{B}}L_V^2} \tag{3.6}$$

where I_0 is a coefficient that depends on the interface temperature and free energy. The factor A is a constant that depends on the solid-liquid surface energy and latent heat of solidification. The normalized rate I/I_0 is plotted in Fig. 3.7(a) as a function of the degree of undercooling for the parameter values corresponding to the MD simulations (see Table 3.1). The nucleation rate strongly depends on the degree of undercooling. No nucleation was expected below $\Delta T = 500$K. The critical temperature T_{cr} corresponds to the maximum of the nucleation rate: $T_{cr} = 3T_m/5 = 1026$ K, i.e. $\Delta T = 684$ K. This estimate is in good agreement with the range of undercooling where nucleation was observed in MD simulations. The experimental estimate is that the critical nucleation temperature is between 0.5 and 0.6 times the melting temperature.

According to CNT, the critical radius r^* of a spherical nucleus depends on the degree of undercooling $\Delta T = T_m - T$:

$$r^* = \frac{2\gamma_{\text{sl}}}{L_v}\frac{T_m}{\Delta T} \tag{3.7}$$

The corresponding number of atoms in a critial nucleus is

$$N^* = 4 \times \frac{4\pi}{3} r^{*3}/a_0^3 \tag{3.8}$$

where the factor 4 stands for the number of *fcc* atoms/unit cell. In simulations, the degree of undercooling ΔT, at which nucleation appears, is in the range 500-600 K. The critial radius r^* is thus between 0.66 nm and 0.75 nm, corresponding to N^* between 100 and 160 atoms. The critical radius predicted by CNT with MD parameters is plotted in Fig. 3.7(b) for the degree of undercooling corresponding to the appearance of the

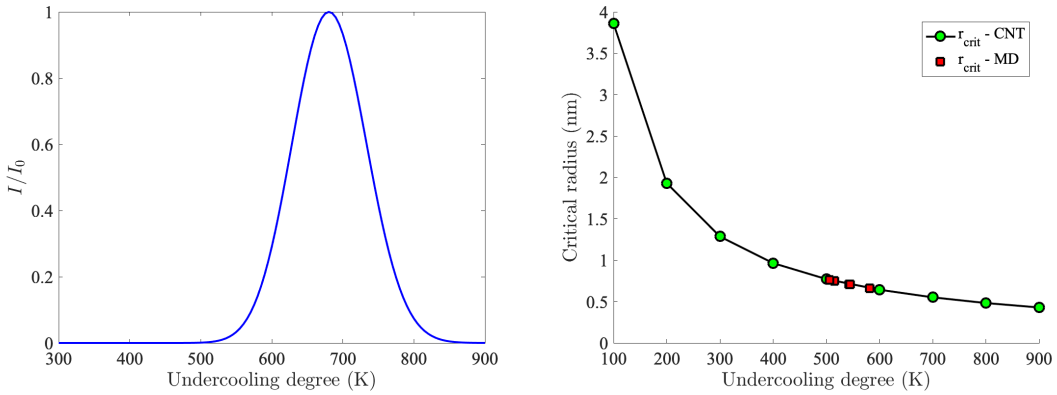

(a) (b)

Figure 3.7: Normalized nucleation rate I/I_0 (eq. (3.5)) (a) and critical radius (b) as a function the degree of undercooling.

first nucleus. We note that the critical nucleus is almost the same in all simulations and smaller than the size of the simulation box along the y axis, thus avoiding any simulation artifacts.

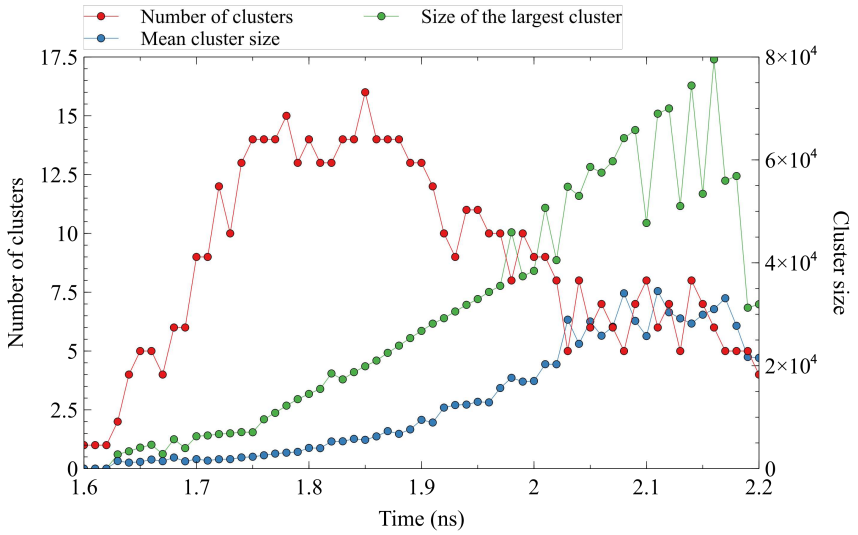

Figure 3.8: Cluster analysis: number of clusters, mean cluster size, and size of the largest cluster as a function of time. Size is measured in terms of the number of atoms in the cluster.

Nucleus formation dynamics is of primary importance in the final microstructure after solidification. In order to describe the dynamics, we analyzed the instantaneous system state at different times after the first nucleation during the growth process. Nuclei were identified by deleting all non-*fcc*/liquid atoms and then using the cluster analysis available in Ovito. A nucleus is defined here as a set of connected atoms, each of

which is within the reach of the other atoms in the same cluster. The cutoff distance was set at 2.5 Å, which is the distance between nearest neighbors in the *fcc* structure. The results are presented in Fig. 3.8. From 1.6 ns, the number of clusters increased, reaching its maximum at 1.8 ns. A maximum of fifteen clusters was observed. Note that the number of clusters does not correspond to the rate of nucleation (eq. (3.5)): it corresponds to the cumulative nucleation rate minus the clusters that disappeared due to coalescence. The mean cluster size remained lower than 5000 atoms. It corresponds to small clusters that are larger than the critical size. Note that the critical nucleus size decreases during system cooling, which ends at 2.5 ns (see eq. 3.7). We also followed the size of the largest cluster. At the very beginning, there is competition between clusters of similar size and the largest one may differ from time to time. At 1.75 ns, the largest cluster was clearly identified. It grew significantly because of adhesion of Ni atoms that diffused in the liquid and came into contact with existing clusters. After 1.8 ns, the number of clusters decreased following coalescence between isolated clusters or with columnar grains. Coalescence was associated with an increase in mean cluster size. Fluctuations in cluster numbers correspond to a detach/attach process between 2 or more adjacent grains. After 2 ns, the number of clusters decreased and their mean size stabilized. During the growth process of equiaxed grains, columnar grains extended in the direction of solidification ($z > 0$), but their growth progressively slowed due to the growth of equiaxed grains. Fluctuations in the size of the largest cluster reflect the attachment/detachment of the grain with columnar grains. At 2.3 ns, all grains were connected. At 2.5 ns, most of the system was solidified, with the coexistence of columnar and equiaxed grains. Grain boundaries were occupied by atoms with no well-defined structure (termed unknown atoms) and can be considered disordered grain boundaries.

Figure 3.4b shows that nuclei appeared randomly in the melt. In the front view provided by the snapshots, we first see the formation of round nuclei. These initial critical spherical nuclei ($r < 0.7$ nm) grew in the form of disks due to their extent being limited in the *y* direction. Each grain is made of *fcc* (green) and *hcp* (red) atoms. As the difference in cohesive energy per atom for *fcc* and *hcp* is very small (less than 0.03 eV; see Table 3.1), any thermal fluctuation may cause the formation of *hcp* Ni atoms, leading to the formation of nanotwinned grains.

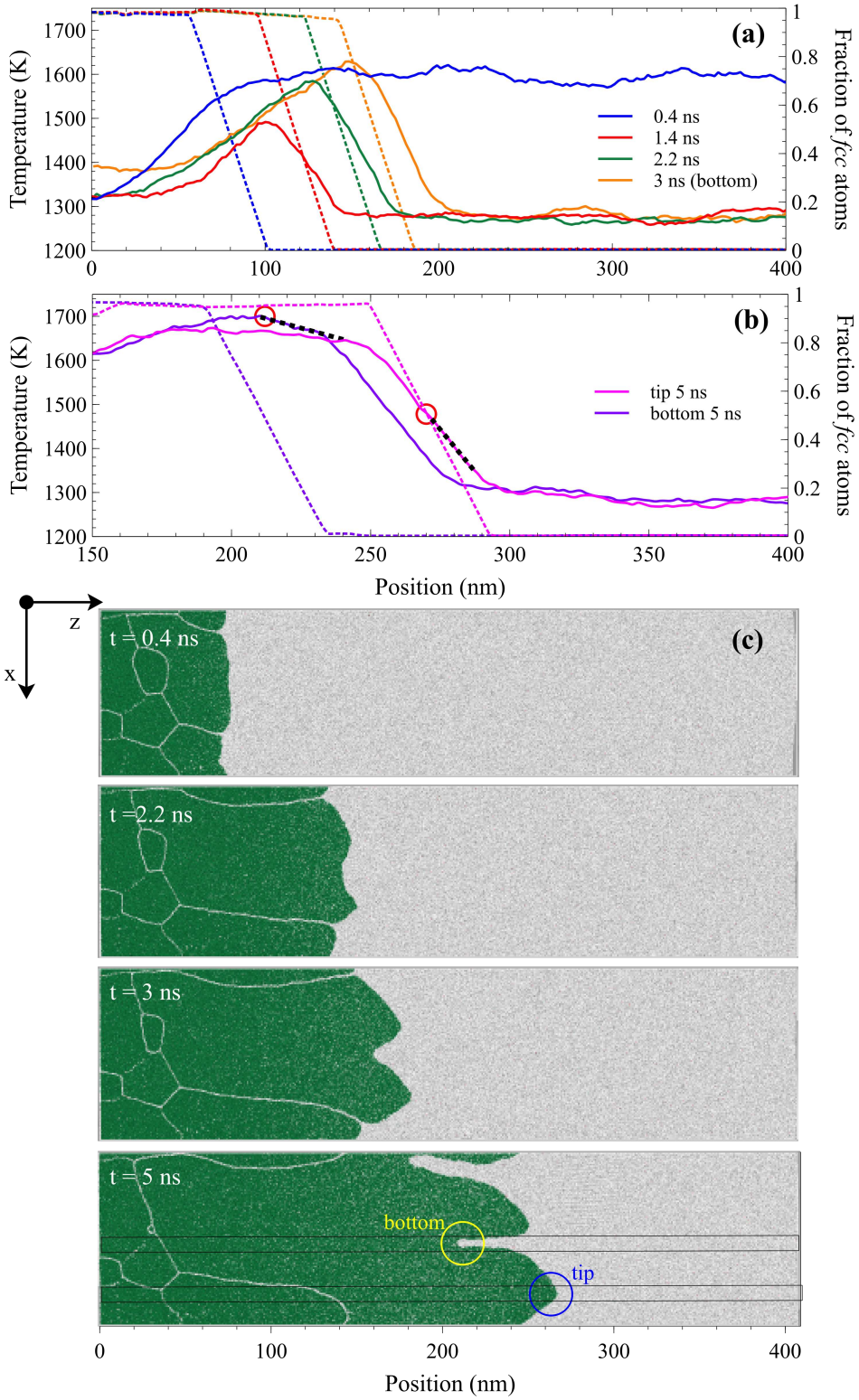

Figure 3.9: System (Model B) submitted to a cooling rate $\alpha = 375$ K/ns with a substrate maintained at $T_{\text{sub}} = 1300$ K. (a) Temperature profiles (solid lines, left axis) and fraction of *fcc* atoms (dashed lines, right axis) at different times during global cooling. (b) Enlarged view of temperature profiles (solid lines, left axis) and fraction of *fcc* atoms (dashed lines, right axis) restricted to the bottom and tip of the protrusion, at 5 ns. The slice over which spatial binning was calculated is shown in the snapshot (c) Snapshots of the system at 0.4, 2.2, 3, and 5 ns.

Let us now consider the case of a substrate at 1300 K (see Fig. 3.9). Here we considered a system twice as long in the z direction ($L_z = 426$ nm). At $t = 0$ ns, laser heating was removed, and the region ranging from 50 nm to 400 nm was submitted to a cooling rate of 375 K/ns. The temperature profile at $t = 0.4$ ns depicted in Fig. 3.9a corresponds to a liquid region at 1600 K and a solid region submitted to a temperature gradient. The limit between the solidified region and the liquid pool is delineated by the abrupt decrease in the fraction of *fcc* atoms. In about 1 ns, the melt pool cooled down to the substrate temperature $T_{\text{sub}} = 1300$ K. This corresponds to an undercooled melt pool. The degree of undercooling $\Delta T = 410$ K did not allow spontaneous nucleation (see Fig. 3.7a). The nucleation rate is almost zero, contrasting with the formation of nuclei observed for a substrate temperature at 1000 K. When cooling ended, the system evolved into adiabatic conditions (NVE ensemble). Figure 3.9a depicts the temperature profiles and fraction of *fcc* atoms at different times under these specific conditions. At 1.4 ns, the temperature peak due to the release of latent heat was evacuated into the solid and liquid parts. At 2.2 ns, this peak became higher, while the temperature gradient in the solidified region became smoother. For later times, this tendency became more pronounced, with a smooth gradient in the solid part and a sharp one in the liquid around the solidification front.

In solidification theory [151], it is well known that when a solid grows in an undercooled liquid, a planar solid/liquid interface is unstable. At 2.2 ns, we observed that protrusions located in the central columnar grain developed at the interface to form a cellular structure with fingers (snapshot in Fig. 3.9). At later times (for instance, 3 ns and 5 ns), these fingers extended, with a marked bottom and tip. In Fig. 3.9b, we plotted the temperature profiles and the fraction of *fcc* calculated in a slice containing the tip or the bottom of the finger. A striking fact is that the thickness of the solidification front between the tip and the bottom increased significantly between 3 and 5 ns. In Fig. 3.9b, we see that the heat released at the tip can only be conducted in the liquid (Fig. 3.9b - circle in red) when the local gradient is very steep. Local temperature $T_{\text{tip}} \sim 1450$ K is lower than the melting point. The heat released at the finger bottom is conducted in both solid and liquid parts. The local temperature $T_{\text{bottom}} \sim 1698$ K is close to the melting point, T_m (Fig. 3.9b - circle in red). The positions of the tip and the bottom are plotted as a function of time in Fig. 3.10(a). As expected, the velocity of the tip v_{tip} is greater than that of the bottom: v_{bottom}. The difference in position between the tip and the bottom increases as a function of time, indicating the progressive extent of the fingers observed in the snapshots. Heat is conducted away from the tip in the liquid, due to the local steep temperature gradient in the liquid part. Due to the Gibbs-Thomson effect [151], the solidification velocity at the tip reads

$$v_{\text{tip}} = \frac{\kappa_{\text{liq}}}{L_V}\frac{1}{r}\Delta T_0\left(1 - \frac{r^*}{r}\right) \tag{3.9}$$

where ΔT_0 is the degree of undercooling, r^* is the corresponding critical radius, and r is the characteristic size of the tip. Given the parameters (see Table 3.1), the theoretical value of the tip velocity is given in Fig. 3.10b. The measured value of the tip is close

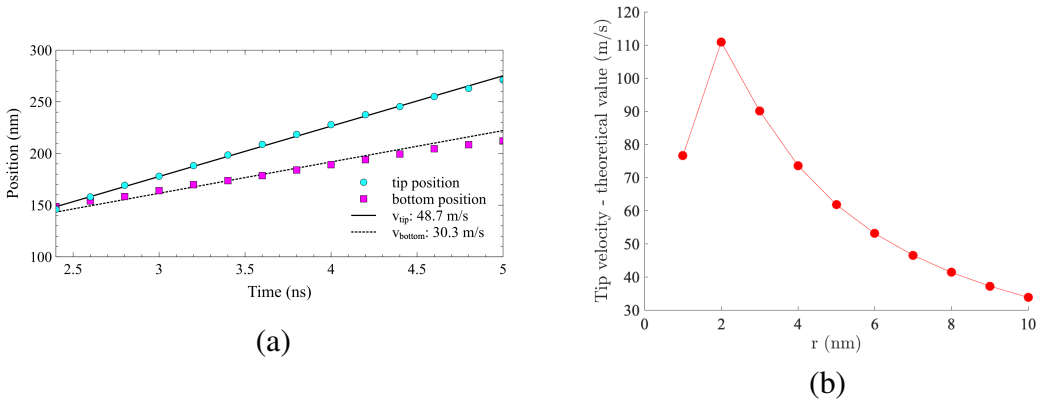

Figure 3.10: (a) Position of the finger tip and bottom as a function of time. (b) Theoretical estimate of tip velocity as a function of the characteristic size of the finger (see eq. 3.9).

to 50 m/s, corresponding to a characteristic size of 6 nm, in good agreement with our simulations.

As shown in Table 3.2, the microstructure observed after solidification depends on both substrate temperature, T_{sub}, and cooling rate, α. The value of T_{sub} modifies the steepness of the temperature gradient in the solid region between the substrate and the solidification front. This temperature gradient becomes smoother as the solid/liquid interface moves forward. In addition, since T_{sub} is the temperature of the melt pool after completion of cooling, its value gives the degree of undercooling. In the case of low values, $T_{sub} \leq 1200$ K, the final structure corresponds to the coexistence of columnar and equiaxed grains. For values $T_{sub} \geq 1300$ K, we observed columnar grains and the development of protrusions associated with solidification front instability. In this case, the degree of undercooling was never high enough for homogeneous nucleation, since the rate of homogeneous nucleation is almost zero.

3.4 Summary

Molecular dynamics (MD) simulations were used to provide in situ observations of solidification during additive manufacturing (AM). The thermal conditions to which the system is submitted during AM are dynamic. The temperature gradient between the solidified region and the melt pool is constantly evolving. Thus, conduction of heat away from the solid/liquid interface takes place in non-stationary conditions. In addition, thermal radiation and convective cooling of the melt pool induce a progressive cooling of the liquid region. Molecular dynamics simulations allow us to reproduce these conditions in a nano-box system corresponding to the close vicinity of the solidification front.

We first analyzed the case of directional solidification in a non-stationary temperature gradient. The steepness of the temperature gradient is directly related to the substrate

temperature T_{sub}. A low T_{sub} value increases the temperature gradient in the solid region (G_s), leading to rapid propagation of the solid/liquid interface in the direction of the gradient. The heat release by conduction in the solidified region determines the front characteristics (velocity and stability). The microstructure is a typical columnar structure. The solid/liquid interface remains flat, expect at grain boundaries, where grain boundary grooving was observed.

When the cooling of the melt pool is taken into account, the situation is completely different. Heat is conducted away from the interface in both solidified and melted regions, leading to an intrinsically unstable solid/liquid interface, with the development of rounded columnar grains. In addition, when the undercooling induced by the cooling was sufficient, we observed spontaneous nucleation of seeds in the melt pool and growth of equiaxed grains. These randomly oriented grains impede further propagation of columnar grains.

The faster the cooling, the faster the equiaxed grains appeared, leading to a large region with equiaxed grains. The propagation velocity of columnar grains is directly related to the temperature gradients from either side of the interface, in the solid (G_s) and liquid (G_l) regions. A greater cooling rate promotes the propagation of columnar grains by increasing their velocity. So the same operating parameter (cooling rate) influences the two competing solidification modes (directional solidification and homogeneous nucleation). The maximum degree of undercooling ΔT_{max} depends on the substrate temperature: $\Delta T_{\text{max}} = T_{\text{sub}} - T_m$. If ΔT_{max} is not in the appropriate range, the nucleation rate vanishes. In this case, the columnar grains continued to grow, but thermal instability led to grain fingering, very similar to dendrite formation.

Although the length scale is nanometric, molecular dynamics simulations reproduce the complex behavior associated with solidification during additive manufacturing. With complementary simulations, we were able to evaluate the structural and thermodynamic parameters of Ni associated with the EAM potential [112]: latent heat of fusion, solid/liquid interfacial energy, heat conductivity, etc. (See Section 2.4.2). This study allowed us to compare the behaviors at nanoscale to those expected in the framework of the classical solidification theory. The main conclusion is that predictions of the solidification theory of pure metals still hold at the nanoscale. Another interesting conclusion of the present work is the observation of CET in a pure metallic system. Here, the CET is driven exclusively by thermal conditions. The next step is to consider systems with inoculants in the melt pool, in order to further control the CET, as is usual in experiments. In addition, through the detailed characterization of relevant parameters, we could consider supplementing this study with simulations at mesoscopic scales [152, 153].

Chapter 4

Mechanical activation of metallic powders and reactivity of activated nanocomposites

We proposed a description, at the atomic level, of a mechanical treatment on a mixture composed of two metallic powders. We used Molecular Dynamics to simulate the very first impact of grinding balls involving compaction and plastic deformation. Two binary mixtures were considered: Ni-Al and Ti-Al, in order to assess the influence of the mechanical and structural properties of these pure elements on the characteristics of the activated mixture. We observed the formation of nanometric mixing zones over deformation steps. The effects induced by the mechanical treatment were found to be specific for each binary system, and depended on both the mechanical and structural properties of the pure elements. Mechanical activation induces solid-state solubility, structural transformations, and defects. In this chapter, we evaluated reactivity and transport properties at different temperatures in Ni-Al and Ti-Al nanocomposites fabricated by mechanical activation. We assessed the extent of their mixing zones, together with solubility, mobility, and the formation of intermetallics within these zones.

4.1 Details of the simulations

The equations of motion of the atoms were integrated with a timestep of 1 fs. As shown in Fig.4.1, we studied the mechanical deformation of a parallelepipedal simulation box filled with rounded particles[1]. The typical box size was 58.6 nm x 58.6 nm x 16.8 nm. To build this initial system, we randomly distributed 12 spheres of 16.6 nm diameter in the middle plane of the simulation box. Each sphere was filled with either a monocrystalline or polycrystalline metal. The polycrystalline systems were obtained by Voronoï tessellation [144, 147]. The EAM potentials developed for the Ni-Al and

[1]Here, "particle" means powder particle

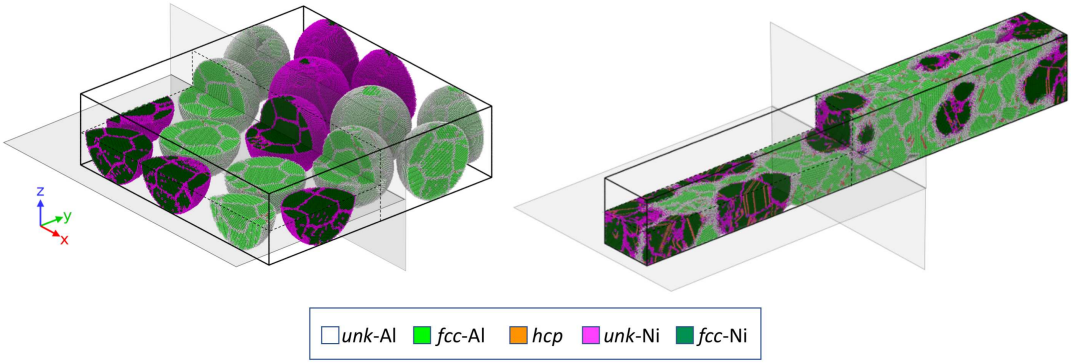

Figure 4.1: Simulated system. Initial state with *fcc*-Ni and *fcc*-Al polycrystalline particles (left). System elongated along the *y*-direction after deformation (right).

	structure	Exp. T_m (K)	Sim. T_m (K)	Exp. T_{tr} (K)	Sim. σ (GPa)	Exp. H (HV)
Al	fcc	933	1055 [112]		8.0 [112]	18
			870 [92]		6.6 [92]	
Ni	fcc	1728	1710 [112]		19.4 [112]	60
Ti	hcp $\rightarrow$ fcc	1713	1531 [92]	1155	14.8 [92]	99

Table 4.1: Structural, thermodynamics and mechanical properties: Structure of pure elements at ambient temperature; Melting temperature T_m of pure elements: Experimental value and theoretical value corresponding to the specific potential; Experimental value of the transition temperature T_{tr}; Simulated tensile strength, σ; Experimental value of hardness, H.

Ti-Al systems are designed by Purja Pun *et al.* [112] and Zope *et al.* [92]. The total number of atoms for the Ti-Al and Ni-Al polycristalline systems are 1658148 and 2110942, respectively. Moreover, the mole fraction (i.e. N(Ni)/N(Al) or N(Ti)/N(Al)) is 52 at.%. The properties of the elements are summarized in Table 4.1.

The system was first equilibrated at 300 K by a run of 50 ps in the NVT (canonical) ensemble followed by 50 ps in the NPT (isothermal-isobaric) ensemble. After this preliminary step, the atoms are integrated in the NPT ensemble. In order to mimic high-energy ball milling in which the average impact velocity of grinding balls is typically between 2 and 14 m/s, the box was shrunk at the constant velocity of 13.17 m/s, corresponding to a compression rate of $\dot{\varepsilon} = 4.5\,10^{10}$ s^{-1} along the x-direction [132]. The length of the simulation box was fixed along the z-direction, and adjusted along the y-direction by the Nose-Hoover barostat to maintain zero pressure in the system. The system deformation was monitored by computing the relative compression $\varepsilon_{xx} = |\Delta L/L_0| = |(L-L_0)/L_0|$. In the following, we will use ε instead of ε_{xx}, for simplicity. The system was deformed up to 80% of its initial length in 1.78 ns before studying its reactivity at a finite temperature. The reactivity simulations were carried out at constant temperature using the anisotropic NPT ensemble along all three directions.

The mechanical alloying observed during high-energy ball milling is necessarily related to the mechanical properties (e.g. Young's modulus, hardness, and tensile strength) of the elemental metal. Some of these properties can be evaluated by computing stress-strain curves. Nevertheless, hardness calculations will require nanoindentation simulations, which are complex and beyond the scope of this study. As a first approximation, stress-strain curves give a rough estimate of the hardness [80] in a given binary by using an empirical linear dependance, $H \approx 3\sigma$, reported between tensile strength and hardness [154] (see Table 4.1)

The local environment (i.e. *fcc*, *bcc*, or unknown/amorphous) was determined for each atom, with the adaptative Common Neighbor Analysis (a-CNA). In the initial configuration depicted in Fig. 4.1, each atom was tagged with an indicator referencing its type and local structure.

4.2 Effects of mechanical activation at the nanoscale

The system composed of nanometric particles of K and L (Ni-Al and Ti-Al) was subjected to compaction and plastic deformation mimicking the action of grinding balls during mechanical treatment. We focused on the 3D defects created by mechanical activation, in particular mixing zones (MZs) where the two elements are in direct contact (see Fig. 4.2) [80]. Mixing zones are of special interest because they could play the role of precursor in subsequent alloying processes. We observed that the effect of deformation depends both on mechanical properties and on the structural characteristics of K and L. The main characteristics of mixing zones after deformation are summarized as follows:

- In the Ni-Al system, both elements are *fcc* but Ni is harder than Al ($H_{\mathrm{Ni}} > H_{\mathrm{Al}}$). Mechanical treatment produces thick and amorphous MZs with an excess of Al. The other crystallized atoms adopt the *fcc*-Ni lattice. In this case, the ductile element adheres easily to hard particles, as in a wetting process. This is corroborated by the high mobility of Al atoms that already occurs during the compaction stage. After plastic deformation is completed, *hcp* planar defects (stacking faults) are created in Ni particles.

- In the Ti-Al system, there is a considerable difference in hardness ($H_{\mathrm{Ti}} \gg H_{\mathrm{Al}}$), as in the Ni-Al system, but the elements have a different crystallographic structure (*hcp-fcc*). The consequences of mechanical treatment are very different in comparison with the Ni-Al system. Mixing zones have a limited extent, with only half of the atoms being amorphous, and a moderate excess of Al. Atom mobility is limited, and occurs during the plastic deformation stage. Crystallized atoms in MZs are *fcc*-Al, *fcc*-Ti, *hcp*-Al, or *hcp*-Ti. In other words, Al(Ti) can adopt the original Ti(Al) structure. Aluminum atoms are stabilized when they are in close vicinity to Ti atoms. This feature leads to the creation of *fcc* seeds that could play the role of nucleus in the formation of an intermetallic.

After deformation, *fcc* stacking faults (2D) and *fcc* regions (3D) are created in Ti particles.

In the next section, the reactivity and transport properties at different temperatures in Ni–Al and Ti–Al nanocomposites fabricated by mechanical activation are evaluated. We assessed the extent of their mixing zones, together with solubility, mobility, and the formation of intermetallics within these zones

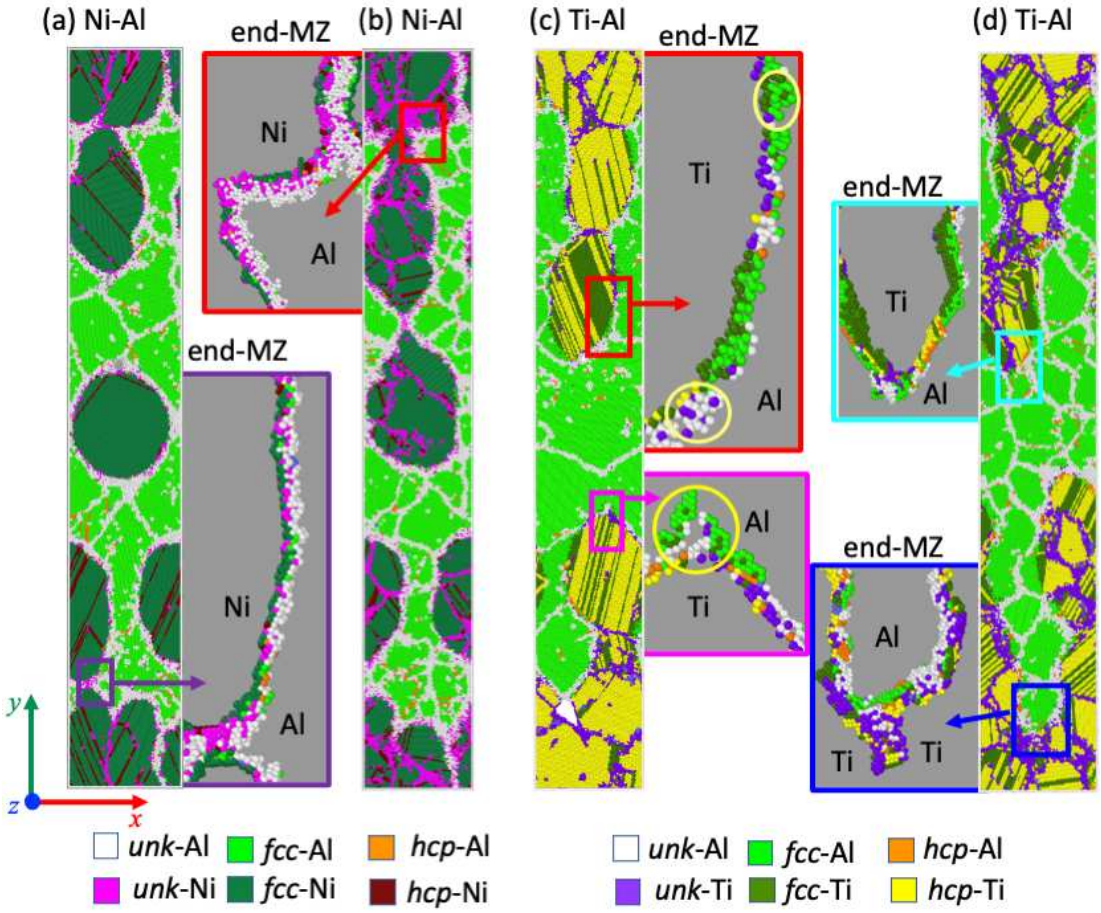

Figure 4.2: Snapshots of a slice of 10 Å, around z = 100 Å after deformation (ε = 73 %): (a) Ni-Al monocrystalline particles (b) Ni-Al polycrystalline particles (c) Ti-Al monocrystalline particles (d) Ti-Al polycrystalline particles.

4.3 Reactivity and mobility in activated powders

Two of the systems studied are reactive: Ti-Al and Ni-Al. Mechanical activation of elemental powders was found to increase their reactivity [49, 78]. This result could be attributed to the formation of premixed nanoclusters, nano-sized precursors and/or defects, including amorphous and metastable regions. In order to understand the role

of activation in reactivity, we studied the evolution of MZs in a temperature range close to ignition temperature, together with atom mobility in MZs, and reactive mechanisms as a function of microstructure.

4.3.1 Ti-Al system

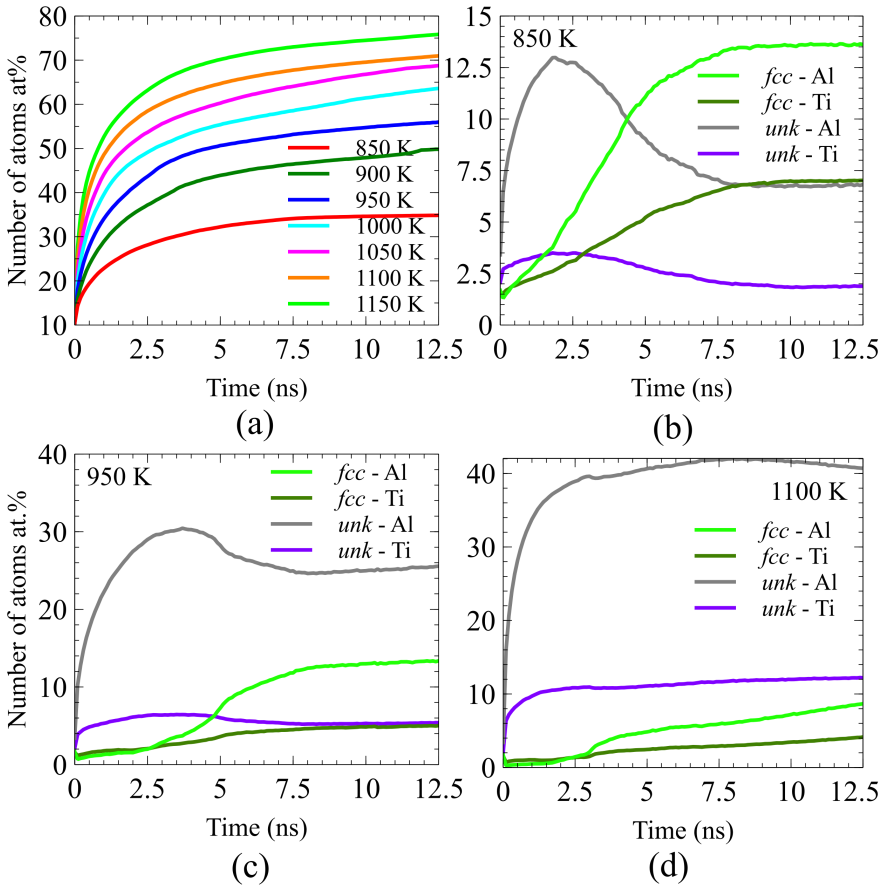

Figure 4.3: (a) Evolution of the number of atoms (at.%) in MZs as a function of time, for different temperatures. (b) Evolution of the number of *fcc*- and *unk*- atoms (at.%) in MZs at $T = 850$ K. (c) $T = 950$ K. (d) $T = 1100$ K. The atomic percentage of atoms is relative to the number of atoms in the entire system.

We first considered the Ti-Al activated system composed of polycrystalline particles after a deformation of $\varepsilon = 73\%$. The system evolution was investigated at temperatures ranging from 850 K to 1150 K, in 50 K steps. For this purpose, the system was heated up to the target temperature and simulations were carried out in the NPT ensemble. We focused on MZs because they reflect the reactivity between pure elements. The evolution of MZs as a function of time is represented in Fig.4.3a. The number of atoms in MZs is 10 at.% after deformation. At low T, in the range (850 K - 950 K), the number of atoms in MZs reached a plateau value in 5 ns. For larger T values, the

number of atoms in MZs continued to increase slowly over the time scale considered. Temperature was found to strongly influence the population in MZs. We must reach temperatures close to 1150 K for the whole system to be mixed. We next analyzed in detail the system at $T = 850$ K, 950 K, and 1100 K, on each side of the melting temperature of the less refractory element ($T_m(\mathrm{Al}) = 870$ K for the Ti-Al EAM potential [92]). What is the reason for the increase in MZs? We expected partial or complete amorphization of Al and diffusion of Ti in Al atoms, resulting in an increase in the number of dissimilar close neighbors.

At $T = 950$ K ($T_m(\mathrm{Al}) < T < T_m(\mathrm{Ti})$) and 10 ns, atoms in MZs represent more than half of the system (n_{MZ} = 55 at.%). Figure 4.3c shows the distribution of atoms according to their local configuration and type as a function of time. The number of *unk*-atoms sharply increased and reached a maximum at 4 ns with a majority of Al atoms. After that stage, MZ reorganization took place. Some amorphous atoms of Ti and Al progressively adopted an *fcc*-local configuration. The ratio between *fcc*-Ti and *fcc*-Al in MZ, $\xi_{fcc} = N_{fcc}(\mathrm{Ti})/(N_{fcc}(\mathrm{Ti}) + N_{fcc}(\mathrm{Al})) = 0.28$, is close to the typical value required for the formation of the TiAl3 intermetallic ($\xi_{fcc} = 0.25$). At 10 ns and later, a majority of atoms in MZs were amorphous (u_{MZ} = 65 at.%). We identified two transformations:

- melting of Al and partial dissolution of Ti in liquid
- formation of the intermetallic phase $TiAl_3$. Note that the $D0_{22}$ structure is based on a face-centered cubic structure.

$$Al_{\mathrm{sol}} + Ti_{\mathrm{sol}} \rightarrow Al_{\mathrm{liq}} + (Al + Ti)_{\mathrm{sol}} + TiAl_3 \tag{4.1}$$

A representative slice was chosen to analyze the local dynamics. Corresponding snapshots are given in Fig. 11. We identified the following characteristic behaviors at 950 K:

I After deformation, Ti particles are composed of *hcp*-Ti, *fcc*-Ti, and *unk*-Ti at internal grain boundaries (GB). Defects in *hcp*-Ti grains are *fcc*-Ti linear defects (stacking faults). Aluminum particles lost their spherical shape and are composed of *fcc*-Al and *unk*-Al in GBs. A few *hcp*-Al atoms correspond to defects in Al grains.

II As the system temperature was increased to 950 K, we observed the rapid amorphization of Al surrounding Ti particles (0.2 ns). Titanium atoms at the particle periphery started to dissolve. We noted that a small region of *fcc*-Ti promoted the formation of *fcc*-Al in its vicinity.

III From $t = 0.2$ ns to 5.25 ns, we observed a progressive coarsening of *hcp*-grains in Ti particles and disappearance of *fcc*-defects. Amorphous atoms in GBs either became *hcp*-atoms or dissolved in the surrounding liquid. After 5.25 ns, the transformation of *unk*-Al to *fcc*-Al accelerated in MZs.

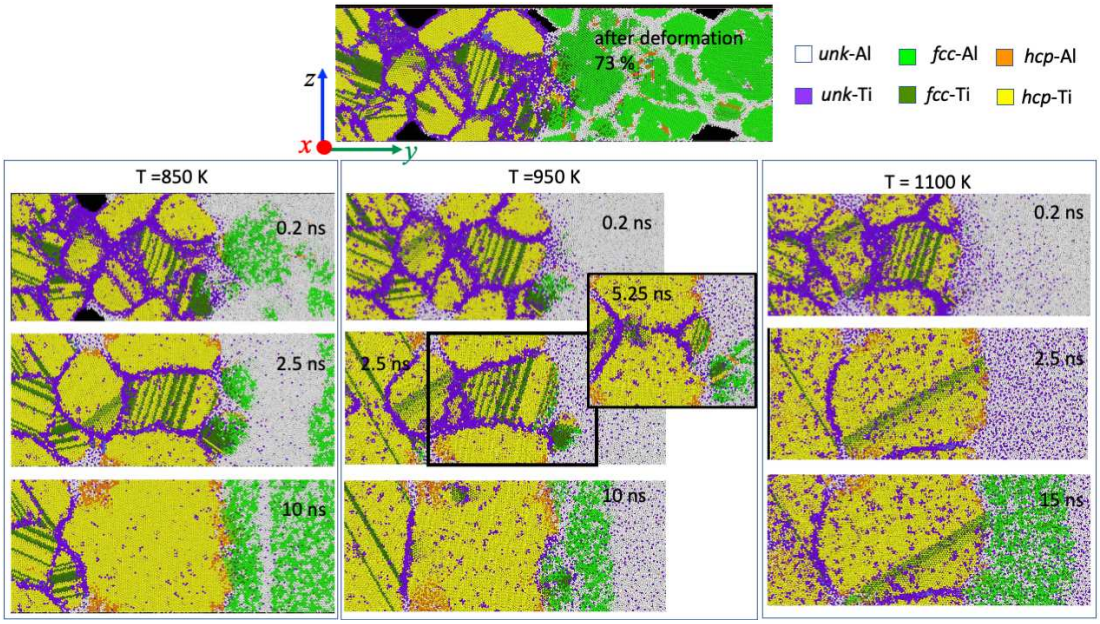

Figure 4.4: Snapshots of a slice of 40 nm in the y-direction and 10 nm in the x-direction: system after deformation, system at 850 K, 950 K, and 1100 K, at different times.

IV At the end, Ti particles were surrounded by a few *hcp*-Al, a layer of *fcc*-atoms, and a liquid solution of Ti and Al.

The final microstructure reflects the two processes described by (4.1).

We now analyze the behavior at 1100 K. In less than 2.5 ns, more than 50 at.% are in MZs (Fig.4.3a), with a majority of amorphous atoms (Fig.4.3d). The snapshots in Fig.4.4 (0.2 ns and 2.5 ns) depict the rapid dissolution of Ti in the liquid and the reorganization of the Ti particles, with larger grains and reduction of *fcc*-defects. From 2.5 ns, the number of atoms in MZs further increased, reaching 70 at.% at 12.5 ns (Fig.4.3a). In Fig.4.3d, we noted that the number of *fcc*-Al increased continuously from 2.5 ns to 12.5 ns, followed by a smooth increase in *fcc*-Ti atoms. The incoming atoms in MZs are *fcc*-atoms with a ratio $\xi_{fcc} \sim 0.33$ at 12.5 ns. A massive recrystallization of $TiAl_3$ around the Ti particle took place at 15 ns. At 1100 K, reactive dissolution and formation of the intermetallic $TiAl_3$ were both observed.

For the two temperatures above the melting point of Al, we observed the spontaneous formation of the intermetallic phase $TiAl_3$. The solubility of Ti in the solution, $x_{\mathrm{MZ}} = 0.22$ - 0.26, is independent of temperature. At 850 K, the situation is quite different. Because the temperature is below the melting point of Al, we did not expect a global amorphization of Al atoms. A limited number of atoms ($n_{\mathrm{MZ}} = 35$ at.%) were in MZs at 12.5 ns (Fig.4.3a). This result indicates limited reactivity at that temperature. As shown in Fig.4.3b, the number of *unk*-atoms increased, reaching a maximum at around 2 ns. The decrease in *unk*-atoms was followed by an increase in *fcc*-atoms; the

ratio is 0.22 in amorphous phase and 0.35 in *fcc*-phase. The microstructures depicted in Fig.4.4 show a transient amorphization of Al atoms around Ti particles. At 2.5 ns, Ti atoms were either dissolved in *unk*-Al or substituted in the *fcc*-Al phase. At 10 ns, the Ti particle mainly recovered its *hcp*-structure, with a thin layer of *hcp*-Al at the periphery. Aluminum *hcp*-atoms correspond to atoms that occupy vacancies liberated by outgoing Ti atoms. Dissolution operates as an exchange of Ti and Al atoms at interfaces. At the end, the particle was surrounded by an *fcc* solid solution, an amorphous solution, and *fcc*-Al with defects.

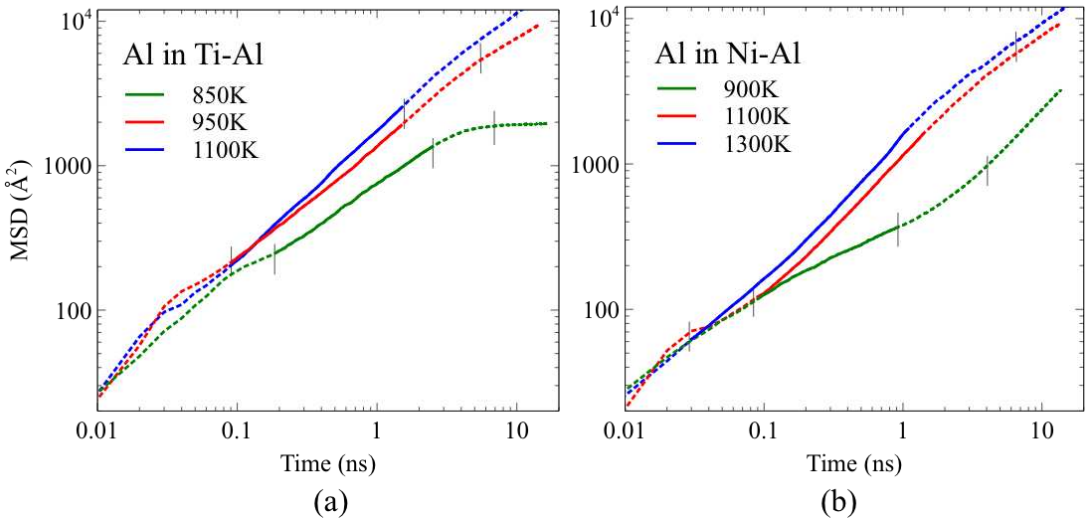

Figure 4.5: MSD log-log plot for Al inside the MZs in the Ti-Al system (a) and in the Ni-Al system (b) at representative temperatures. Log-log plots for Ti in the Ti-Al system and Ni in the Ni-Al system are given in Supporting Information. Vertical lines delineate the 3 stages observed in the system evolution (see text). Solid line corresponds to the time interval over which diffusion coefficients are computed (see Table 4.2).

In order to study the mobility of atoms in MZs, we computed the mean square displacement (MSD) of atoms in MZs as a function of time:

$$\mathrm{MSD} = \frac{1}{N_{\mathrm{MZ}}} \sum_{i=1}^{N_{\mathrm{MZ}}} |\vec{r}_i(t) - \vec{r}_i(0)|^2 \tag{4.2}$$

where N_{MZ} is the number of particles in the MZ, $\vec{r}_i(0)$ is the reference position of the i-atom, $\vec{r}_i(t)$ is the atom position at time t. Note that the number of particles in MZs increases as a function of time. The MSD log-log plot at different temperatures is depicted in Fig. 4.5a. Typically, a diffusion mode corresponds to a linear dependance: $\mathrm{MSD} \sim t$. Three characteristic slopes are observed in the MSD log-log plot that delineate three stages in the system evolution (the very beginning up to 0.1 ns corresponds to the suppression of voids between particles):

T (K)	700	800	850	900	950	1000	1050	1100	1150	1200
Al/Ti-Al			0.78	**1.35**	**1.97**	**2.07**	**2.46**	**2.71**	**3.02**	
Ti/Ti-Al			0.42	**0.72**	**1.21**	**1.37**	**1.80**	**2.19**	**2.61**	
Al/Ni-Al	0.016	0.057		0.38		1.16		**1.90**		**2.26**
Ni/Ni-Al	0.015	0.061		0.45		1.36		**2.29**		**3.05**

Table 4.2: Diffusion coefficients $\times 10^{-9}$ (m^2/s) in MZs for the Ti-Al system and the Ni-Al system. Values corresponding to temperatures above the melting point of Al are in bold.

	Al in Ti-Al	Ti in Ti-Al	Al in Ni-Al	Ni in Ni-Al
Q low T	69.84	69.45	100.54	103.95
Q high T	20.32	36.08	18.86	31.76

Table 4.3: Diffusion activation energy (kJ/mol) for the Ti-Al system and the Ni-Al system (eq. (4.3))

I First stage ($\sim$ 0.1 ns - $\sim$ 2 ns): The MSD log-log plot is fitted by a straight line, characteristic of a diffusion regime in MZs composed of *unk*-atoms.

II Second stage (2 ns - 8 ns): There is a change of slope and curve bending. This reflects lower atom mobility associated with partial recrystallization in MZs.

III Third stage (after 8 ns): There is another change of slope corresponding to a further slowing down of mobility.

Atom mobility can be directly related to the microstructure evolution of MZs depicted in Fig. 4.3b-d. The first stage corresponds to the increase in *unk*-atoms in MZs. In the second stage, the number of *unk*-atoms decreases in favor of *fcc*-atoms. In the third stage, the microstructure of MZs does not evolve significantly.

The diffusion coefficients are estimated for the time interval [0.1 ns - 3 ns] prior to recrystallization in MZs (Table 4.2). Figure 4.6 gives $\ln(D)$ for Ti and Al in MZs as a function of $1/T$. We noted two slopes associated either with high temperatures (950 K - 1150 K) or with low temperatures (850 K - 900 K). The linear fit gives the corresponding activation energies Q according to the Arrhenius law:

$$D = D_0 \exp\left(-\frac{Q}{RT}\right) \tag{4.3}$$

where D_0 is the prefactor and R the universal gas constant. The activation energies are given in Table 4.3. Below the melting point of Al (850 K), the diffusion coefficient is noticeably lower than at higher temperatures. The existence of two slopes observed in Fig. 4.6 reflects the change of microstructure in the MZs, with a transition from an amorphous system to pure liquid.

For purposes of comparison, the diffusion coefficients were evaluated with Dictra (Thermo-Calc). The diffusion activation energy in pure liquid Al is 19 kJ/mol, close

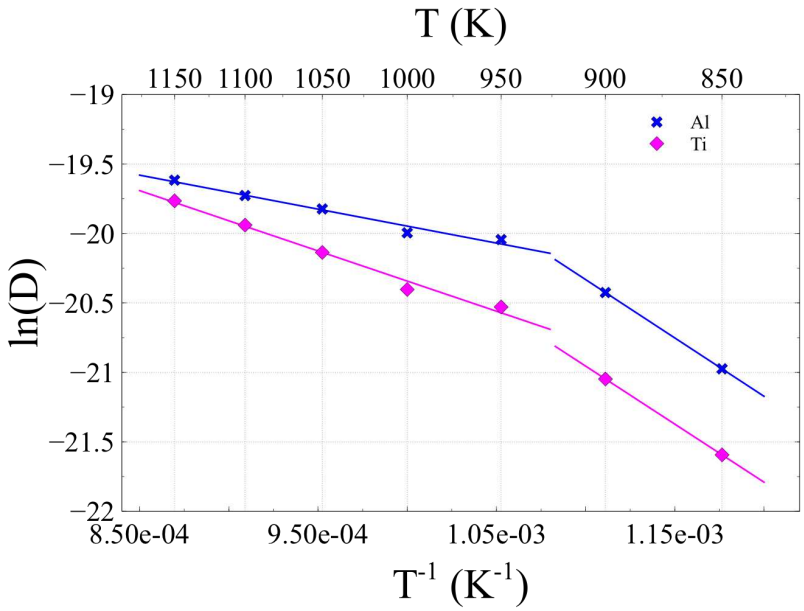

Figure 4.6: Plot of $\ln(D)$ as a function of $1/T$ for the Ti-Al system.

to the value measured in MD simulations. The diffusion coefficient of Ti in liquid Al at 1100 K, with mole fraction $x(Ti) = 0.2$, is 3.4 10^{-9} m^2/s, of the same order of magnitude as the value measured in MD simulations at high temperatures. Note, however, than this molar fraction is unrealistic in a system at equilibrium, due to the limited solubility of Ti in Al liquid.

In an activated system, Ti solubility in Al is greater than at equilibrium, which actually enhances reactivity. Figure 4.7 depicts the location of Ti atoms that will later be embedded in MZs. We identified Ti atoms in MZs at 2 ns (snapshot not shown), and reported their positions in black on a snapshot at 0.06 ns. Two locations were identified: internal grain boundaries and the external shell of the particle. Around the Ti particle, we observed a dissolution front in the liquid. Inside the Ti particle, GBs expanded with incoming Al and became channels for effective diffusion of Ti atoms toward the liquid solution. The GB expansion weakened particle stability so that it fragmented into small Ti-grains, which are more likely to dissolve. Both mechanisms promote the dissolution of Ti beyond the expected equilibrium value.

4.3.2 Ni-Al system

We next considered the Ni-Al activated system composed of polycrystalline particles after a deformation of $\varepsilon = 73\%$. Mechanical treatment induces the formation of amorphous regions where atoms of Ni and Al are mixed, occupying 15 at.% of the entire system. Mixing zones generally contain the same amount of Ni and Al. In order to

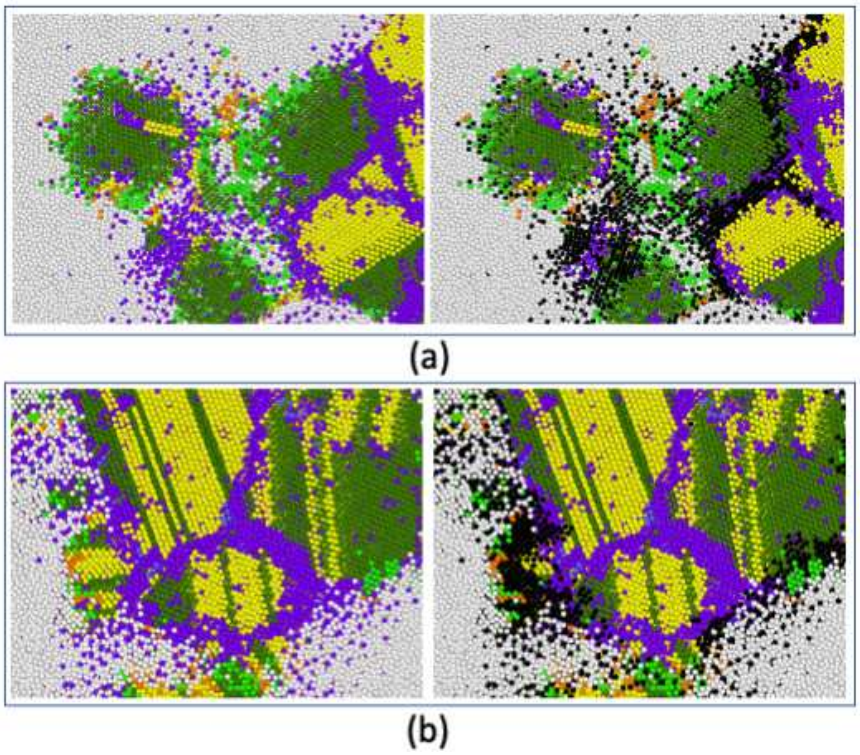

Figure 4.7: Two detailed views of the snapshot after deformation (0.06 ns). Black atoms are Ti atoms in MZs at 2 ns. (a) Visualization of Ti atoms in grain boundaries (b) Visualization of Ti atoms in the external shell. Left: All atoms are represented with the color coding of Fig. 4.4. Right: Ti atoms in MZs at 2 ns are shown in black.

investigate the reactivity of the activated system, the system evolution was studied at temperatures ranging from 700 K to 1200 K, in 100 K steps. For this purpose, the system was heated up to the target temperature, and simulations were carried out in the NPT ensemble. The extent of MZs as a function of time is represented in Fig. 4.8a. The mole fraction $x_{\mathrm{MZ}} = N_{\mathrm{MZ}}(Ni)/N_{\mathrm{MZ}}$ expressed in at.% is given in Fig. 4.8b. The behavior depends on temperature:

- At low temperatures (700 K and 800 K), the number of atoms in MZs (n_{MZ}) remained limited and did not exceed 22 at.% at 700 K and 30 at.% at 800 K. The proportion of Ni in MZs measured by x_{MZ} decreased as a function of time (Fig. 4.9b). This result indicates that more and more Al atoms are in MZs. If we compare the snapshot of the system prior to and after heating at 700 K (Fig. 4.9a and Fig. 4.9b), we note a coarsening of Al grains and the creation of amorphous regions around Ni grains with the mixing of Ni and Al atoms. As shown in Fig. 4.8c, MZs contained twice as much *unk*-Al as *unk*-Ni atoms.

- At an intermediate temperature (900 K, below the melting point of aluminum $T_m(\mathrm{Al}) = 1055$ K for the Ni-Al EAM potential [112]), the number of atoms in

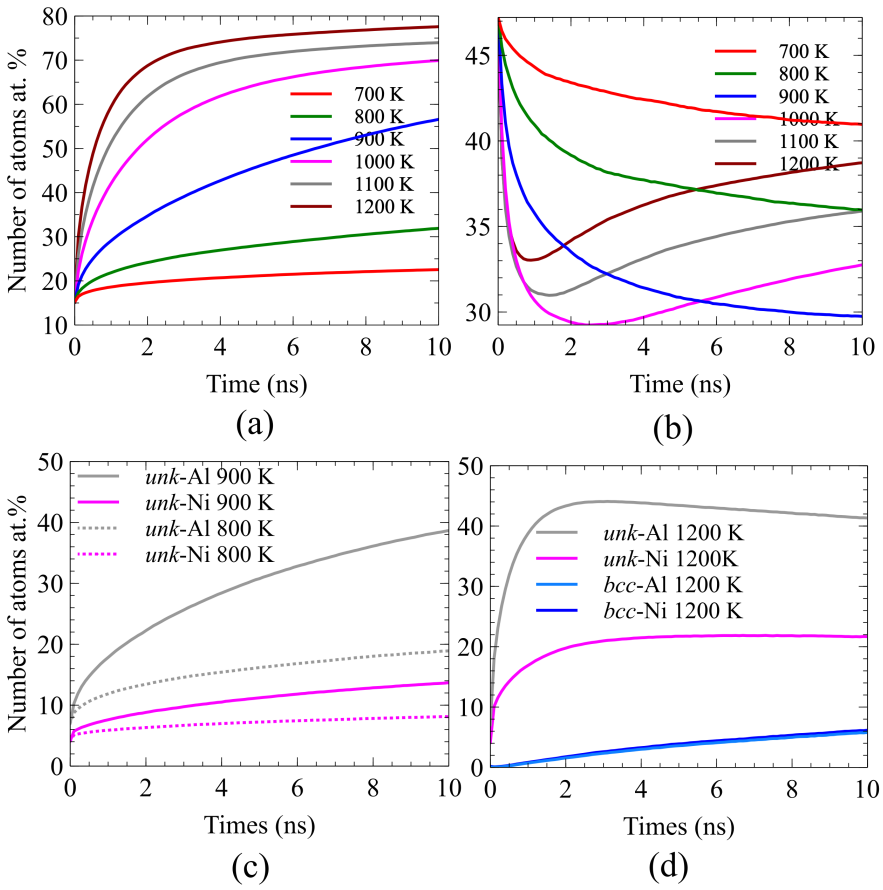

Figure 4.8: (a) Evolution of the number of atoms (at.%) in MZs as a function of time, for different temperatures. (b) Evolution of mole fraction x_{MZ} (at.%) in MZs (c) Evolution of the number of *unk*-atoms (at.%) in MZs at $T = 800$ K and $T = 900$ K. (d) Evolution of the number of *bcc*- and *unk*-atoms (at.%) in MZs at $T = 1200$ K. The atomic percentage of atoms is relative to the number of atoms to the entire system.

MZs (n_{MZ}) grew continuously up to 56 at.% at 10 ns because of the strong amorphization of Al atoms and subsequent dissolution of Ni in these amorphous regions. At 10 ns and beyond, the mole fraction x_{MZ} is stable and equal to 30 at.% . Mixing zones almost completely replaced Al regions (Fig. 4.9c). Locally, seeds of *bcc*-atoms nucleated around Ni particles.

- The behavior of the number of atoms in MZs is more or less the same at high temperatures (1000 K, 1100 K, and 1200 K). The number of atoms in MZs (n_{MZ}) increased before reaching a plateau value. At 1200 K, almost 80 at.% of atoms are in MZs. As shown in Fig. 4.8b, the mole fraction x_{MZ} decreased abruptly before reaching a minimum. First, Al melted and then Ni atoms progressively dissolved in the liquid solution. Figure 4.8d shows the increase in the number of *unk*-Al followed by the increase in *unk*-Ni in less than 2 ns. After 2 ns, the num-

ber of *bcc*-Al and *bcc*-Ni started to increase with the formation of intermetallic *B2*-NiAl. The number of *unk*-Al decreased slightly, while the number of *unk*-Ni remained constant. This result indicates that *unk*-Al atoms in MZs transformed into *bcc*-Al, and that *unk*-Ni atoms that became *bcc*-Ni were replaced in MZs by incoming Ni atoms that dissolved in the liquid region. At 10 ns, the snapshot (Fig. 4.9d) depicts shrinking *fcc*-Ni particles surrounded by a liquid solution composed of Ni and Al. Disoriented *B2*-NiAl grains surrounded the Ni particles and eventually formed a neck between particles. Grain boundaries progressively disappeared inside the Ni particles. We suppose that internal GBs acted as channels for outgoing *unk*-Ni that were dissolved in the melt. The mole fraction of *unk*-Ni in MZs is 0.34 at 10 ns, close to the expected equilibrium value.

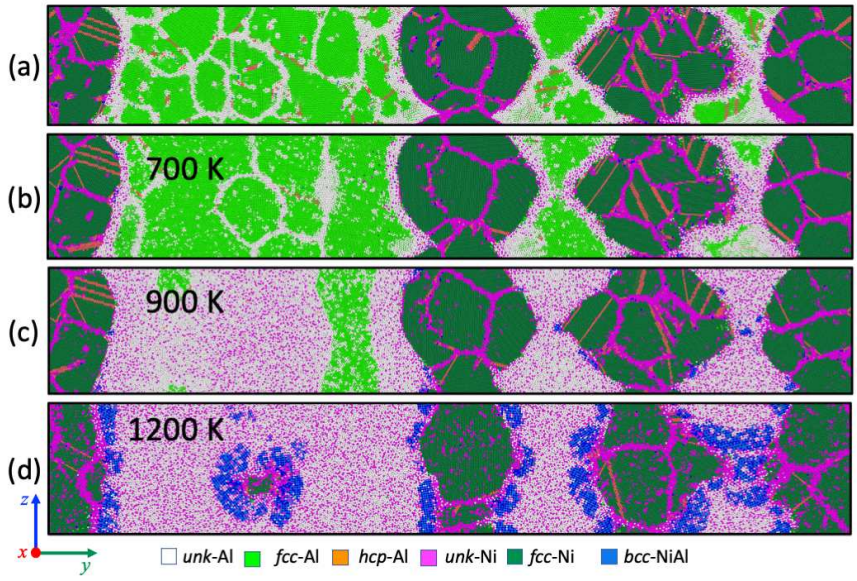

Figure 4.9: Snapshots of the system (slice at x = 169 nm) after deformation (a), at 700 K (b), 900 K (c), and 1200 K (d) at $t = 10$ ns.

The mobility of atoms in MZs was studied for the temperature range (700 K-1200 K). The MSD log-log plot is presented in Fig. 4.5b. At high temperatures (1100 K and 1300 K), we noted a diffusive regime followed by a slowing down of mobility, directly associated with the formation of the solid *B2*-NiAl intermetallic. By contrast, at 900 K, the diffusive regime was followed by an increase in atom mobility. This behavior is actually associated with the polycrystallinity of Al particles: Al GBs played the role of diffusion paths and thus enhanced atom mobility.

Diffusion coefficients were evaluated in the time interval [0.1 ns - 1 ns] prior to recrystallization. Results are summarized in Table 4.2, Table 4.3, and Fig. 4.9. At high temperatures, above the melting point of Al, the activation energy is close to 19 kJ/mol for pure Al liquid, the value given by Dictra (Thermo-calc) ($D = 6.95\,10^{-9}$ m^2/s at 1100 K). In the case of a liquid solution Ni + Al at 1100 K, the diffusion coefficient

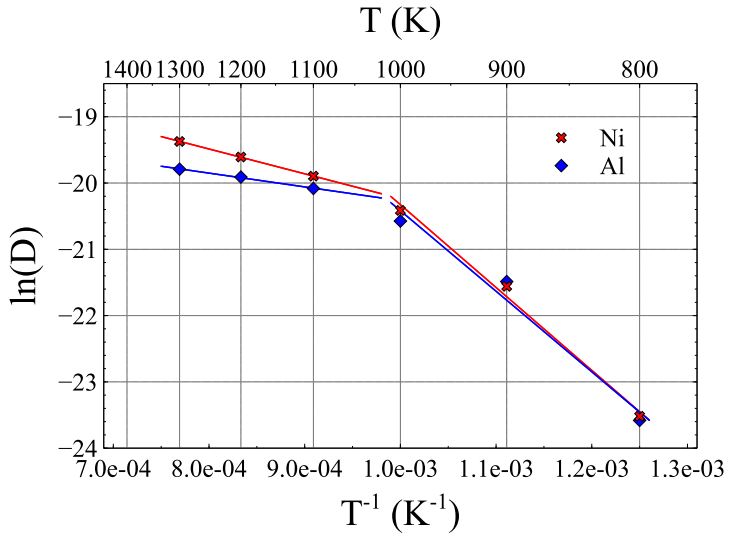

Figure 4.10: Plot of $\ln(D)$ as a function of $1/T$ for the Ni-Al system.

of Ni in the solution given by Dictra ranges from $1\,10^{-8}$ m^2/s to $2\,10^{-8}$ m^2/s, with the mole fraction x(Ni) in the range [0 - 0.3]. In the MD simulations, the estimated diffusion coefficient is smaller by one order of magnitude. Note that the melting temperature given by the Purja and Mishin potential is 1050 K, which is 170 K higher than the experimental value. This temperature difference will necessarily produce discrepancies when computing diffusivities close to the expected melting point. In addition, the discrepancy could be attributed either to the amorphous state of MZs, which occurs prior to complete melting in the time range over which the diffusion coefficient was estimated, or to the progressive dissolution of Ni into the liquid solution. At low temperatures, the diffusion coefficient measured in MZs is of the order of 10^{-11}-10^{-10} m^2/s, larger than the characteristic value in the *fcc* solid phase 10^{-15}-10^{-13} m^2/s. This higher diffusivity results from the almost completely amorphous atomic arrangement of the Ni-Al MZs.

We observed three different behaviors as a function of temperature:

- At high temperatures (1000 K - 1200 K), aluminum was completely melted. Large MZs with liquid solution $(\text{Ni+Al})_{\text{liq}}$ were formed. Note that, at 1000 K, the system behaved as if it were above the melting point of Al. The nanometric size of MZs induces their melting.

- At low temperatures (700 K - 800 K), atoms diffused in the amorphous regions formed around Ni particles. In this case, MZs can be considered as an amorphous solid solution $(\text{Ni+Al})_{\text{sol}}$. Nevertheless, diffusion coefficients are larger than values characteristic of a solid but of the typical order of magnitude of diffusion in GBs.

- At 900 K, below the melting point of aluminum, we noted an intermediate situation: extended amorphous regions in which Ni atoms diffuse more efficiently than at 800 K but less than in a liquid phase.

It appears that mechanical activation induced increased reactivity below the melting point of aluminum.

4.4 Summary

The mechanical treatment produces Ti-Al and Ni-Al nanocomposites whose reactivity has been investigated in the present work. For this purpose, we focused on the evolution of mixing zones at different temperatures, just below and above the melting point $T_m(Al)$ of the less refractory element (here Al). We also quantified the mobility in MZs by measuring the diffusion coefficients. The typical behavior can be summarized as follows:

- For the Ti-Al system, MZs increase during annealing. Annealing leads to the coarsening of Ti grains inside Ti particles, with suppression of defects and grain boundaries. For $T < T_m(Al)$, the reactivity is limited, with partial amorphization of Al, formation of *fcc* solid solution, and dissolution of Ti in amorphous Al. The diffusion coefficient prior to massive recrystallization corresponds to typical mobility in a dual-phase system: here, an amorphous phase. For $T \geq T_m(Al)$, the system is more reactive, with complete melting of Al, dissolution of Ti into the liquid solution, and formation of the intermetallic $TiAl_3$. The diffusion coefficient prior to crystallization corresponds to a melt. The mechanical treatment promotes the solubility of Ti in Al in comparison with equilibrium.

- For the Ni-Al system, annealing promotes broad MZs. The reactive behavior is directly related to the temperature. For $T < T_m(Al)$, the reactivity is limited. Mixing zones remain narrow, with the dissolution of Ni in the amorphous solid solution. The diffusion coefficient in MZs is of the same order of magnitude as diffusion in grain boundaries. For $T \sim T_m(Al)$, the reactivity is more pronounced, with broader MZs composed of *unk*-Al and *unk*-Ni. The diffusion coefficient in MZs remains smaller than in a liquid. For $T > T_m(Al)$, the activated system becomes very reactive, with the full amorphization of Al. Mixing zones extend over Al regions with effective dissolution of Ni into the liquid solution. The intermetallic *B2*-NiAl is formed around the solid Ni particles. The diffusion coefficient in MZs becomes close to that of a liquid.

Microscopic simulations provide an interesting tool to observe the effects of a mechanical treatment, and to study the reactivity of nanocomposites fabricated by a mechanical process. This work could be extended in order to take into account the activation associated with the friction of sliding interfaces. It would be interesting to estimate the efficiency of amorphization and chemical mixing, in the case where heat dissipation is taken into account. Another important issue is to understand the fragmentation

process during HEBM. Alternative approach such as Extended Finite Element method [155] could be undertaken to handle fracture and crack propagation at the mesoscopic scale.

Chapter 5

Reactivity of Ti–Al reactive laminated particles: Experimental study and molecular dynamics simulations

In this chapter, we focused on the reactivity of the Ti-Al system in the case of reactive laminated particles (RLPs) produced by high energy ball milling (HEBM), by combining an experimental investigation and MD study. In the experimental part that was performed by our collaborators, the aim is to detect the key aspects of the exothermic reaction as the reaction onset temperature and the characteristic activation energy. In the MD part developed during my PhD, the understanding of the reaction mechanism is directly related to the question of phase transformations associated with the self-propagating reactive wave. To handle this problem by means of molecular dynamics, the atomic and microstructure evolution inside the stacked layers was simulated at a fixed temperature. Two representative systems were prepared: a small system (reference system) and a thick system. Different initial temperatures close to the melting temperature of Al were imposed for the same stoichiometry $N_{\mathrm{Ti}}/N_{\mathrm{Al}} \sim 3$ with an excess of Ti. This allowed accurate description of reactive dissolution and crystallization of intermetallic compound during the progress of the reaction.

5.1 Experimental study

Composite Ti/Al powders were produced by means of HEBM technique in the planetary mill "Activator-2S" ("Activator", available at ISMAN laboratory inRussia), from the mixture of Ti and Al elemental powders. The powders were placed in the steel jars together with steel balls. Volume of the jar was 250 ml (filled with Ar at 4 bar), diameter of the steel balls 6 mm, balls to mixture mass ratio 20:1, the rotation speed of Sun-disc 200 rpm, milling time 120 min. After HEBM, the powder consisted of bimetallic particles, where Ti flattened inclusions were embedded into Al matrix: thus,

Al layers separated Ti islands in each bimetallic particle. Reactivity of the composite powders were evaluated by heating up mini-pellets (3 mm in diameter, 0.3 - 1.0 mm thick), consolidated from the composite powder, in Ar atmosphere, and measuring reaction onset temperature T_i. Details of the methods were published earlier [52]. Microstructure and elements distribution inside the bimetal particles were studied using SEM and EDS analyses. Basing on the Kissinger method [156], energy of activation E was evaluated from the formula

$$\ln\left(\frac{b}{T_i^2}\right) = \text{const} - E/(RT_i) \tag{5.1}$$

where $b = dT/dt$ - heating rate, T_i - reaction onset temperature, R - gas constant. We used T_i instead of the temperature corresponding to maximum reaction rate, T_m, because, as distinct from differential scanning calorimetry, temperature in our experiments increased very sharply after reaction initiation. Thus, value of T_i was close to T_m, which allowed evaluation of E from eq. (5.1).

After HEBM, both metals (Ti and Al) formed bimetal particles (Fig. 5.1a). More ductile metal Al forms matrix, where Ti layers (inclusions) have irregular shape. No intermetallic phases were observed at the boundaries between Al and Ti (Fig. 5.1b). At the same time, some intermixing of these two metals was revealed due to line-scan mode of EDS microanalysis (Fig. 5.2). A typical microstructure of the intermixed areas looks similar to metastable phases that formed in the Ni-Al systems during HEBM due to intense friction [64]. It allows us to assume that metastable phases (perhaps, solid solutions) can be formed due to HEBM also in the Ti-Al system, which should decrease temperature of the reaction initiation in this system.

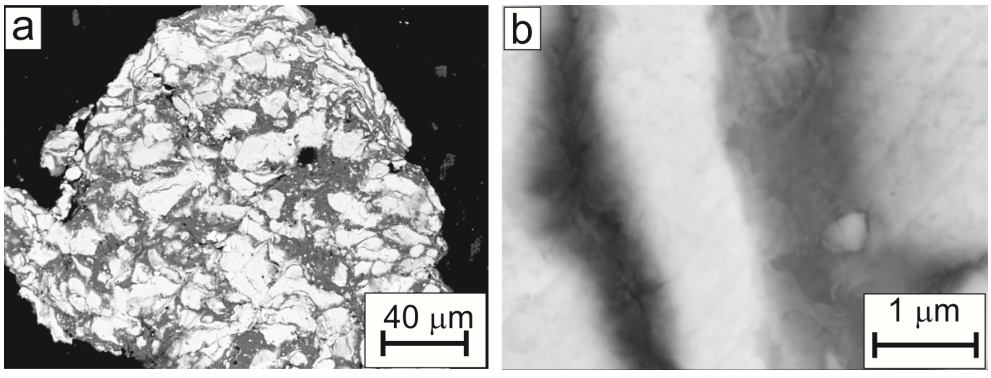

Figure 5.1: Microstructure of the bimetal particle after HEBM (a) and boundaries between Ti and Al layers (b). SEM, backscattered electrons. Dark phase is Al, white - Ti.

In order to measure the reaction initiation temperature, the mini-pellets were placed in the h-BN crucible and heated up using carbon-strip heater with average rate from 18 K/s up to 119 K/s. Typical temperature-time profile of the process is shown in Fig. 5.3. When the temperature of the sample achieved some value T_i, exothermal

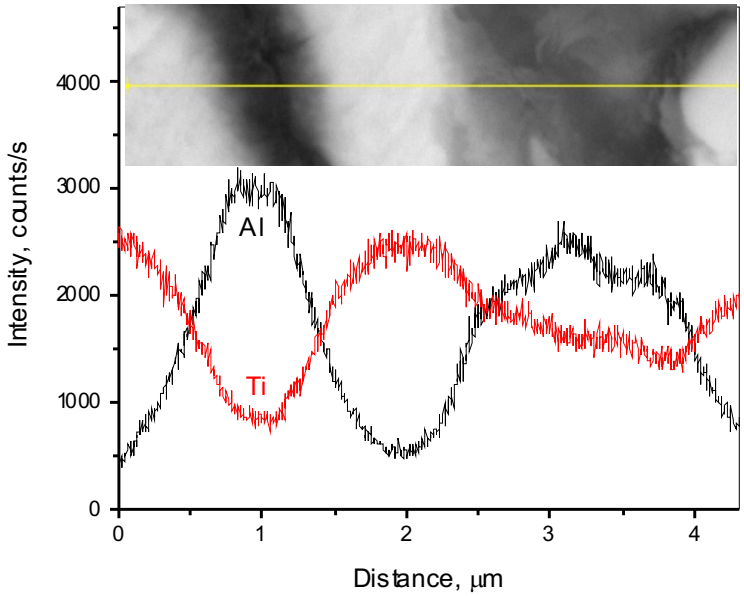

Figure 5.2: SEM and results of the EDS scanning along the line. Dark phase - Al, white - Ti, grey - intermediate metastable phase.

reaction started and increased temperature sharply. The heating regime below T_i does not follow strictly a linear law, however, average heating rate can be calculated for the sake of rough approximation as

$$b = < dT/dt > = (T_i - T_0)/t_i, \tag{5.2}$$

where T_i - the reaction onset temperature, T_0 - initial temperature of the sample, and t_i - heating time. The carbon heater was switched-off in 1 second after exothermic reaction initiation, and the sample cooled down.

The value of T_i increased continuously with increasing heating rate b (Fig. 5.4). Based on these data, the Kissinger equation (5.1) was applied to evaluate activation energy of the process:

$$E \sim -R \frac{d\left[\ln(b/T_i^2)\right]}{d(1/T_i)} \tag{5.3}$$

Two linear regions were appeared at the Kissinger plot (Fig. 5.5) that correspond to the values of activation energy $E_1 = (28.4 \pm 7.3)$ kJ/mol for higher temperature, and $E_2 = (92.1 \pm 14.4)$ kJ/mol for lower temperature regions. A transition point between these two regions corresponds to a temperature of about 950 - 960 K, which is close to the melting point of Al (933.5 K). Thus, we can assume that limiting stage of the process changes, when T_i exceeds melting temperature of Al. Probably, under slow heating conditions (smaller b), reaction has enough time to form some solid intermetallic product on the boundary between Ti and Al, which later limits the reaction rate even after Al melts. At fast heating (larger b), no solid product appears, and the reaction is limited only by diffusion in the melt, with small energy of activation.

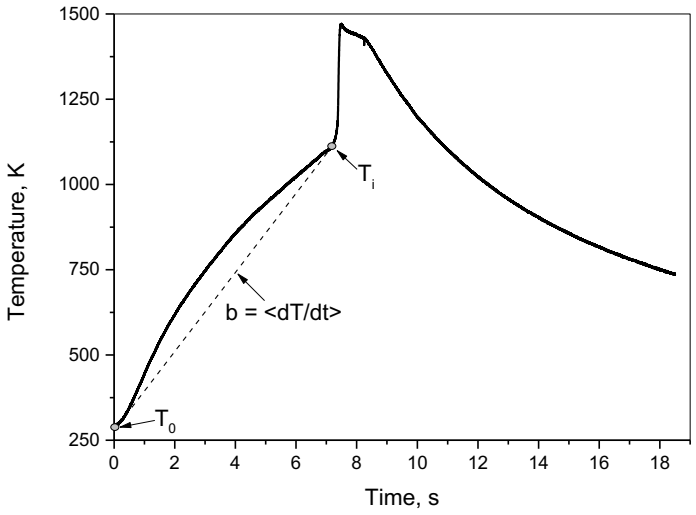

Figure 5.3: Temperature-time profile of the heating up and reaction in Ti/Al composite powder sample measured with WRe5/WRe20 thermocouple.

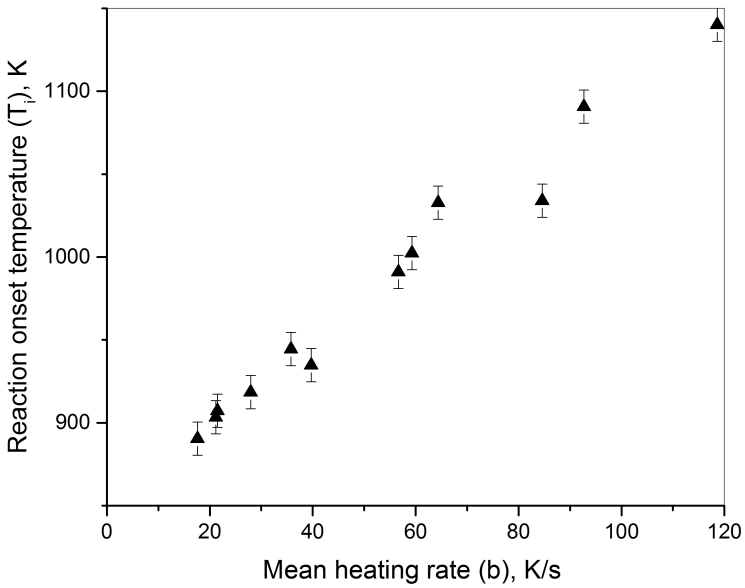

Figure 5.4: Reaction onset temperature as function of heating rate.

Although the two measured values of E definitely indicate two different mechanisms of interaction, it remains a challenge to reveal these mechanisms. Diffusion coefficient and activation energy of Ti atoms in the Al melt are not available up to now. The activation energies of Ti and Al solid state diffusion in different phases of the Ti-Al systems, such as α-Ti, β-Ti, Ti_3Al, and TiAl, fall in the range 2.59-4.08 eV (250-394 kJ/mol) [157]. These values are much higher than the values measured in this work. From

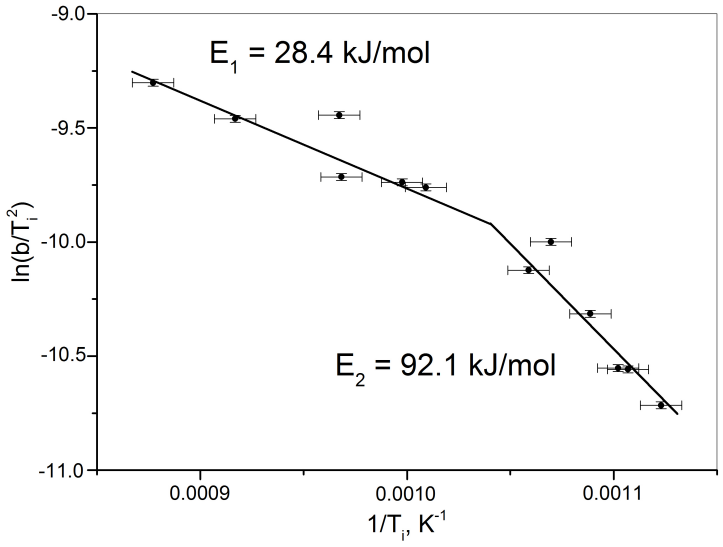

Figure 5.5: Evaluation of activation energy in Kissinger coordinates.

the other hand, some experimental study of interfacial reactions in Ti/Al multilayers during diffusion welding, shown that effective activation energy of diffusion decreases dramatically with decreasing atomic fraction of Ti [158]. Thus, the activation energy for diffusion in the TiAl phase was determined as 250 kJ/mol, while diffusion in the $TiAl_3$ phase had activation energy about 100 kJ/mol. Moreover, $TiAl_3$ was a major phase formed during the diffusion welding [158]. Recent works confirmed the leading role of $TiAl_3$ in the interface reaction between Ti and Al below melting point of Al [159, 160]. Measurements of the linear growth rate of $TiAl_3$ layer in the temperature range 823 - 923 K gave activation energy 128.7 kJ/mol [160]. Since the forming has polycrystalline structure with well-developed grain boundaries network [159], the grain boundary diffusion must be also taken into account. Basing on to the normal parabolic growth of the $TiAl_3$ layer (which was the only phase appeared on the Ti/Al boundary at 823-923 K), activation energy of 33.1 kJ/mol was obtained for the low temperature grain boundary diffusion controlled growth, and 296.2 kJ/mol - for the high temperature bulk diffusion controlled growth [161]. Overall activation energy of 76.8 kJ/mol was accepted for the whole region of the applied annealing temperatures. It is worth noting that all these data were obtained using isothermal annealing method. Comparison with our data measured at non-isothermal conditions allows assumptions that the value of 92.1 kJ/mol corresponds to combination of solid-state bulk and grain boundary diffusion, while 28.4 kJ/mol may correspond to grain diffusion solely or to liquid phase diffusion in the Al melt. From analogy with other metallic melts, we may expect that activation energy of diffusion in the Al melt is approximately 5 times smaller that that for the solid-state diffusion [162]. The following MDS results allow deeper insight in the mechanism of interaction.

5.2 Numerical study

5.2.1 Design of the numerical experiments

The system was analyzed at the atomistic level using the EAM interatomic potential developed by Zope and Mishin in 2003 [92]. The potential of Zope and Mishin was initially fitted for Al, α-Ti and γ-TiAl using extended experimental and ab-initio databases and its transferability was then tested by considering other intermetallic compounds (i.e., $L1_0$-TiAl, $L1_2$-$TiAl_3$ and $D0_{22}$-$TiAl_3$). A preliminary step consisted in computing the melting temperature (see 5.1) using a classical liquid-solid coexistence (two-phase) method [114]. Thermal expansion coefficient was also determined to characterize the behavior of the system as a function of temperature (see Section 2.4.2).

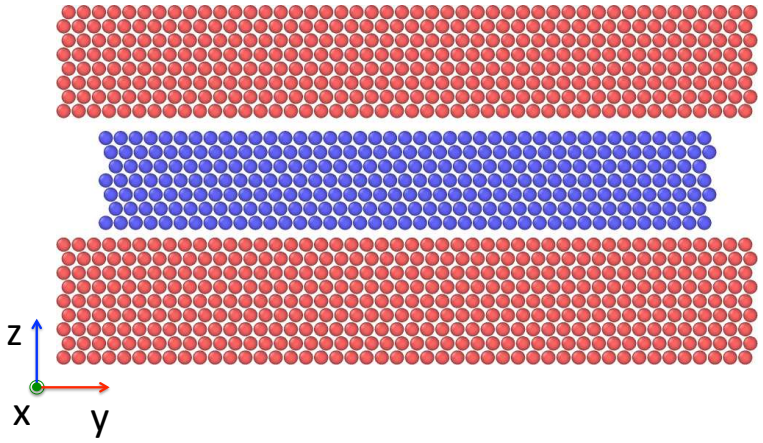

Figure 5.6: Initial configuration of the simulated system with one slice of Al in between two Ti layers. Al and Ti are shown as blue and red spheres, respectively.

In order to model the Ti-Al reactive interfaces in RLPs, a simplified bilayer Ti-Al-Ti system was considered. The initial system (see Fig. 5.6), referred to here as the small sample, is made of an inner layer of *fcc*-Al (7 atomic planes containing 10 188 Al atoms) in between two outer layers of hcp-Ti (8 and 9 atomic planes each containing all together 31 280 atoms) with $N_{\mathrm{Ti}}/N_{\mathrm{Al}} \sim 3$. The size of the simulation box is $L_x = L_y = 11.8$ nm in the x-direction and L_z = 6 nm in the z-direction. The interface is oriented normal to the [002] direction of the Ti layers and to the [111] direction of Al layer. Periodic boundary conditions are applied in all directions. The empty space around the Al layer allows the system to avoid any artificial constraint due to the application of periodicity on the Al and Ti [163].

Both Al and Ti lattice parameters were determined as a function of temperature on bulk systems. Hence, the Ti-Al-Ti system was created with the appropriate lattice parameter corresponding to the initial temperature. The simulation is thermalized in the canonical statistical ensemble (NVT) over 400 ps at the initial temperature using

	Melting temperatures (K)			Cohesive energies (eV/atom)
metal/phase	two-phase method	other works	experimental	EAM potential vs. experimental
Al	870	870	933	3.36 / 3.36
Ti	1531	-	1941	4.85 / 4.85
	1510	1494	1713	4.51 / 4.51
($D0_{22}$)	1175	-	1388	4.02 / 4.06

Table 5.1: Melting temperatures and cohesive energies evaluated using the Zope and Mishin EAM potential [92] and experimental values.

	$N_{\mathrm{Ti}}/N_{\mathrm{Al}} \sim 3$			
sample	$L_x = L_y$ (nm)	L_z (nm)	Al atomic planes	# atoms
Reference system	11.8	6.1	7	41 468
Thick sample	17.5	13.4	15	211 710

Table 5.2: Summary of the simulation details

a Nosé-Hoover thermostat (damping parameter of 0.1). The simulation is then carried out in the microcanonical statistical ensemble (NVE) over more than 15 ns. NVE simulation corresponds to adiabatic conditions: no external reservoir is interacting with the system. This procedure allows us to observe the spontaneous dynamics of the system that may imply a variety of elemental mechanisms. The time step to integrate the equation of motions with a Verlet algorithm was fixed at 0.001 ps.

A thick sample was also considered (see Table 5.2). Initially, an inner layer of *fcc*-Al with of 15 atomic planes (N_{Al} = 51 230) was placed in between two outer layers of *hcp*-Ti with 40 atomic planes each (N_{Ti} = 160 480) with $N_{\mathrm{Ti}}/N_{\mathrm{Al}} \sim 3$. The size of the simulation box is $L_x = L_y = 17.5$ nm in the x-direction and $L_z = 13.4$ nm in the z-direction. The orientations of Ti and Al at interface was (002)/(111) as in the previous simulations. The simulation procedure is in two parts:

- The system is thermalized in the NVT ensemble before the simulation in adiabatic conditions (NVE ensemble).
- The system is then cooled down by step of 5 K in the NPT ensemble during 300 ps and the NVT ensemble during 100 ps. After each step, the simulation is carrying out in the microcanonical ensemble (NVE) in order to observe the spontaneous dynamics of the system. The cooling process begins at 1315 K and ends at 1200 K.

Different indicators are used to follow the evolution of the system. The number density profiles along the $z-$axis gives a good indication of the crystallinity state and of the local composition in Ti or Al in each slice. Well-defined peaks are associated with a system structured in atomic planes. Each atom was labeled by two indices: one associated with the chemical species (type) and one with its local lattice structure (Ackland and Jone's indicator, see Section 2.4.1). It is also useful to compute the potential energy per atom, which is very sensitive to the local environment of a given

atom. Global indicators were also followed during the evolution of the system: temperature and the stoichiometry in the inner layer. The stoichiometry is defined as the ratio $\xi = N_{\mathrm{Ti}}/(N_{\mathrm{Ti}} + N_{\mathrm{Al}})$.

5.2.2 Reference sample results

The reference system was prepared at different initial temperatures, close to the melting temperature of Al, T_m(Al) = 870 K (see Table 5.1). For initial temperatures below the melting temperature of Al, the system remains stable. Just a small number of defects appear in the inner layer. The stability of the interface is quite unexpected as compared to prior works on Ni-Al system where exothermic phase transformations already appear in solid-state [163]. This is probably due to the very low misfit between (002) Ti-plane and (111) Al-plane (see Fig. 5.7).

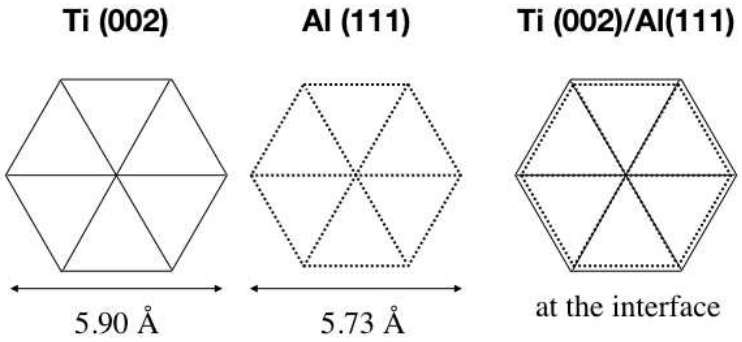

Figure 5.7: Atomic arrangement of Ti and Al at the interface.

For an initial temperature of 950 K, the situation is completely different. During the thermalization at 950 K, the Al inner melts and wets the Ti-free surface. During the simulation in adiabatic conditions, the temperature is followed as well as the fraction (at%) of atoms in the different local configurations (*fcc, hcp* or unknown). The typical shape of curves in Fig. 5.8 suggests that the dynamics of the system can be divided into 4 stages:

I Just after thermalization, from t = 0.4 to 11 ns (stage I), the number of amorphous atoms (unknown) and *fcc* atoms is more or less constant. Amorphous atoms correspond to liquid atoms. The fcc-atoms are located at free surfaces or interfaces. The temperature slowly increases up to 1050 K and ξ reaches 0.18.

II During stage II (from t = 11 to 12 ns), the number of *hcp*-atoms starts to decrease. The temperature reaches 1100 K and ξ exceeds 0.2. This stage corresponds to a rapid dissolution of Ti in the inner layer.

III The stage III is short (less than 0.2 ns, from t = 12.24 to 12.46 ns). More *hcp*-Ti atoms disappear together with a sudden and short decrease in amorphous atoms. This corresponds to a reorganisation of the inner layer in *fcc* atoms. The burst

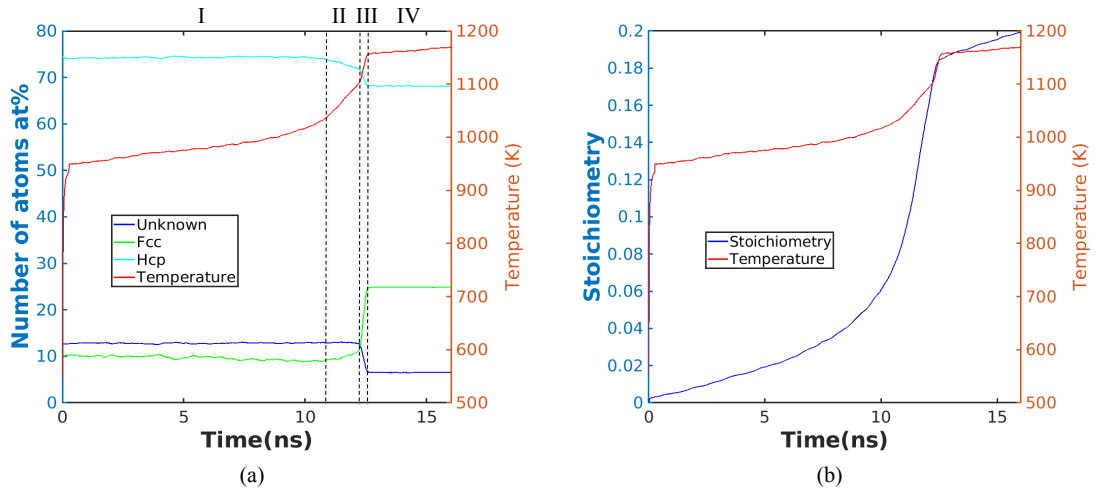

Figure 5.8: (a): Temperature T (scale in K, on the right) and number of atoms in at% (on the left) as a function time (scale in ns). The number of atoms in *fcc, hcp* and unknown configuration are represented. The different stages in the evolution are indicated by the dashed lines. (b): Temperature T (scale in K, on the right) and stoichiometry (on the left) as a function time (scale in ns).

in temperature is associated with the crysallization of the inner layer with a stoichiometry around 0.23.

IV In the last stage (IV), the temperature reaches a plateau. Other indicators are stable. The system is completely crystallized and its structure doesn't changes over time.

The number density profile at t = 0.4 ns in Fig. 5.9a shows the amorphization of Al atoms in the inner layer due to melting. Although the temperature was larger than the melting temperature of Al, the Al atoms remained arranged in layers close to the interface. During the adiabatic evolution of the system, the Ti atoms invade the inner layer as the stoichiometric factor ξ progressively increases while the Al are reorganized in planes (see Fig. 5.9b). At the interfaces, the transient formation of a solid solution $(Ti+Al)_{ss}$ was observed. Figure 5.9c demonstrates the recrystallization of the inner plane (6 planes) with a well-defined ratio between Al and Ti atoms. This ratio is slightly less than 0.25, the one expected for the formation of $TiAl_3$. The Ackland and Jones' analysis shows formation of a *fcc*-like structure except a twin defect formed by planes in hcp-like structure.

The increase in temperature is associated with two processes: the reactive dissolution between Ti and Al and the spontaneous crystallization of a new phase. The reactive dissolution plays an important role in the catalytic character of the reaction because an increase in temperature favors further dissolution of Ti in Al. In this simulation, the process of dissolution was interrupted by the phase transformation in an intermetallic

compound. Indeed, the stoichiometry in the inner layer increases up to a plateau with a value of 22 at% of titanium.

The phase transformation could be associated with an exothermic reaction giving rise to the formation of a new compound. If we suppose that is formed:

$$3\mathrm{Al} + \mathrm{Ti} \rightarrow \mathrm{TiAl_3} \tag{5.4}$$

The energy balance expressed in terms of cohesive energies reads

$$\frac{1}{4}[3 \times E_0(\mathrm{Al}) + E_0(\mathrm{Ti})] = E_0(\mathrm{TiAl_3}) + q \tag{5.5}$$

where $q = 0.30$ eV is the excess energy released by the atomic rearrangement or, equivalently, the formation energy of the compound $TiAl_3$. The intermetallic $TiAl_3$ is characterized by a $D0_{22}$ structure at high temperature. But the potential developed by Zope and Mishin [92] gives a very small difference between the two structures $D0_{22}$ and $L1_2$ of the $TiAl_3$. The structure $L1_2$ is 0.001 eV/atom smaller than the structure $D0_{22}$. According to this observation, the distinction between these two structures can't be really established in the context of the simulation.

Another simulation was carried out with an initial temperature of 1000 K. The number of atoms and the geometry remained the same. The system was created with the appropriate lattice parameter corresponding to 1000 K. As shown in Fig. 5.10, the dynamics follows the four stages described previously. During stage II, the temperature rise is even more pronounced. The dissolution is here more important and the stoichiometry reaches a plateau value of 34 at% and a maximum temperature $T_{\mathrm{ad}} = 1300$ K. The evolution towards the final temperature is done in a shorter time.

5.2.3 Thick sample results

In order to investigate the size effect, a thick sample was created at 1000 K. We performed the same analysis as previously. In this case, Fig. 5.11a shows only 3 stages: (I) slow increase in temperature and no configuration change, (II) rapid dissolution of Ti in the inner layer and (III) saturation toward the adiabatic temperature. The dissolution of Ti in the inner layer produces a release of heat. The adiabatic temperature is 1315 K and the saturation of the liquid solution is $\xi = 0.35$ as shown in Fig. 5.11b. No spontaneous crystallization was observed. After the NVE simulation in adiabatic conditions, the inner layer is a liquid solution $(0.35\ \mathrm{Ti} + 0.65\ \mathrm{Al})_{\mathrm{liq}}$. Figure 5.12 at $t = 5$ ns gives the number density profile and the corresponding snapshot of the system during stage (I). Although the inner layer is Al liquid, a structural ordering close to the interfaces was noticed. Figure 5.12 at $t = 20$ ns corresponds to the coexistence of solid outer layers surrounding the liquid solution of Ti and Al. As shown in Fig. 5.12, 3.5 ns after the start of the cooling demonstrates the complete reorganization in atomic planes with a constant ratio between Ti and Al in each plane. All atoms of the inner layer have a *fcc* local configuration as proven in Fig. 5.11c.

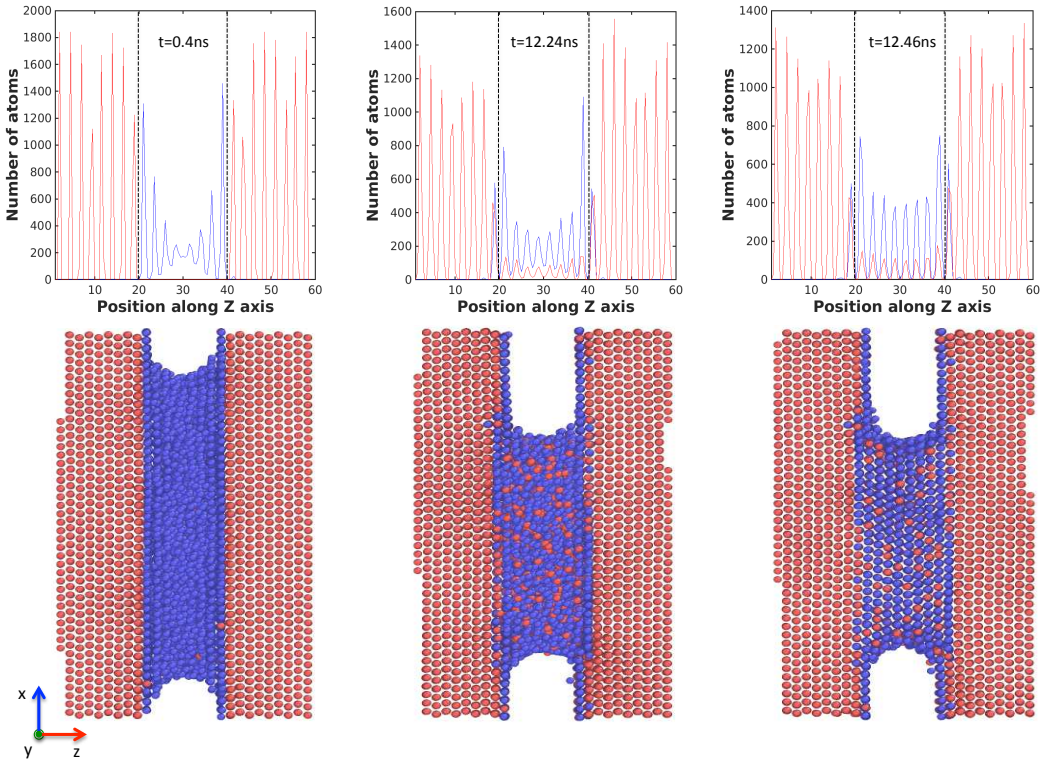

Figure 5.9: Number density profiles at t = 0.4, 12.24, 12.46 ns in the z-direction, perpendicular to the interfaces. The dashed lines indicate the limits of the inner layer in the initial configuration. Corresponding snapshots of the system. Position is measured in Angstroms.

Dissolution is the main process in the self-sustained character of the reaction in the Ti-Al system. Above the melting point of Al, Ti dissolve in the liquid Al layer. Figure 5.13 gives the coverage of 4 planes below the lower interface. A similar behavior was observed for the upper interface. The following features were identified:

1. The Ti atoms close to the interfaces leave the solid substrate more easily than atoms located deeper. Nevertheless, the number of liquid atoms (marked as amorphous atoms) doesn't significantly increase.

2. The vacancies liberated by outgoing Ti atoms are occupied by incoming Al atoms very quickly. Most Al atoms adopt a local fcc arrangement while Ti atoms are becoming liquid. The Al atoms occupy substitutional positions in the first atomic plane (# -1) below the interface.

3. The mobility of Al atoms is limited in outer layers because of the lack of local defects and the inefficient diffusion in solid-phase. As shown in Fig.5.13, the first plane below the interface is completely depleted by Ti atoms and progressively

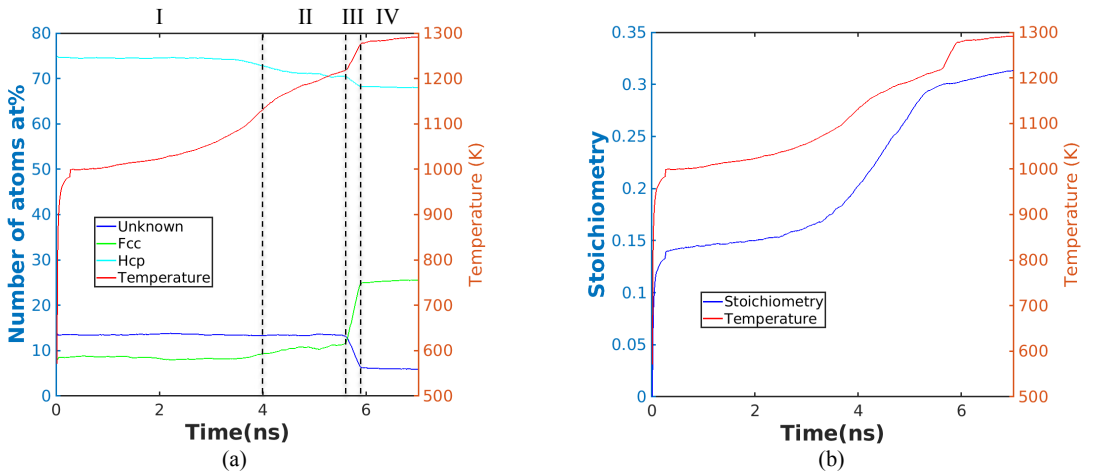

Figure 5.10: Initial temperature of 1000 K. (a): Temperature T (scale in K, on the right) and number of atoms in at% (on the left) as a function time (scale in ns). The number of atoms in fcc, hcp and unknown configuration are represented. The different stages in the evolution are indicated by the dashed lines. (b): Temperature T (scale in K, on the right) and stoichiometry (on the left) as a function time (scale in ns).

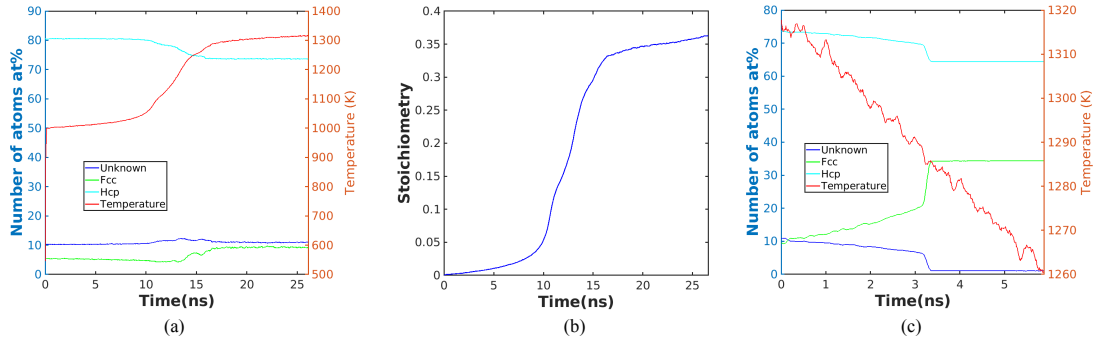

Figure 5.11: Thick sample. Initial temperature of 1000 K. (a): Temperature T (scale in K, on the right) and number of atoms in at% (on the left) as a function time (scale in ns) during the heating. The number of atoms in fcc, hcp and unknown configuration are represented. (b) Stoichiometry (on the left) as a function time (scale in ns). (c): Temperature T (scale in K, on the right) and number of atoms in at% (on the left) as a function time (scale in ns) during the cooling.

covered by Al atoms. Defects (vacancies and line defects) are created in plane (# -1).

4. In about 10 ns, 50 at% of Ti of the first atomic plane below the interface are dissolved. At 12 ns, the number of Ti reaches a minimum value. Remaining Ti (< 20 at%) are located on the free surfaces.

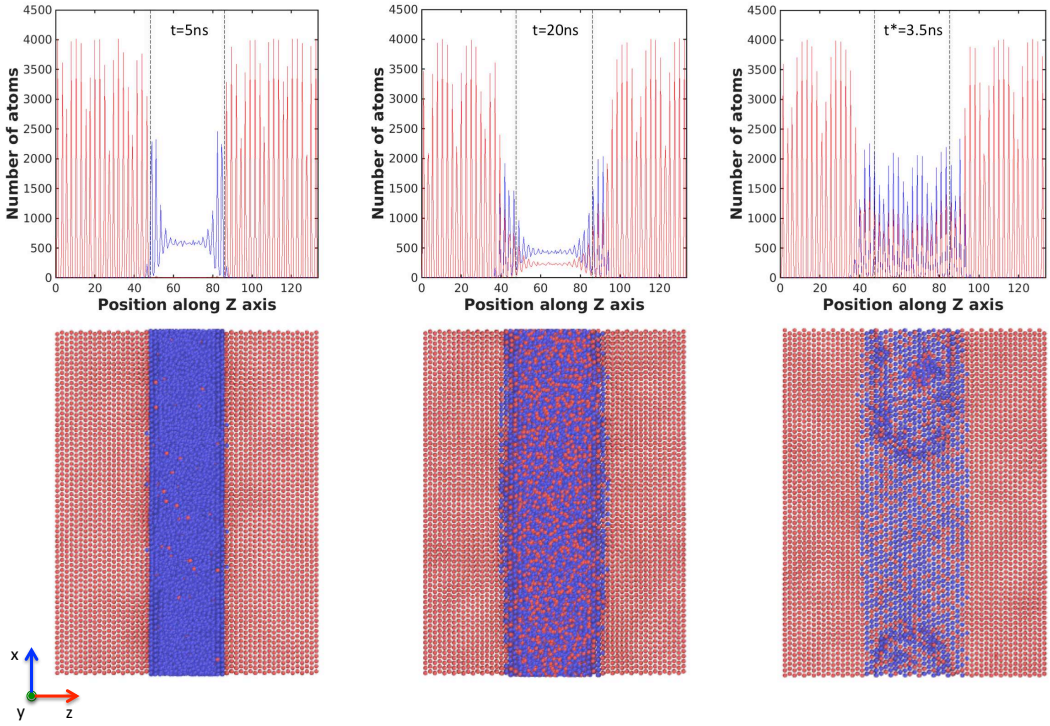

Figure 5.12: Number density profiles at t = 5, 20 ns in the z-direction, perpendicular to the interfaces, and 3.5 ns after the start of the cooling. The dashed lines indicate the limits of the inner layer in the initial configuration. Corresponding snapshots of the system. Position is measured in Angstroms.

5. When the number of Ti in the plane (# -1) is significantly reduced, the second plane (# -2) starts to be depleted and the number of Ti in the plane (# -1) increases again and reaches a value of 32 at%. The dissolution process operates plane by plane as shown in Fig. 5.13.

6. After the dissolution of 70 at% of Ti atoms in 3 planes, the system reaches a state Ti_{sol} - $(Ti_x + Al_{1-x})_{ss}$ - $(Ti_y + Al_{1-y})_{liq}$

In the case of liquid mixtures, Titanium and Aluminum are characterized by a negative mixing enthalpy:

$$\Delta H_{mix}(T) = H_{Ti-Al}(T) - [(1 - x_{Ti})\, H_{Al}(T) + x_{Ti}\, H_{Ti}(T)] \tag{5.6}$$

At the atomistic level, the scheme (Fig. 5.14) shows the elemental process associated with dissolution: a liquid atom Al will be exchanged with a solid Ti atom. As an example, a set of atoms were followed. For instance, the potential energy of the Al atom in the liquid layer is around - 3.28 eV and decreases to -5.48 eV when it substitutes a Ti

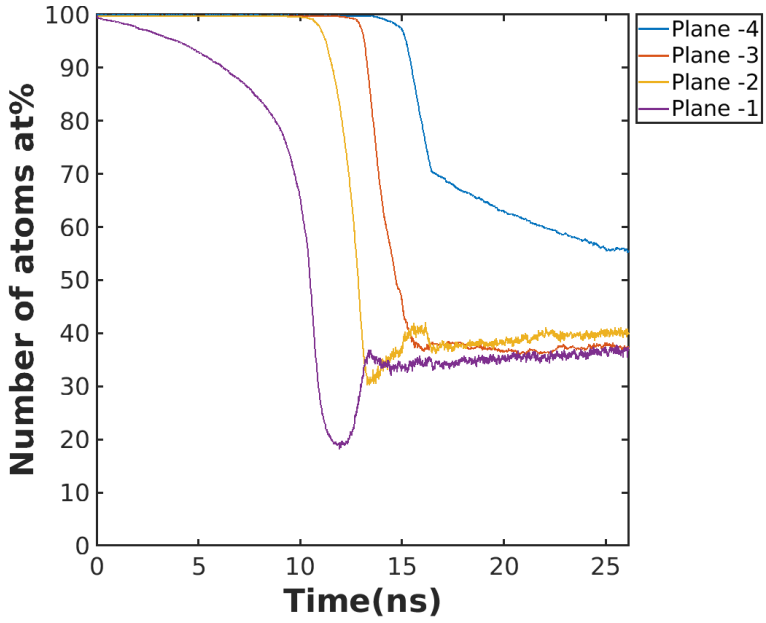

Figure 5.13: Number of Ti atoms (at%) in the atomic planes close to the interface. The plane (# -1) is the plane just below the interface, the plane (# -2) is below the plane (#-1), etc.

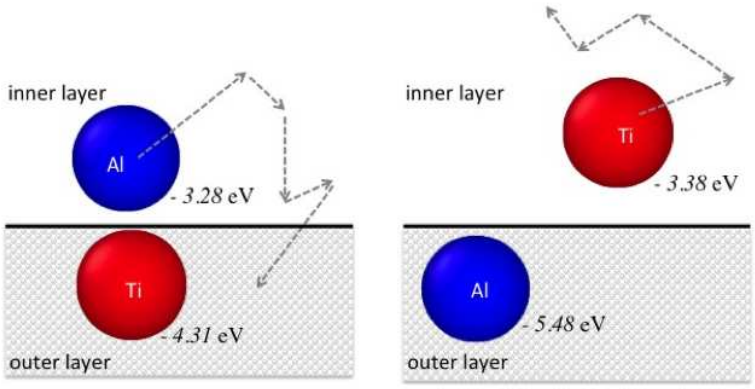

Figure 5.14: Schematic representation of the dissolution process.

in the outer solid layer. The Ti atom in the solid has a potential energy of -4.31 eV and increases to -3.38 eV when it disolves in the inner liquid layer. The energetic balance reads:

$$E(\mathrm{Al_{liq}}) + E(\mathrm{Ti_{sol}}) = E(\mathrm{Al_{Ti-sol}}) + E(\mathrm{Ti_{Al-liq}}) + q_{\mathrm{diss}} \tag{5.7}$$

where q_{diss} represents the excess of energy release by the dissolution process: the heat of dissolution q_{diss} = 1.27 eV. The energy transfer associated with all dissolved atoms induces the increase of T up to 1315 K.

During the exchange between Al and Ti atoms, a single incoming Al atom surrounded by Ti atoms induces a slight change in the potential energy of Ti nearest neighbours

depicted by the area a in Fig. 5.15. The substitution of several Al atoms in a vicinity induces a significant modification of neighbouring atoms depicted by the area b in Fig. 5.15. Such group of atoms will play the role of a nucleus for further dissolution.

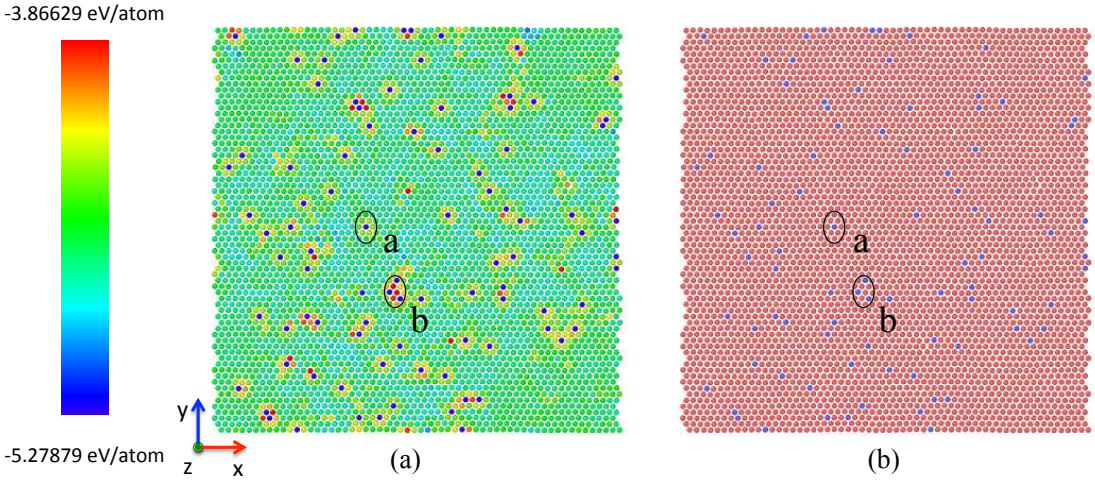

Figure 5.15: Snapshot of atomic plane #-1. (a): potential energy /atom. (b): species index (Al is blue and Ti is red). Time t = 2ns.

5.3 Summary

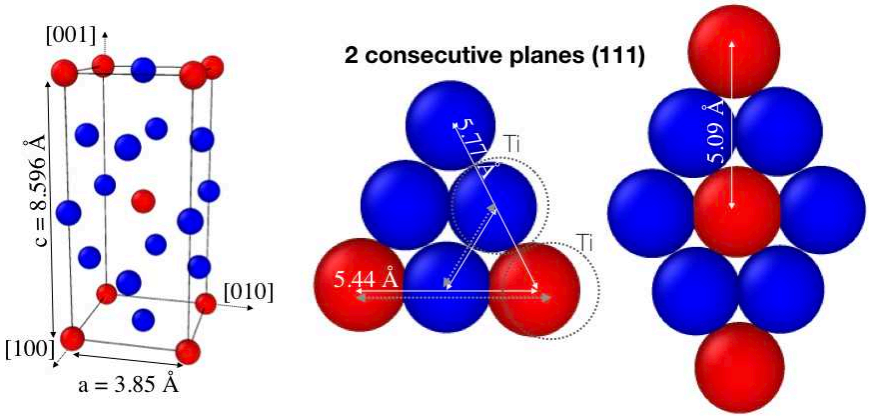

Figure 5.16: $D0_{22}$ crystallographic structure of $TiAl_3$ and two consecutive (111) planes in $TiAl_3$. The (002) plane of pure Ti is shown in dashed. Al in blue and Ti in red.

The reactivity of the Ti-Al system has been studied by means of molecular dynamics simulations and experiments. The main features are as follows:

- No reaction occurs at a temperature below the melting point of Al. The interface between (002)-Ti plane and (111)-Al plane is very stable due to the small

mismatch between the two structures. In addition, the metallic radius of Ti is slightly larger than the Al metallic radius:

$$r_{\text{metal}}(\text{Ti}) = 1.47 \text{ pm} \quad r_{\text{metal}}(\text{Al}) = 1.43 \text{ pm} \tag{5.8}$$

This fact explains the lack of solubility of Ti in Al solid.

- When the system is heated above the melting temperature of Al, we observed an exothermic self-sustained dynamics until a plateau value of T is reached. The behavior is similar to the phenomenon of adiabatic explosion.
- The first phase transformation to occur at high temperature is the amorphization of the Al inner layer, except close the interfaces where Al exhibits a structural ordering.
- The dissolution of Ti in Al is associated with an exothermic mixing of the two metals. The heat released due to dissolution is the main heat source.
- The dissolution operates as an exchange of Ti and Al atoms at interfaces. There is no net flux at the interface.
- The adiabatic temperature depends on the initial temperature value. The same is true for the saturation value of the liquid solution.
- The spontaneous formation of an intermetallic compound was only observed in the small systems. The phase transformation is very rapid (less than 0.2 ns).
- In the large system, the crystallization of the intermetallic compound occurs during the cooling simulation at 2988 K. The growth of the intermetallic develops plane by plane starting from the interface.
- The intermetallic compound is ($\text{Ti}_y\ \text{Al}_{1-y}$) with $y \sim 0.3$. The interatomic potential developed by Zope and Mishin predicts a single Al-rich phase $\text{Ti}_{0.25}\text{Al}_{0.75} \equiv \text{TiAl}_3$. The simulation results demonstrate the formation of an intermetallic with a well-defined composition and a local fcc configuration, close to the TiAl_3 compound. As shown in Fig.5.16, the TiAl_3 intermetallic can easily grow on a Ti plane. Substitution of Ti atoms by Al ones and a slight displacement of Ti gives the specific structure. Moreover the $D0_{22}$ structure is based on a face centered cubic structure.

Chapter 6

General conclusions and perspectives

This work focused on the numerical modelling of powder metallurgy processes by means of molecular dynamics (MD) simulations. Two processes were investigated, namely the solidification process in the context of additive manufacturing and the mechanical treatment of powders (i.e., mechanical activation due to milling). The results of MD simulations are reported in Chapters 3 to 5. These simulations required 7 million hours of computing time on the LINUX cluster at the computer center of the University of Burgundy.

The simulations were performed using many-body potentials that are well suited for metallic systems. These potentials are fitted on specific physical properties provided by experimental and numerical (*ab-initio* calculations) data. The reliability of MD simulations depends on the accuracy of the interatomic potentials. As explained in Chapter 2, we performed certain specific calculations to evaluate the validity of the potentials used in this work. Moreover, in order to interpret the results, we computed useful properties: the latent heat of fusion, the melting temperature, the thermal conductivity, the thermal expansion and the solid/liquid interface energy.

Chapter 3 deals with the solidification of Ni in the context of additive manufacturing. For this purpose, two specific systems were designed to model the directional solidification of the melt pool above a polycrystalline substrate. In the model without imposed cooling, columnar growth with a planar solid/liquid interface was observed whatever the value of the substrate temperature. When a cooling rate was imposed, we observed three different microstructures according to the temperature gradient, the substrate temperature and the cooling rate. Columnar microstructures followed by the formation of equiaxed grains were observed when the undercooling temperature in the liquid reached a temperature of over 500 K with a sufficiently high cooling rate. The formation of equiaxed grains is directly related to the homogeneous nucleation event. On the other hand, when the cooling rate was too low (in our case 75 K/ns),

the columnar growth reached the end of the box of simulation. The temperature in the liquid was not sufficient to observe any nucleation event because the undercooling temperature was too low (below 500 K). Moreover, a substrate temperature of 1300 K resulted in the formation of cells. As discussed in the corresponding chapter, instabilities of the front in pure metals are directly related to the negative gradient in the liquid. These instabilities will progressively gives rise to the formation of protrusions which will transform into cells. Results are summarized in Fig. 6.1 according to the cooling mode, substrate temperature and cooling rate. The originality of the present work relies on the interpretation of our numerical results obtained at a nanoscale with theories of solidification and nucleation developed at micro/macroscale.

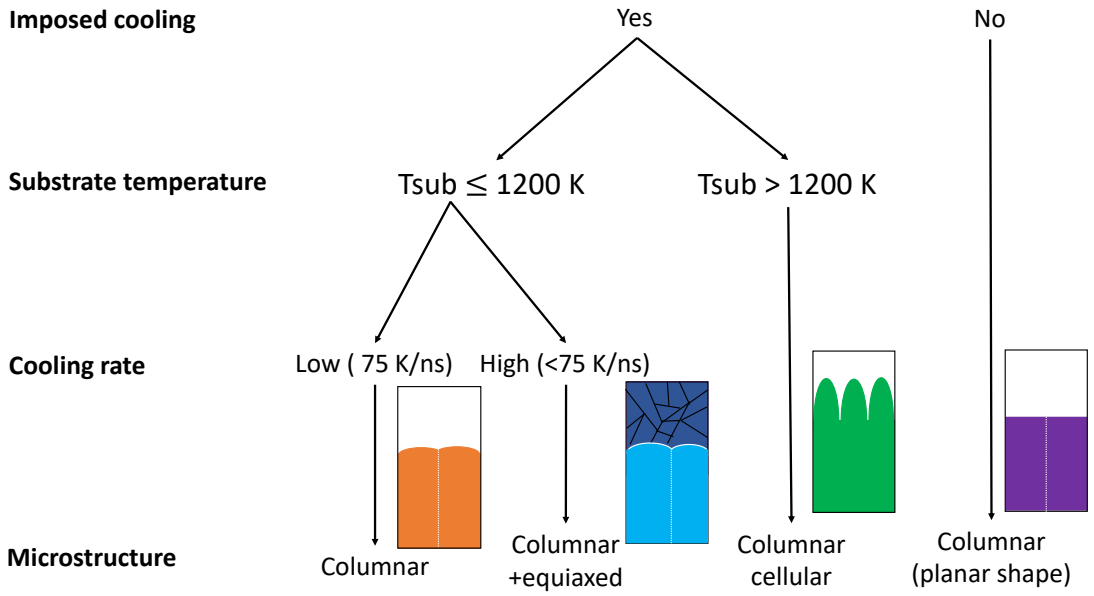

Figure 6.1: Schematic representation of the several microstructures of nickel obtained after solidification as a function of the cooling mode, substrate temperature and cooling rate.

In the last two chapters, the reactivity of composite powders was studied via two different approaches. In Chapter 4, the reactivity and diffusion of titanium-aluminum (Ti-Al) and nickel-aluminum (Ni-Al) systems after severe plastic deformation due to mechanical activation by milling were studied. In Chapter 5, we designed a laminated system appropriate to study the reactivity of titanium-aluminum reactive laminated particles.

In order to investigate the enhanced reactivity due to mechanical activation, we elaborated a system containing a large number of interfaces and defects as observed after high-energy ball milling. The action of the grinding balls on the powder is very complex. Ball-to-ball and ball-to-wall collisions are an important source of modification to the initial microstructure of the powder. To understand such modifications, we developed a mechanical impact model on a set of metallic particles at the microscopic

scale in order to identify the modifications induced in the microstructure as a result of mechanical activation and to evaluate the reactivity of the activated powders. In a first step, polycrystalline particles were subjected to progressive uniaxial compression to produce severe plastic deformation. In a second step, the deformed samples were heated to the temperatures of interest (*i.e.*, around the melting temperature of aluminum).

We were able to demonstrate that compression induces compaction and severe plastic deformation that creates complex mixing zones between elements at the surface contact between particles. The contacts between the particles create defects such as twins, dislocations or stacking faults in *fcc*-structures (Ni particles). After the plastic deformation, initial *hcp*-Ti particles show a high number of *fcc* atoms, indicating the presence of a huge number of linear/planar defects. Temperature setting allowed us to study the diffusion in activated Ti-Al and Ni-Al powders; the diffusion coefficients were evaluated in the mixing zones for these systems. Reactivity was studied in order to better understand mechanisms including the formation of intermetallics, grain coarsening, etc.

In Chapter 5, we considered a simplified model consisting of an aluminum layer between two titanium layers in order to mimic lamellar particles obtained via a planetary ball mill. Different mechanisms according to temperature were in this way revealed. For temperatures below the melting temperature of aluminum, the system remained stable and no exothermic reaction appeared in the solid state. For temperatures above the melting temperature of aluminium, a self-sustained behavior arising from the exothermic dissolution of titanium in the liquid aluminium layer was observed. The dissolution remained limited by the low solubility of titanium in liquid aluminium. The exothermic reaction continued until the recrystallization of the system and the formation of the intermetallic $TiAl_3$. In order to understand the size effects (thickness of the layer), we considered a thicker sample. The system reacted similarly to the smaller sample, although no spontaneous recrystallization was observed. Cooling was therefore necessary for recrystallization and the formation of the $TiAl_3$ intermetallic to occur. This thicker system also allowed us to analyze more finely the dissolution mechanisms of Ti in Al. Titanium dissolves plane by plane until saturation. The molecular dynamics approach thus highlighted the fact that the dissolution takes place via exchange between an aluminium atom and a titanium atom at the interfaces.

Working in parallel, our Russian collaborators[1] contributed to this study by developing an experimental approach. They studied the reactivity of lamellar particles produced via high-energy ball milling. By evaluating the activation energies, they identified two different behaviors. The first is associated with solid state transformation at interfaces below the melting temperature of aluminum. The second corresponds to the dissolution of titanium in liquid aluminum and the formation of the intermetallic $TiAl_3$.

[1] In the framework of a PHC Kolmogorov RECIPES 2018-2021 with Pr. A. S. Rogachev and coworkers at MISiS University, Functional Nanoceramics Laboratory

• Perspectives

As discussed in Chapter 3, columnar grains cause anisotropic properties, reduce mechanical performance and increase hot tear tendency. One of the main objectives here was thus to promote the columnar to equiaxed transition. It is possible to form equiaxed grains using adequate parameters of the AM process that directly modify the temperature gradient and the solidification rate, as reported by [164]. However, the low thermal gradient required for the formation of equiaxed grains remains difficult to achieve, even when adapting the process parameters. One of the strategies to promote the columnar to equiaxed transition is to inject nanoparticles, which serve as nucleation sites, into the melt pool to promote heterogeneous nucleation. Indeed, the energy barrier related to heterogeneous nucleation is lower than that of homogeneous nucleation. For instance, certain particles have demonstrated their efficiency in the context of AM of Al-based metals, namely Al_3Sc [165], TiB_2 [166], Al_3Zr [167], and TiC [168]. The main difficulty is finding sufficiently stable and powerful nucleant particles.

In order to reproduce these phenomena at the atomic scale, we considered adding NiAl particles to an Al melt pool based on the models we had previously developed. One of the main difficulties related to these materials stems from the progressive dissolution of NiAl particles (see Fig. 6.2). Indeed, the melting temperature difference between the NiAl intermetallic and Al is not sufficient to preserve the stability of the NiAl nanoparticles. It is for this reason that we chose to put this study aside at first. It is, however, quite frequent to observe this phenomenon of dissolution during the injection of particles carried out in the course of experiments. An interesting perspective would include performing a more systematic study of the dissolution of NiAl particles as a function of their size while they are subjected to different thermal conditions. There are several questions that arise in this context. Does the progressive dissolution of NiAl prevent the particles from acting as an inoculant promoting heterogeneous nucleation? Does dissolution, which is an exothermic process, necessarily prevent heterogeneous nucleation because of a local temperature increase? What is the role of the composition gradient generated by the progressive dissolution of nanoparticles? What are the effects of the cooling rates on the two mechanisms, namely heterogeneous nucleation and dissolution? An alternative approach would be to choose a system in which the dissolution is limited, allowing the particles to act as powerful nucleants. For instance, Al_3Ti particles are known to be strong nucleants for the solidification of the Al melt [169].

To avoid the problems arising from dissolution, one of the possible options is to consider metallic systems in which the difference between melting temperatures is significant, as for example copper (Cu) and tungsten (W). Experimentally, copper and tungsten have melting temperatures of 1358 K and 3695 K, respectively. In addition, tungsten has a bcc structure and copper has an fcc structure. There are different interatomic potentials for the Cu-W system and we considered the one developed by

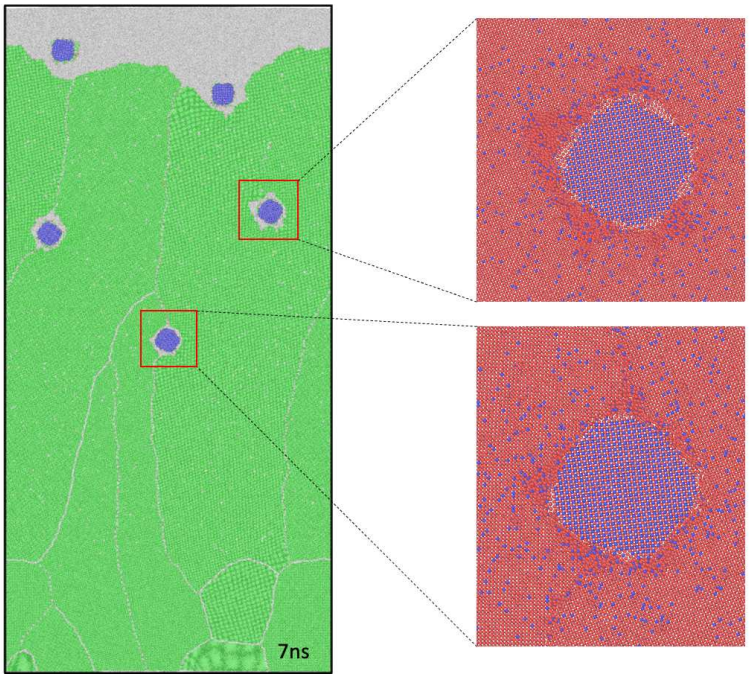

Figure 6.2: Snapshot of the system at the end of the simulation (7 ns). Left: fcc, bcc (NiAl) and amorphous atoms are represented in green, blue and white colors, respectively. Right: snapshot zooms of the red squares with Al and Ni atoms represented in red and blue colors, respectively. The Ni atoms progressively dissolved around NiAl particles.

Wei *et al.* [170] that is known to give an abnormally high melting temperature for tungsten. This, however, is an advantage for our study in which W particles play the role of nucleation sites and have to remain stable at high temperature. Using this potential, we computed crucial properties for solidification: the solid/liquid interface energy of Cu, the thermal expansion of both metals, the melting temperature of Cu and the thermal conductivity of Cu following the methods presented in Chapter 2. We studied heterogeneous nucleation using a simplified quasi-3D model containing a single W particle surrounded by Cu liquid. Various sizes of tungsten were considered, namely 1.59 nm, 7.95 nm and 23.85 nm, and different isothermal temperatures were applied to estimate the undercooling degree related to the free growth of copper. The degree of undercooling depends on the radius of the particle. For the smallest radius of 1.59 nm, the undercooling degree required to observe free growth was estimated to be 133 K, while the other two sizes were estimated at an undercooling degree between 40-50 K. Note that this method is similar to the one used in the context of liquid/solid interfacial energy presented in Chapter 2. The larger particles have lower undercooling temperatures than the smaller ones, as is frequently observed in heterogeneous nucleation processes. These results pinpointed more precisely the range of temperatures giving rise to the solidification of Cu from the W surfaces.

In a second step, we developed simulations similar to the ones used to study Ni solid-

ification but in this new case, several W particles were randomly added to a Cu melt. The model without imposed cooling gave interesting results that merit further investigation:

- The solid/liquid interface is locally disturbed where it crosses the W particles. A solidification delay is observed after the passage of a particle. Indeed, the Cu remains amorphous while the front around the particles continues to propagate with a flat shape. This solidification delay is directly related to the size of the particle: the larger the particle, the larger the zone in which the front is disturbed. The delay is nonetheless caught up in a few picoseconds because the temperature gradients in the liquid and in the solid are positive: the heat is extracted in the solid part of the Cu. The engulfment by the solidification interface is clearly shown in Fig. 6.3, right.
- Heterogeneous nucleation is not observed because the solidification temperature is relatively high (close to the melting temperature of Cu).
- A "groove" is observed at the grain boundaries located at the solid/liquid interfaces (also called triple junction). The grooving induces an opening angle depending on the solid/liquid surface tensions and the energy of the grain boundary. The grain boundaries cling to the particles when the opening angle is close enough. A progressive curvature of the grain boundary is also observed. This phenomenon seems very similar to the Zener pinning resulting from the interaction between particles and grain boundaries in polycrystalline materials (see Fig. 6.3, left). The pinning of boundaries by obstacles is an important effect in materials processing and its characterization requires further investigation.

The model with imposed cooling rate gives rise to several observations:

- The solidification front is also disturbed when it passes through particles. The delay is significantly different from that observed in the model without cooling. Indeed, the gradient in the liquid is negative: heat is released in the solid and the liquid. The solidification delay is therefore propagated over a longer period of time, even throughout the entire solidification process. An interesting next step would be to continue this work to better understand the effect of particles on a solidification front with a negative gradient in the liquid. How will these particles influence the solidified microstructure? Could the growth transform more easily into cellular/dendritic growth? How do the grain boundaries adapt to the presence of the particles?
- The same pinning by the dispersed particles is observed as in the model without imposed cooling.
- The temperature range giving rise to heterogeneous nucleation is relatively small. Indeed, the smallest particles favor heterogeneous nucleation at a temperature of 1050 K and the largest at 1160 K. The solidification rate of Cu is therefore low in this temperature range as it is relatively close to the melting tempera-

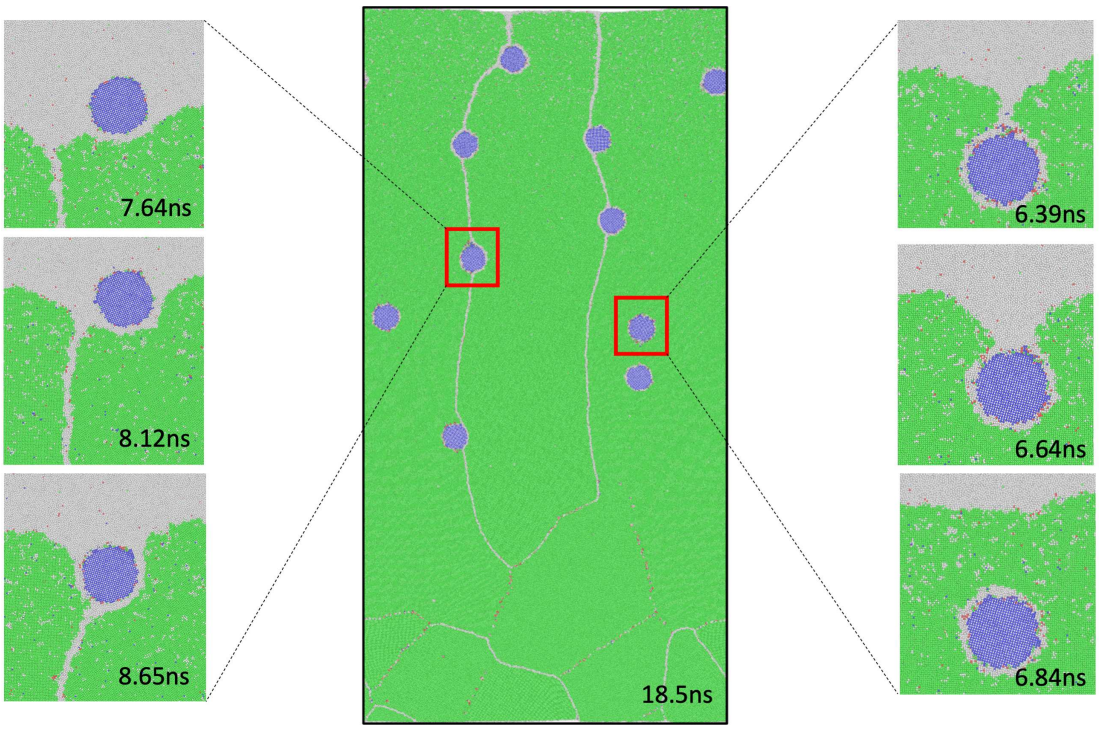

Figure 6.3: Snapshot of the system at the end of the simulation (18.5 ns) with bcc, fcc and amorphous atoms represented in blue, green and white, respectively. Left: snapshot zooms of the evolution of the grain boundary with progressive pinning on the particle of W. Right: snapshot zooms on the evolution of the Cu solid/liquid interface in presence of the W particle.

ture (1181K). We were nevertheless able to observe heterogeneous nucleation by properly choosing the thermostat temperatures and cooling rates (see Fig.6.4).

However, this results in a major problem related to the thermostats we use. For example, the temperature in the laser region is averaged over all atoms in the liquid region. The solidification front and heterogeneous nucleation are both exothermic processes releasing a very substantial amount of heat in the liquid region. Consequently, the atoms still in the liquid state have abnormally low temperatures to compensate for this heat release, results that may be questionable from a physical point of view. Note that we considered 10 particles. A smaller number of particles would be more appropriate to reduce the heat release effect and avoid this artifact. Further investigation of the method used should therefore be carried out in continuing this study.

Remaining in the context of solidification, several perspectives to my work might be considered:

- **Solidification of alloys**: Metal alloys are mainly used in additive manufacturing techniques. During the solidification of a pure metal, the effects are exclusively thermal. With an alloy, other phenomena such as chemical undercooling can be

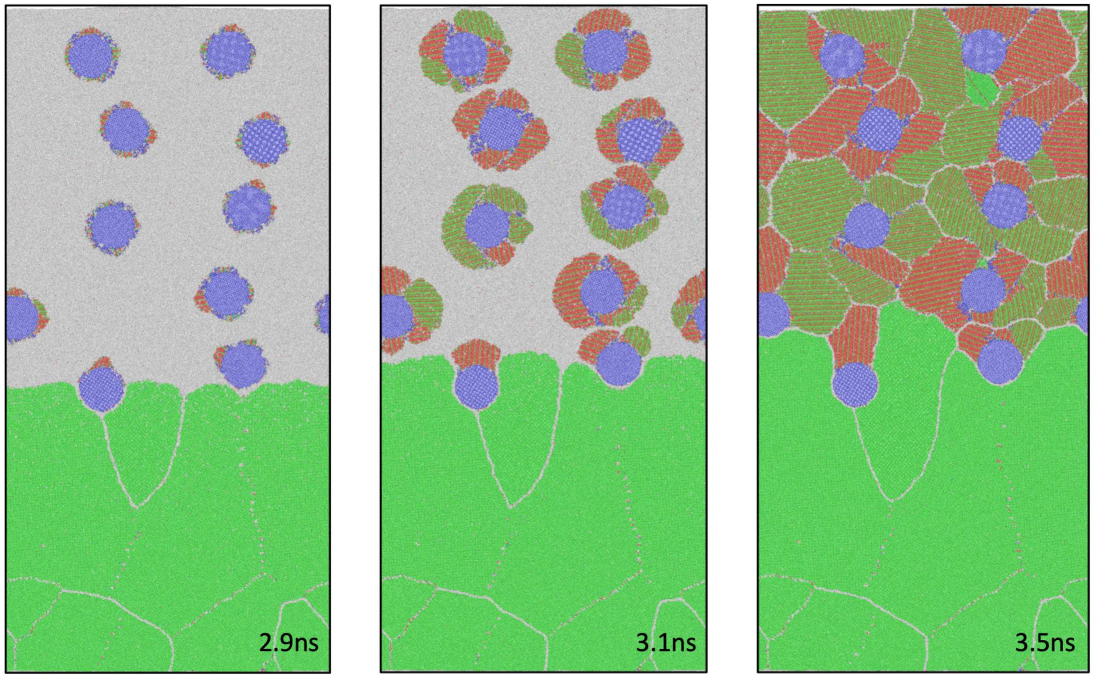

Figure 6.4: Snapshots of Cu-W system with an imposed cooling ramp of 215 K/ns at 2.9 ns, 3.1 ns and 3.5 ns (end of the simulation). The bcc, fcc, hcp, and amorphous atoms are represented in blue, green, red and white, respectively. Heterogeneous nucleation is observed around the particles of W.

studied. The solidification rate will also be different from that of a pure metal. A preliminary work was carried out by adding 5% of Al atoms to the Ni samples, adopting the same model as in the study of Ni in the presence of an imposed cooling. In the case of pure Ni, with a substrate temperature of 1300 K, dendritic/cellular growth has been observed. Under the same thermal conditions (substrate temperature and cooling rate), the microstructure was completely different for the Ni-Al alloy. We observed the formation of equiaxed grains upstream of the front. It would certainly be interesting to carry out an in-depth study on Ni-Al alloys. Several questions would have to be clarified: What is the influence of the Al percentage? What microstructures will be formed? Will a compositional gradient upstream of the front be set up during solidification as is commonly observed in experiments? Dendrites, which are often associated with alloys, could also be studied in further detail.

- **Solidification maps**: In the course of our study of solidification, we observed different microstructures related to solidification rates, thermal gradients, substrate temperatures and cooling rates. It would be interesting to quantify more precisely the transition between flat columnar growth and cellular growth in metallic alloys. Indeed, experimenters rely on solidification maps; such maps

are particularly based on thermal gradients and solidification rates. An interesting perspective would be to compare these maps with results obtained from molecular dynamics.

- **Particle inoculation**: Crystal growth on inoculating particles is an exothermic process. The heat, released locally in the liquid, causes a significant increase in temperature. This phenomenon is also a function of the density of the inoculating particles where heterogeneous nucleation occurs. The undercooling degree depends on the size of the particles. It could be interesting to introduce several particles of different sizes into a liquid bath by imposing a cooling. Different questions would have to be considered: Will the heat released by the growth around the larger particles prevent the growth on the smaller ones? What would the distances between particles need to be in order to observe growth on all particles? It might also be interesting to consider the size distribution of the particles.
- **Convection**: Additive manufacturing techniques cause convection in the liquid bath. A comparison between the models we have studied on the solidification of Ni with models that take convection into account could provide a better understanding of the influence of convection on solidification. Moreover, the addition of inoculant particles in the liquid bath would also be an interesting situation to consider. What would the movements of these particles be? What would their positions at the end of solidification be? Would it be possible to observe heterogeneous nucleation in the presence of convective phenomena?

As mentioned above, most of the items listed in the context of future perspectives have been the subject of preliminary calculations to design the simulations, to determine what is feasible and to identify technical difficulties. Beyond these preliminary studies that open up many opportunities, it will be necessary to perform a systematic and thorough study in order to better understand the role played by the inoculation of particles in the melt pool of pure metals and alloys.

Bibliography

[1] Saurav Goel et al. “Horizons of modern molecular dynamics simulation in digitalised solid freeform fabrication with advanced materials”. *Materials Today Chemistry* 18 (2020).

[2] Felix H Kim and Shawn P Moylan. *Literature review of metal additive manufacturing defects*. Tech. rep. NIST AMS 100-16. National Institute of Standards and Technology, 2018, NIST AMS 100–16.

[3] John J. Lewandowski and Mohsen Seifi. “Metal Additive Manufacturing: A Review of Mechanical Properties”. *Annual Review of Materials Research* 46.1 (2016), pp. 151–186.

[4] Nick Tepylo, Xiao Huang, and Prakash C. Patnaik. “Laser-Based Additive Manufacturing Technologies for Aerospace Applications”. *Advanced Engineering Materials* 21.11 (2019), p. 1900617.

[5] Pritam Anant Pidge and Harish Kumar. “Additive manufacturing: A review on 3 D printing of metals and study of residual stress, buckling load capacity of strut members”. *Materials Today: Proceedings*. International Conference on Mechanical and Energy Technologies 21 (2020), pp. 1689–1694.

[6] C. Doñate-Buendia et al. “Effect of nanoparticle additivation on the microstructure and microhardness of oxide dispersion strengthened steels produced by laser powder bed fusion and directed energy deposition”. *Procedia CIRP*. 11th CIRP Conference on Photonic Technologies [LANE 2020] 94 (2020), pp. 41–45.

[7] William E. Frazier. “Metal Additive Manufacturing: A Review”. *Journal of Materials Engineering and Performance* 23.6 (2014), pp. 1917–1928.

[8] Ana Vafadar et al. “Advances in Metal Additive Manufacturing: A Review of Common Processes, Industrial Applications, and Current Challenges”. *Applied Sciences* 11.3 (2021), p. 1213.

[9] B. Dutta and F. H. Froes. “The Additive Manufacturing (AM) of titanium alloys”. *Metal Powder Report* 72.2 (2017), pp. 96–106.

[10] Nesma T. Aboulkhair et al. “3D printing of Aluminium alloys: Additive Manufacturing of Aluminium alloys using selective laser melting”. *Progress in Materials Science* 106 (2019), p. 100578.

[11] Sudarsanam Suresh Babu et al. “Additive Manufacturing of Nickel Superalloys: Opportunities for Innovation and Challenges Related to Qualification”. *Metallurgical and Materials Transactions. A, Physical Metallurgy and Materials Science* 49.9 (2018).

[12] V. Ocelík et al. “Additive Manufacturing of High-Entropy Alloys by Laser Processing”. *JOM* 68.7 (2016), pp. 1810–1818.

[13] Nima Haghdadi et al. “Additive manufacturing of steels: a review of achievements and challenges”. *Journal of Materials Science* 56.1 (2021), pp. 64–107.

[14] Telma Ferreira et al. “Additive Manufacturing in Jewellery Design”. 2013, pp. 187–194.

[15] Timothy J. Horn and Diana Gamzina. “Additive Manufacturing of Copper and Copper Alloys” (2020).

[16] Amir Mostafaei, Jerard Gordon, and Anthony Rollett. “Additive Manufacturing of Cobalt Alloys”. 2019, pp. 374–379.

[17] Shuang Bai and Jian Liu. “Additive manufacturing of bimetallic structures”. *SN Applied Sciences* 2.7 (2020), p. 1152.

[18] Douglas C Hofmann et al. “Compositionally graded metals: A new frontier of additive manufacturing”. *J. Mater. Res.* 29.17 (2014), p. 12.

[19] Valmik Bhavar et al. “A review on powder bed fusion technology of metal additive manufacturing”. *Additive Manufacturing Handbook*. 2017.

[20] Dong-Gyu Ahn. “Direct metal additive manufacturing processes and their sustainable applications for green technology: A review”. *International Journal of Precision Engineering and Manufacturing-Green Technology* 3.4 (2016), pp. 381–395.

[21] Annamaria Gisario et al. “Metal additive manufacturing in the commercial aviation industry: A review”. *Journal of Manufacturing Systems* 53 (2019), pp. 124–149.

[22] Liping Zheng et al. “Melt pool boundary extraction and its width prediction from infrared images in selective laser melting”. *Materials & Design* 183 (2019), p. 108110.

[23] Michael Bermingham et al. “Revealing the Mechanisms of Grain Nucleation and Formation During Additive Manufacturing”. *JOM* 72.3 (2020), pp. 1065–1073.

[24] Pengwei Liu et al. “Insight into the mechanisms of columnar to equiaxed grain transition during metallic additive manufacturing”. *Additive Manufacturing* 26 (2019), pp. 22–29.

[25] H. Jung et al. “Columnar to equiaxed transition during directional solidification in refined Al-based alloys”. *Journal of Alloys and Compounds* 484.1 (2009), pp. 739–746.

[26] J. D. Hunt. “Steady state columnar and equiaxed growth of dendrites and eutectic”. *Materials Science and Engineering*. Solidification Microstructure: 30 Years after Constitutional Supercooling 65.1 (1984), pp. 75–83.

[27] W. Kurz, C. Bezençon, and M. Gäumann. “Columnar to equiaxed transition in solidification processing”. *Science and Technology of Advanced Materials* 2.1 (2001), pp. 185–191.

[28] M. Gäumann et al. “Single-crystal laser deposition of superalloys: processing–microstructure maps”. *Acta Materialia* 49.6 (2001), pp. 1051–1062.

[29] M. J. Bermingham et al. “Promoting the columnar to equiaxed transition and grain refinement of titanium alloys during additive manufacturing”. *Acta Materialia* 168 (2019), pp. 261–274.

[30] Joel Heang Kuan Tan, Swee Leong Sing, and Wai Yee Yeong. “Microstructure modelling for metallic additive manufacturing: a review”. *Virtual and Physical Prototyping* 15.1 (2020), pp. 87–105.

[31] J. A. Spittle. “Columnar to equiaxed grain transition in as solidified alloys”. *International Materials Reviews* 51.4 (2006), pp. 247–269.

[32] Wilfried Kurz, Michel Rappaz, and Rohit Trivedi. “Progress in modelling solidification microstructures in metals and alloys. Part II: dendrites from 2001 to 2018”. *International Materials Reviews* 66.1 (2021), pp. 30–76.

[33] Elaheh Dorari et al. “Growth competition between columnar dendritic grains - The role of microstructural length scales”. *Acta Materialia* 223 (2022), p. 117395.

[34] Sachin Kurian and Reza Mirzaeifar. “Selective laser melting of aluminum nanopowder particles, a molecular dynamics study”. *Additive Manufacturing* 35 (2020), p. 101272.

[35] J. Lu and J. A. Szpunar. “Molecular-dynamics simulation of rapid solidification of aluminum”. *Acta Metallurgica et Materialia* 41.8 (1993), pp. 2291–2295.

[36] Ze-An Tian et al. “Molecular dynamics simulation for cooling rate dependence of solidification microstructures of silver”. *Journal of Non-Crystalline Solids* 354.31 (2008), pp. 3705–3712.

[37] Q. X. Pei, C. Lu, and M. W. Fu. “The rapid solidification of Ti_3Al : a molecular dynamics study”. *Journal of Physics: Condensed Matter* 16.24 (2004), pp. 4203–4210.

[38] Z. Y. Hou et al. “Cooling rate dependence of solidification for liquid aluminium: a large-scale molecular dynamics simulation study”. *Physical Chemistry Chemical Physics* 18.26 (2016), pp. 17461–17469.

[39] Franck Celestini and Jean-Marc Debierre. “Measuring kinetic coefficients by molecular dynamics simulation of zone melting”. *Physical Review E* 65.4 (2002), p. 041605.

[40] D. Y. Sun, M. Asta, and J. J. Hoyt. “Kinetic coefficient of Ni solid-liquid interfaces from molecular-dynamics simulations”. *Physical Review B* 69.2 (2004), p. 024108.

[41] F. Celestini and J. M. Debierre. “Nonequilibrium molecular dynamics simulation of rapid directional solidification”. *Physical Review B* 62.21 (2000), pp. 14006–14011.

[42] Avik Mahata and Mohsen Asle Zaeem. “Effects of solidification defects on nanoscale mechanical properties of rapid directionally solidified Al-Cu Alloy: A large scale molecular dynamics study”. *Journal of Crystal Growth* 527 (2019), p. 125255.

[43] Mehran Bahramyan et al. “Nano-scale simulation of directional solidification in TWIP stainless steels: A focus on plastic deformation mechanisms”. *Materials Science and Engineering: A* 812 (2021), p. 140999.

[44] Yasushi Shibuta et al. “Homogeneous nucleation and microstructure evolution in million-atom molecular dynamics simulation”. *Scientific Reports* 5.1 (2015), p. 13534.

[45] Avik Mahata, Mohsen Asle Zaeem, and Michael I Baskes. “Understanding homogeneous nucleation in solidification of aluminum by molecular dynamics simulations”. *Modelling and Simulation in Materials Science and Engineering* 26.2 (2018), p. 025007.

[46] Takuya Fujinaga and Yasushi Shibuta. “Molecular dynamics simulation of athermal heterogeneous nucleation of solidification”. *Computational Materials Science* 164 (2019), pp. 74–81.

[47] C. Suryanarayana. “Mechanical alloying and milling”. *Progress in Materials Science* 46.1 (2001), pp. 1–184.

[48] Peter Baláž et al. “Hallmarks of mechanochemistry: from nanoparticles to technology”. *Chemical Society Reviews* 42.18 (2013), pp. 7571–7637.

[49] Alexander S. Rogachev. “Mechanical activation of heterogeneous exothermic reactions in powder mixtures”. *Russian Chemical Reviews* 88.9 (2019), p. 875.

[50] S. Paris et al. “Spark plasma synthesis from mechanically activated powders: a versatile route for producing dense nanostructured iron aluminides”. *Scripta Materialia* 50.5 (2004), pp. 691–696.

[51] A. Fourmont et al. “Effects of planetary ball milling on AlCoCrFeNi high entropy alloys prepared by Spark Plasma Sintering: Experiments and molecular dynamics study”. *Journal of Alloys and Compounds* 820 (2020), p. 153448.

[52] A. A. Nepapushev et al. “Production of Rounded Reactive Composite Ti/Al Powders for Selective Laser Melting by High-Energy Ball Milling”. *Metallurgical and Materials Transactions B* 50.3 (2019), pp. 1241–1247.

[53] Quang Nguyen et al. “Nanocomposite thermite powders with improved flowability prepared by mechanical milling”. *Powder Technology* 327 (2018), pp. 368–380.

[54] Vladimir Popov et al. “Powder Bed Fusion Additive Manufacturing Using Critical Raw Materials: A Review”. *Materials* 14 (2021), p. 909.

[55] A. B. Spierings et al. “Powder flowability characterisation methodology for powder-bed-based metal additive manufacturing”. *Progress in Additive Manufacturing* 1.1 (2016), pp. 9–20.

[56] Kazybek Kassym and Asma Perveen. “Atomization processes of metal powders for 3D printing”. *Materials Today: Proceedings*. 10th International Conference of Materials Processing and Characterization 26 (2020), pp. 1727–1733.

[57] Christine Friederike Burmeister and Arno Kwade. “Process engineering with planetary ball mills”. *Chemical Society Reviews* 42.18 (2013), pp. 7660–7667.

[58] S. Beinert et al. “Analysis and modelling of bead contacts in wet-operating stirred media and planetary ball mills with CFD–DEM simulations”. *Chemical Engineering Science* 134 (2015), pp. 648–662.

[59] S. Rosenkranz, S. Breitung-Faes, and A. Kwade. “Experimental investigations and modelling of the ball motion in planetary ball mills”. *Powder Technology* 212.1 (2011), pp. 224–230.

[60] A. S. Rogachev et al. “Experimental investigation of milling regimes in planetary ball mill and their influence on structure and reactivity of gasless powder exothermic mixtures”. *Powder Technology* 274 (2015), pp. 44–52.

[61] Ulrich Hoffmann, Christian Horst, and Ulrich Kunz. “Reactive Comminution”. *Integrated Chemical Processes*. 2005, pp. 407–436.

[62] B. B. Khina. “Effect of mechanical activation on SHS: Physicochemical mechanism”. *International Journal of Self-Propagating High-Temperature Synthesis* 17.4 (2008), pp. 211–217.

[63] Alexander S. Mukasyan et al. “Mechanical activation and gasless explosion: Nanostructural aspects”. *Chemical Engineering Journal* 174.2 (2011), pp. 677–686.

[64] A. S. Rogachev et al. “Influence of the high energy ball milling on structure and reactivity of the Ni+Al powder mixture”. *Journal of Alloys and Compounds* 577 (2013), pp. 600–605.

[65] A. S. Rogachev et al. “Reactivity of mechanically activated powder blends: Role of micro and nano structures”. *International Journal of Self-Propagating High-Temperature Synthesis* 22.4 (2013), pp. 210–216.

[66] Christopher E. Shuck and Alexander S. Mukasyan. “Reactive Ni/Al Nanocomposites: Structural Characteristics and Activation Energy”. *The Journal of Physical Chemistry A* 121.6 (2017), pp. 1175–1181.

[67] S. Odunuga et al. “Forced Chemical Mixing in Alloys Driven by Plastic Deformation”. *Physical Review Letters* 95.4 (2005), p. 045901.

[68] Francesco Delogu. “Forced chemical mixing in model immiscible systems under plastic deformation”. *Journal of Applied Physics* 104.7 (2008), p. 073533.

[69] Alan C. Lund and Christopher A. Schuh. “Molecular simulation of amorphization by mechanical alloying”. *Acta Materialia* 52.8 (2004), pp. 2123–2132.

[70] J. E. Hammerberg, B. L. Holian, and S. J. Zhou. “Studies of sliding friction in compressed copper”. *AIP Conference Proceedings* 370.1 (1996), pp. 307–311.

[71] David A. Rigney and S. Karthikeyan. “The Evolution of Tribomaterial During Sliding: A Brief Introduction”. *Tribology Letters* 39.1 (2010), pp. 3–7.

[72] Nhon Q. Vo et al. “Atomic Mixing in Metals Under Shear Deformation”. *JOM* 65.3 (2013), pp. 382–389.

[73] En-Qiang Lin et al. “Molecular dynamics simulation of nano-scale interfacial friction characteristic for different tribopair systems”. *Applied Surface Science*. International Vacuum Congress (IVC-18) 258.6 (2012), pp. 2022–2028.

[74] Kai Chen et al. “Molecular dynamics simulation of microstructure evolution and heat dissipation of nanoscale friction”. *International Journal of Heat and Mass Transfer* 109 (2017), pp. 293–301.

[75] Mathew J. Cherukara et al. “Shock Loading of Granular Ni/Al Composites. Part 1: Mechanics of Loading”. *The Journal of Physical Chemistry C* 118.45 (2014), pp. 26377–26386.

[76] Mathew J. Cherukara et al. “Shock Loading of Granular Ni/Al Composites. Part 2: Shock-Induced Chemistry”. *The Journal of Physical Chemistry C* 120.12 (2016), pp. 6804–6813.

[77] Khachatur V. Manukyan et al. “Tailored Reactivity of Ni+Al Nanocomposites: Microstructural Correlations”. *The Journal of Physical Chemistry C* 116.39 (2012), pp. 21027–21038.

[78] A. Fourmont et al. “Reactivity of Ni–Al nanocomposites prepared by mechanical activation: A molecular dynamics study”. *Journal of Applied Physics* 129.6 (2021), p. 065301.

[79] D. R. Maurice and T. H. Courtney. “The physics of mechanical alloying: A first report”. *Metallurgical Transactions A* 21.1 (1990), pp. 289–303.

[80] Florence Baras et al. “Mechanical activation of metallic powders and reactivity of activated nanocomposites: a molecular dynamics approach”. *Applied Physics A* 127.7 (2021), p. 555.

[81] A. S. Rogachev et al. “Combustion in reactive multilayer Ni/Al nanofoils: Experiments and molecular dynamic simulation”. *Combustion and Flame* 166 (2016), pp. 158–169.

[82] D. P. Adams. “Reactive multilayers fabricated by vapor deposition. A critical review”. *Thin Solid Films* 576.C (2014).

[83] T. P. Weihs. “5 - Fabrication and characterization of reactive multilayer films and foils”. *Metallic Films for Electronic, Optical and Magnetic Applications*. Ed. by Katayun Barmak and Kevin Coffey. 2014, pp. 160–243.

[84] A. Sáenz-Trevizo and A. M. Hodge. “Nanomaterials by design: a review of nanoscale metallic multilayers”. *Nanotechnology* 31.29 (2020), p. 292002.

[85] Alexander S. Mukasyan, Alexander S. Rogachev, and Singanahally ThippaReddy Aruna. “Combustion synthesis in nanostructured reactive systems”. *Advanced Powder Technology*. Special issue of the 7th World Congress on Particle Technology 26.3 (2015), pp. 954–976.

[86] Seema Sen, Markus Lake, and Peter Schaaf. “Al-based binary reactive multilayer films: Large area freestanding film synthesis and self-propagating reaction analysis”. *Applied Surface Science*. AEM2017 - International conference on Advanced Energy Materials 474 (2019), pp. 243–249.

[87] Seema Sen et al. “Synthesis and characterization of Ti/Al reactive multilayer films with various molar ratios”. *Thin Solid Films* 631 (2017), pp. 99–105.

[88] Emília Illeková et al. “Kinetics of intermetallic phase formation in the Ti/Al multilayers”. *Thermochimica Acta* 469.1 (2008), pp. 77–85.

[89] J.C. Gachon et al. “On the mechanism of heterogeneous reaction and phase formation in Ti/Al multilayer nanofilms”. *Acta Materialia* 53.4 (2005), pp. 1225–1231.

[90] Oral Büyüköztürk et al. “Structural solution using molecular dynamics: Fundamentals and a case study of epoxy-silica interface”. *International Journal of Solids and Structures* 48.14 (2011), pp. 2131–2140.

[91] *Basic Crystal Concepts*. `http://home.iitk.ac.in/~sangals/crystosim/crystaltut.html`.

[92] Rajendra R. Zope and Y. Mishin. “Interatomic potentials for atomistic simulations of the Ti-Al system”. *Physical Review B* 68.2 (2003), p. 024102.

[93] Peter Brommer et al. “Classical interaction potentials for diverse materials from *ab initio* data: a review of *potfit*”. *Modelling and Simulation in Materials Science and Engineering* 23.7 (2015), p. 074002.

[94] Mingjian Wen et al. “KLIFF: A framework to develop physics-based and machine learning interatomic potentials”. *Computer Physics Communications* 272 (2022), p. 108218.

[95] Alexander Stukowski et al. “Atomicrex—a general purpose tool for the construction of atomic interaction models”. *Modelling and Simulation in Materials Science and Engineering* 25.5 (2017), p. 055003.

[96] E. B. Tadmor et al. “The potential of atomistic simulations and the knowledgebase of interatomic models”. *JOM* 63.7 (2011), pp. 17–17.

[97] L. V. Woodcock. “Isothermal molecular dynamics calculations for liquid salts”. *Chemical Physics Letters* 10.3 (1971), pp. 257–261.

[98] H. J. C. Berendsen et al. “Molecular dynamics with coupling to an external bath”. *The Journal of Chemical Physics* 81.8 (1984), pp. 3684–3690.

[99] Hans C. Andersen. “Molecular dynamics simulations at constant pressure and/or temperature”. *The Journal of Chemical Physics* 72.4 (1980), pp. 2384–2393.

[100] Shuichi Nosé. “A unified formulation of the constant temperature molecular dynamics methods”. *The Journal of Chemical Physics* 81.1 (1984), pp. 511–519.

[101] William G. Hoover. “Canonical dynamics: Equilibrium phase-space distributions”. *Physical Review A* 31.3 (1985), pp. 1695–1697.

[102] *Periodic Boundary Conditions*. `https://isaacs.sourceforge.net/phys/pbc.html`.

[103] Aidan P. Thompson et al. “LAMMPS - a flexible simulation tool for particle-based materials modeling at the atomic, meso, and continuum scales”. *Computer Physics Communications* 271 (2022), p. 108171.

[104] Alexander Stukowski. “Visualization and analysis of atomistic simulation data with OVITO–the Open Visualization Tool”. *Modelling and Simulation in Materials Science and Engineering* 18.1 (2009), p. 015012.

[105] G. J. Ackland and A. P. Jones. “Applications of local crystal structure measures in experiment and simulation”. *Physical Review B* 73.5 (2006), p. 054104.

[106] Peter Mahler Larsen, Søren Schmidt, and Jakob Schiøtz. “Robust structural identification via polyhedral template matching”. *Modelling and Simulation in Materials Science and Engineering* 24.5 (2016), p. 055007.

[107] J. Dana. Honeycutt and Hans C. Andersen. “Molecular dynamics study of melting and freezing of small Lennard-Jones clusters”. *The Journal of Physical Chemistry* 91.19 (1987), pp. 4950–4963.

[108] Alexander Stukowski. “Structure identification methods for atomistic simulations of crystalline materials”. *Modelling and Simulation in Materials Science and Engineering* 20.4 (2012), p. 045021.

[109] *The Thomas Group - PTCL, Oxford*. `http://rkt.chem.ox.ac.uk/lectures/liqsolns/liquids.html`.

[110] Fen Luo et al. “SolidLiquid Interfacial Energy and Melting Properties of Nickel under Pressure from Molecular Dynamics”. *Journal of Chemical & Engineering Data* 55.11 (2010), pp. 5149–5155.

[111] K. Thurnay. *Thermal properties of transition metals*. Tech. rep. 0947-8620. 1998, p. 136.

[112] G.P. Purja Pun and Y. Mishin. “Development of an interatomic potential for the Ni-Al system”. *Philosophical Magazine* 89.34-36 (2009), pp. 3245–3267.

[113] Elena V. Levchenko et al. “Phonon-mediated heat dissipation in a monatomic lattice: case study on Ni”. *Philosophical Magazine* 95.32 (2015), pp. 3640–3673.

[114] V. Turlo, F. Baras, and O. Politano. “Comparative study of embedded-atom methods applied to the reactivity in the Ni–Al system”. *Modelling and Simulation in Materials Science and Engineering* 25.6 (2017), p. 064002.

[115] Y. Mishin. “Atomistic modeling of the and -phases of the Ni–Al system”. *Acta Materialia* 52.6 (2004), pp. 1451–1467.

[116] Juan D. Olarte-Plata and Fernando Bresme. “The impact of the thermostats on the non-equilibrium computer simulations of the interfacial thermal conductance”. *Molecular Simulation* 48.1 (2022), pp. 87–98.

[117] Noel Jakse et al. “Machine learning interatomic potentials for aluminium: application to solidification phenomena”. *Journal of Physics: Condensed Matter* 35.3 (2022), p. 035402.

[118] Sébastien Becker et al. “Unsupervised topological learning approach of crystal nucleation”. *Scientific Reports* 12.1 (2022), p. 3195.

[119] Yasushi Shibuta et al. “Heterogeneity in homogeneous nucleation from billion-atom molecular dynamics simulation of solidification of pure metal”. *Nature Communications* 8.1 (2017), p. 10.

[120] Yasushi Shibuta et al. “Submicrometer-scale molecular dynamics simulation of nucleation and solidification from undercooled melt: Linkage between empirical interpretation and atomistic nature”. *Acta Materialia* 105 (2016), pp. 328–337.

[121] Qiang Sheng et al. “On the onset of surface condensation: formation and transition mechanisms of condensation mode”. *Scientific Reports* 6.1 (2016), p. 30764.

[122] Tatsuto Kimura and Shigeo Maruyama. “MOLECULAR DYNAMICS SIMULATION OF HETEROGENEOUS NUCLEATION OF A LIQUID DROPLET ON A SOLID SURFACE”. *Microscale Thermophysical Engineering* 6.1 (2002), pp. 3–13.

[123] K. Yasuoka, G. T. Gao, and X. C. Zeng. “Molecular dynamics simulation of supersaturated vapor nucleation in slit pore”. *The Journal of Chemical Physics* 112.9 (2000), pp. 4279–4285.

[124] J. Q. Broughton and G. H. Gilmer. "Molecular dynamics investigation of the crystal–fluid interface. VI. Excess surface free energies of crystal–liquid systems". *The Journal of Chemical Physics* 84.10 (1986), pp. 5759–5768.

[125] M. Asta, J. J. Hoyt, and A. Karma. "Calculation of alloy solid-liquid interfacial free energies from atomic-scale simulations". *Physical Review B* 66.10 (2002), p. 100101.

[126] J. J. Hoyt, Mark Asta, and Alain Karma. "Method for Computing the Anisotropy of the Solid-Liquid Interfacial Free Energy". *Physical Review Letters* 86.24 (2001), pp. 5530–5533.

[127] W. A. Curtin. "Density-functional theory of crystal-melt interfaces". *Physical Review B* 39.10 (1989), pp. 6775–6791.

[128] D. W. Marr and A. P. Gast. "Planar density-functional approach to the solid-fluid interface of simple liquids". *Physical Review E* 47.2 (1993), pp. 1212–1221.

[129] Y. Xia et al. "Molecular dynamics studies on the correlation of undercoolability and thermophysical properties of liquid Ni–Al alloys". *Computational Materials Science* 112 (2016), pp. 383–394.

[130] Xian-Ming Bai and Mo Li. "Calculation of solid-liquid interfacial free energy: A classical nucleation theory based approach". *The Journal of Chemical Physics* 124.12 (2006), p. 124707.

[131] W. J. Boettinger et al. "Phase-Field Simulation of Solidification". *Annual Review of Materials Research* 32.1 (2002), pp. 163–194.

[132] F. Delogu and G. Cocco. "Molecular dynamics investigation on the role of sliding interfaces and friction in the formation of amorphous phases". *Physical Review B* 71.14 (2005), p. 144108.

[133] H. -J. Kim, S. Karthikeyan, and D. Rigney. "A simulation study of the mixing, atomic flow and velocity profiles of crystalline materials during sliding". *Wear*. 17th International Conference on Wear of Materials 267.5 (2009), pp. 1130–1136.

[134] B Li et al. "Molecular dynamics calculation of heat dissipation during sliding friction". *International Journal of Heat and Mass Transfer* 46.1 (2003), pp. 37–43.

[135] Brandon Witbeck and Douglas E. Spearot. "Grain size effects on Ni/Al nanolaminate combustion". *Journal of Materials Research* 34.13 (2019), pp. 2229–2238.

[136] Brandon Witbeck, Jake Sink, and Douglas E. Spearot. "Influence of vacancy defect concentration on the combustion of reactive Ni/Al nanolaminates". *Journal of Applied Physics* 124.4 (2018), p. 045105.

[137] Mathew J. Cherukara, Karthik Guda Vishnu, and Alejandro Strachan. “Role of nanostructure on reaction and transport in Ni/Al intermolecular reactive composites”. *Physical Review B* 86.7 (2012), p. 075470.

[138] Joshua C Crone et al. “Role of microstructure in initiation of Ni–Al reactive multilayers”. *Appl. Phys. Lett.* (), p. 4.

[139] Elena Levchenko et al. “Molecular dynamics simulation of alloying in a Ti-coated Al nanoparticle”. *Intermetallics* 22 (2013), pp. 193–202.

[140] Florence Baras et al. “SHS in Ni/Al Nanofoils: A Review of Experiments and Molecular Dynamics Simulations”. *Advanced Engineering Materials* 20.8 (2018), p. 1800091.

[141] Elena Levchenko et al. “Molecular dynamics simulation of the alloying reaction in Al-coated Ni nanoparticle”. *Computational Materials Science* 47 (2010), pp. 712–720.

[142] Sergey Kiselev and E. Zhirov. “Molecular-dynamics simulation of the synthesis of intermetallic Ti–Al”. *Intermetallics* 49 (2014), pp. 106–114.

[143] Amit Bandyopadhyay, Yanning Zhang, and Susmita Bose. “Recent developments in metal additive manufacturing”. *Current Opinion in Chemical Engineering*. Materials Engineering Separations Engineering 28 (2020), pp. 96–104.

[144] O. Politano and F. Baras. “Reaction front propagation in nanocrystalline Ni/Al composites: A molecular dynamics study”. *Journal of Applied Physics* 128.21 (2020), p. 215301.

[145] O. Politano, A. S. Rogachev, and F. Baras. “Molecular Dynamics Studies in Nanojoining: Self-Propagating Reaction in Ni/Al Nanocomposites”. *Journal of Materials Engineering and Performance* 30.5 (2021), pp. 3160–3166.

[146] Pierre Hirel. “Atomsk: A tool for manipulating and converting atomic data files”. *Computer Physics Communications* 197 (2015), pp. 212–219.

[147] A. Perron et al. “Oxidation of nanocrystalline aluminum by variable charge molecular dynamics”. *Journal of Physics and Chemistry of Solids*. EMRS 2009 Symposium D: Nano-scale Energetic Materials: Fabrication, Characterization and Molecular Modeling 71.2 (2010), pp. 119–124.

[148] Q. Jiang and H. M. Lu. “Size dependent interface energy and its applications”. *Surface Science Reports* 10.63 (2008), pp. 427–464.

[149] Marc J. Assael et al. “Reference correlations for the thermal conductivity of liquid copper, gallium, indium, iron, lead, nickel and tin”. *High Temperatures - High Pressures* 46.6 (2017), pp. 391–416.

[150] V. Turlo, O. Politano, and F. Baras. “Modeling self-sustaining waves of exothermic dissolution in nanometric Ni-Al multilayers”. *Acta Materialia* 120 (2016), pp. 189–204.

[151] David A. Porter, Kenneth E. Easterling, and Mohamed Y. Sherif. *Phase Transformations in Metals and Alloys*. 4th ed. 2021.

[152] Sepideh Kavousi et al. "Quantitative prediction of rapid solidification by integrated atomistic and phase-field modeling". *Acta Materialia* 211 (2021), p. 116885.

[153] Sepideh Kavousi et al. "A temperature-dependent atomistic-informed phase-field model to study dendritic growth". *Journal of Crystal Growth* 579 (2022), p. 126461.

[154] P. Zhang, S. X. Li, and Z. F. Zhang. "General relationship between strength and hardness". *Materials Science and Engineering: A* 529 (2011), pp. 62–73.

[155] Khader M. Hamdia and Timon Rabczuk. "Key Parameters for Fracture Toughness of Particle/Polymer Nanocomposites; Sensitivity Analysis via XFEM Modeling Approach". *Proceedings of the 7th International Conference on Fracture Fatigue and Wear*. Ed. by Magd Abdel Wahab. Lecture Notes in Mechanical Engineering. 2019, pp. 41–51.

[156] H. E. Kissinger. "Reaction Kinetics in Differential Thermal Analysis". *Analytical Chemistry* 29.11 (1957), pp. 1702–1706.

[157] Y. Mishin and Chr. Herzig. "Diffusion in the Ti–Al system". *Acta Materialia* 48.3 (2000), pp. 589–623.

[158] Acoff V. L. Luo J.G. "Interfacial reactions of titanium and aluminum during diffusion welding". *Welding Research Supplement to the welding Journal* (2000), pp. 239–243.

[159] N. Thiyaneshwaran, K. Sivaprasad, and B. Ravisankar. "Nucleation and growth of TiAl3 intermetallic phase in diffusion bonded Ti/Al Metal Intermetallic Laminate". *Scientific Reports* 8.1 (2018), p. 16797.

[160] Amir Hossein Assari and Beitallah Eghbali. "Microstructure and Kinetics of Intermetallic Phase Formation during Solid State Diffusion Bonding in Bimetal Ti/Al". *Physics of Metals and Metallography* 120.3 (2019), pp. 260–268.

[161] Mostafa Mirjalili et al. "On the kinetics of TiAl3 intermetallic layer formation in the titanium and aluminum diffusion couple". *Intermetallics* 32 (2013), pp. 297–302.

[162] T. Gòrecki. "Changes in the activation energy for self- and impurity-diffusion in metals on passing through the melting point". *Journal of Materials Science Letters* 9.2 (1990), pp. 167–169.

[163] Florence Baras and Olivier Politano. "Molecular dynamics simulations of nanometric metallic multilayers: Reactivity of the Ni-Al system". *Phys. Rev. B* 84 (2011).

[164] P. A. Kobryn and S. L. Semiatin. "The laser additive manufacture of Ti-6Al-4V". *JOM* 53.9 (2001), pp. 40–42.

[165] Adriaan B. Spierings et al. “Microstructure and mechanical properties of as-processed scandium-modified aluminium using selective laser melting”. *CIRP Annals* 65.1 (2016), pp. 213–216.

[166] X. P. Li et al. “Selective laser melting of nano-TiB2 decorated AlSi10Mg alloy with high fracture strength and ductility”. *Acta Materialia* 129 (2017), pp. 183–193.

[167] John H. Martin et al. “3D printing of high-strength aluminium alloys”. *Nature* 549.7672 (2017), pp. 365–369.

[168] Ting-Chiang Lin et al. “Aluminum with dispersed nanoparticles by laser additive manufacturing”. *Nature Communications* 10.1 (2019), p. 4124.

[169] Junsheng Wang et al. “Heterogeneous nucleation of solid Al from the melt by Al_3Ti: Molecular dynamics simulations”. *Physical Review B* 82.14 (2010), p. 144203.

[170] W. Wei et al. “Strain-stress relationship and dislocation evolution of W–Cu bilayers from a constructed n-body W–Cu potential”. *Journal of Physics: Condensed Matter* 31.30 (2019), p. 305002.

ECOLE DOCTORALE
CARNOT - PASTEUR

Résumé : La relation procédé-microstructure est centrale en sciences des matériaux car la microstructure va déterminer les propriétés des matériaux élaborés par les procédés. Dans notre travail, nous nous sommes intéressés à différents procédés de métallurgie en adoptant une description à l'échelle atomique. Cette approche permet de déceler les mécanismes élémentaires qui sont à l'origine des microstructures observées sans avoir à postuler des mécanismes macroscopiques et estimer les paramètres associés. A cet égard, les simulations par dynamique moléculaire fournissent un outil d'observation "in-situ" des systèmes métalliques pour autant qu'un potentiel d'interaction atomique soit disponible. L'originalité de notre démarche a été de modéliser les caractéristiques des procédés aux échelles nanométriques. Dans le contexte de la métallurgie des poudres, nous nous sommes intéressés à la fabrication additive de matériaux métalliques et à l'activation des poudres métalliques par broyage à haute énergie. Nous avons réalisé des simulations de dynamique moléculaire afin de comprendre les processus de solidification directionnelle à l'échelle nanométrique d'un métal polycristallin de Ni pur dans le contexte de la fabrication additive. Différentes microstructures ont été observées en fonction des conditions thermiques. La solidification et la nucléation ont également été comparées aux théories classiques de la solidification et de la nucléation afin d'en établir la validité aux échelles nanométriques. Nous avons modélisé le procédé de broyage par un traitement mécanique sous la forme d'une compaction et d'une déformation plastique pour rendre compte de l'action des billes de broyage sur un mélange binaire de poudres. Cette approche permet de comprendre le comportement des poudres activées mécaniquement (Ti+Al et Ni+Al) en caractérisant la mobilité des atomes, les transformations structurelles et la réactivité. Nous avons également étudié la réactivité d'un modèle multicouche nanométrique Ti-Al similaire aux matériaux obtenus après un broyage très énergétique. Nous avons mis en évidence plusieurs mécanismes élémentaires responsables de leur réactivité exacerbée comme la dissolution aux interfaces Ti(solide)/Al(liquide) et la formation d'intermétallique ($TiAl_3$).

Abstract: The process-microstructure relationship is central in materials science because the microstructure will determine the properties of the materials developed by the processes. In our work, we focused on different metallurgical processes by adopting a description at the atomic scale. This approach allows us to detect the elementary mechanisms that are at the origin of the observed microstructures without having to postulate macroscopic mechanisms or estimate the associated parameters. In this respect, molecular dynamics simulations provide a tool for "in-situ" observation of metallic systems as long as an atomic interaction potential is available. The originality of our approach consists in modeling the characteristics of the processes at nanometric scales. In the context of powder metallurgy, we focused on the additive manufacturing of metallic materials and the activation of metallic powders by high-energy milling. We performed molecular dynamics simulations to understand the directional solidification processes at the nanoscale of a pure Ni polycrystalline metal in the context of additive manufacturing. Various microstructures were observed as a function of thermal conditions. Solidification and nucleation were also compared to classical solidification and nucleation theories to establish their validity at the nanoscale. We modeled the milling process by mechanical treatment with compaction and plastic deformation to observe the action of grinding balls on a binary mixture of powders. This approach allows us to understand the behavior of mechanically activated powders (Ti+Al and Ni+Al) by characterizing atom mobility, structural transformations and reactivity. We also studied the reactivity of a Ti-Al nanometric multilayer model similar to the materials obtained after high-energy milling. We have highlighted several elementary mechanisms responsible for their increased reactivity, such as dissolution at the Ti(solid)/Al(liquid) interfaces and the formation of an intermetallic ($TiAl_3$).

UBFC
UNIVERSITÉ
BOURGOGNE FRANCHE-COMTÉ

Université Bourgogne Franche-Comté
32, avenue de l'Observatoire
25000 Besançon